Rydberg polaritons and Rydberg superatoms
-
Novel tools for quantum nonlinear optics

Von der Fakultät Mathematik und Physik der Universität Stuttgart
zur Erlangung der Würde eines Doktors der Naturwissenschaften (Dr. rer. nat.)
genehmigte Abhandlung

vorgelegt von

Christoph Tresp
aus Esslingen a. N.

Hauptberichter:	Dr. Sebastian Hofferberth
Mitberichter:	Prof. Dr. Martin Dressel
	Dr. Thomas Pohl
Prüfungsvorsitzender:	Prof. Dr. Hans Peter Büchler
Tag der mündlichen Prüfung:	22. Februar 2017

Universität Stuttgart
5. Physikalisches Institut

2017

Christoph Tresp: *Rydberg polaritons and Rydberg superatoms - Novel tools for quantum nonlinear optics*, PhD Thesis, Stuttgart, February 2017

Abstract

Mapping the strong interaction between Rydberg excitations in ultra-cold atomic ensembles onto single photons enables the realization of optical nonlinearities which can modify light on the level of individual photons. This novel approach forms the basis of a growing Rydberg quantum optics toolbox, which already contains photonic logic building-blocks such as single-photon sources, switches, transistors, and conditional π-phase shifts.
This thesis reports on two experiments investigating strong photon-photon interactions mediated by Rydberg interactions. First, applying a ladder-type EIT scheme to Rydberg atoms in D-states with high principal quantum number results in the Rydberg interaction mediated nonlinearity accompanied by a time-dependent decay of transmission of probe light through the medium. In a joint experimental and theoretical analysis, this effect is attributed to the dephasing of propagating polaritons into stationary Rydberg excitations caused by the state mixing interaction occurring with Rydberg D-state atoms. Second, via a two-photon Raman excitation scheme Rydberg atoms are efficiently excited in a small atomic cloud. As the size of the Rydberg blockade exceeds the dimension of the medium, only a single Rydberg excitation can be present at a time. By fast engineered dephasing this Rydberg excitation is decoupled from the light field. Measurement of the transmitted light and the amount of excited Rydberg atoms gives evidence for the realization of a deterministic single-photon absorber.

Declaration of authorship

I hereby declare that this thesis is my own work and that, to the best of my knowledge and belief, it contains no material previously published or written by another person, except where due acknowledgment has been made in the text.

Hiermit erkläre ich, dass diese Arbeit von mir eigenständig verfasst wurde und dass, außer an gekennzeichneten Stellen, kein Material verwendet wurde welches schon zuvor von anderen Personen verfasst wurde.

_____

Christoph Tresp

Publications

The work discussed in this thesis was published in:

- **C. Tresp**, P. Bienias, S. Weber, H. Gorniaczyk, I. Mirgorodskiy, H. P. Büchler, and S. Hofferberth
  Dipolar dephasing of Rydberg D-state polaritons; Phy. Rev. Lett, **115**, 083602 (2015)

- **C. Tresp**, C. Zimmer, I. Mirgorodskiy, H. Gorniaczyk, A. Paris-Mandoki, and S. Hofferberth
  Single-Photon Absorber Based on Strongly Interacting Rydberg Atoms; Phys. Rev. Lett. **117**, 223001 (2016)

- S. Weber, **C. Tresp**, H. Menke, A. Urvoy, O. Firstenberg, H. P. Büchler, and S. Hofferberth
  Tutorial: Calculation of Rydberg interaction potentials; arXiv:1612.08053; submitted to J. Phys. B (2016)

Furthermore, in the framework of this thesis following articles have been published:

- H. Gorniaczyk, **C. Tresp**, J. Schmidt, H. Fedder, and S. Hofferberth
  Single-Photon Transistor Mediated by Interstate Rydberg Interactions; Phy. Rev. Lett, **113**, 053601 (2014)

- H. Gorniaczyk, **C. Tresp**, P. Bienias, A. Paris-Mandoki, W. Li, I. Mirgorodskiy, H. P. Büchler, I. Lesanovsky, and S. Hofferberth
  Enhancement of Rydberg-mediated single-photon nonlinearities by electrically tuned Förster resonances; Nature Communications **7**, 12480 (2016)

- A. Paris-Mandoki, H. Gorniaczyk, **C. Tresp**, I. Mirgorodskiy, and S. Hofferberth
  Tailoring Rydberg interactions via Förster resonances: state combinations, hopping and angular dependence; J. Phys. B: At. Mol. Opt. Phys. **49** 164001 (2016)

Contents

1 Zusammenfassung in deutscher Sprache

Einführung in das Themengebiet dieser Arbeit

Die Herstellung von kleinsten atomaren Strukturen ist in unserer heutigen Zeit dank des technologischen Fortschritts eine gängige Methode, welche u.a. die Integration von Computern in den Alltag ermöglichte. Sowohl die Bandbreite als auch der Abtransport von Wärme in den verwendeten Halbleitermaterialen moderner Prozessoren wird den rapiden Fortschritt in Zukunft allerdings verlangsamen oder gar stoppen. Aufgrund seiner Eigenschaft fast verlustfrei und mit hoher Geschwindigkeit große Strecken zurücklegen zu können, ist der Einsatz von Licht als Ersatz elektronischer Bauteile in zukünftigen-Computergenerationen erstrebenswert [1].

Neben den möglichen Anwendungen in klassischen Computern sind Photonen, nicht zuletzt seit der ersten Demonstration verschränkter Photonenpaaren [2, 3] ein hervorragender Kandidat für den Einsatz in Quantencomputern [4] und -simulatoren [5]. Die Grundbausteine solcher Anwendungen, wie z.B. optische Gatter oder Transistoren, basieren dabei auf starken Wechselwirkungen zwischen einzelnen Photonen. Da Photonen im Vakuum allerdings nicht miteinander wechselwirken, müssen optisch nichtlineare Materialen gefunden werden um die benötigten Wechselwirkungen zwischen einzelnen Photonen zu vermitteln. In herkömmlichen optischen Materialen sind Wechselwirkungen zwischen einzelnen Photonen vernachlässigbar klein. Demzufolge treten nichtlineare Effekte, wie etwa die Frequenzverdopplung [6] oder auch die Summenfrequenzbildung [7] erst bei sehr hohen Lichtintensitäten auf.
Das einfachste System, welches man sich als Forscher zur Realisierung von Nichtlinearitäten zwischen einzelnen Photonen vorstellen kann, besteht aus einem einzelnen Atom welches an ein Lichtfeld gekoppelt wird [8]. Zum Erreichen starker Wechselwirkungen zwischen den einzelnen Photonen des Lichtfelds ist die Sättigung des atomaren Übergangs mit einem einzelnen Photon erforderlich. Allerdings verlangt der winzige Streuquerschnitt der Atom-Licht-Wechselwirkung, dass der einfallende Lichtpuls an die dipolförmige Abstrahlcharakteristik des Atoms angepasst wird. Trotz des enormen Fortschritts in der Ingenieurskunst zur Fertigung von Präzisionsoptiken, konnten bisher nur schwache Kopplungseffizienzen erreicht werden [9].
Einen alternativen Ansatz bietet die Nutzung atomarer Ensembles in welchen Lichtpulse unter der Verwendung von langsamem Licht [10], welches mit Hilfe vom elektromagnetisch induzierter Transparenz (EIT) erzeugt wird [11, 12]. Obwohl die Stärke der so erzielbaren Wechselwirkungen im Prinzip limitiert ist [13], konnte mit dieser Methode

erst vor kurzem ein Phasenschub gemessen werden, welcher einen Wert von π übertrifft. Dazu wurde nur eine geringe Menge Licht, bestehend aus acht Photonen benötigt [14]. Eine extreme Verstärkung optischer Nichtlinearitäten wurde mittels einzelner, in der Grundmode optischer Resonatoren hoher Güte gefangener Atome realisiert [15]. Dabei wird die Atom-Licht-Wechselwirkung durch die vielen Umläufe, welche ein einzelnen Photon im Resonator untergehen kann bevor es emittiert wird, extrem verstärkt. Neben vielen weiteren beeindruckenden Resultaten im Bereich der Quantenelektrodynamik mit Resonatoren sind insbesondere die Verschränkung von Photonenpaaren [16], die Realisierung eines Einzel-Photonen-Transistors welcher durch ein einzelnes Photon geschalten wird [17], und der von einem einzelnen Photon hervorgerufene optische Phasenschub [18] erwähnenswert. Allerdings sind die hohen technischen Anforderungen nur schwer mit der erforderliche Skalierbarkeit zu vereinbaren. Darüberhinaus limitiert die benötigte hohe Güte der Resonatoren die maximal erzielbare Bandbreite.

In einem komplementären Ansatz werden die starken Dipol-Dipol-Wechselwirkungen zwischen Paaren von Rydbergatomen in kalten atomaren Gasen ausgenutzt, um diese auf Photonen zu übertragen. Generell wurden Rydbergatome, also Atome die wenigstens ein Elektron besitzen welches in einen Zustand hoher Hauptquantenzahl angeregt wurde (typischerweise $n > 10$), im Bereich der Atomphysik im Laufe der letzten Jahre ein beliebter Forschungsgegenstand. Das Feld entwickelt sich rapide in verschiedenste Richtungen, welche sich von kalten, atomaren Kollisionen zwischen einzelnen Rydbgerg-Elektronen und ultra-kalter Materie [19, 20], über Einzel-Quanten-Bit Gatter [21, 22], bis hin zur Realisierung von quantalen Vielteilchensystem erstrecken [23, 24]. In den für dieses Schriftstück relevanten Arbeiten wird die Rydberg basierte Anregungsblockade [25] als Grundlage verwendet. Bei resonanter Anregung mit Laserlicht darf im sogenannten Bereich der Rydbergblockade nur ein einzelnes Atom in den Rydbergzustand angeregt werden, die Energieniveaus von benachbarten Atomen werden aufgrund der Rydberg-Rydberg Wechselwirkung aus der Anregungsbandbreite des Lasers geschoben. Dies erlaubt die Beobachtung kollektiver Vielteilchendynamik und die Verschränkung großer Atomzahlen. Obwohl sich die Rydberg-Wechselwirkung zum ersten Mal als Verbreiterungsmechanismus in der Spektroskopie von Zäsiumdampf bemerkbar machte [26], revolutionierten sowohl die Verfügbarkeit der Laserkühlung neutraler Atome [27, 28] als auch präzise Spektroskopiemethoden das Feld der Rybergphysik. Bei Temperaturen im Bereich weniger Mikrokelvin dominieren die Wechselwirkungsenergien auf der Größenordnung von einigen Gigahertz, diese Errungenschaft ermöglichte beispielsweise die Beobachtung kohärenter Zeitentwicklung verschränkter Atompaare [29, 30], die Durchstimmbarkeit der Wechselwirkungsstärke vom Bereich der van-der-Waals Wechselwirkung [31] hin zu resonanter Dipol-Dipol Wechselwirkung [32, 33], oder Bildung geordneter Strukturen [34]. Insbesondere die mittlerweile verfügbaren Techniken zur kohärenten Kontrolle machen Rydbergatome zu einem vielversprechenden Kandidaten für die Realisierung von Modellsystemen mit gut kontrollierbarer Größe und Form zum Einsatz als universeller Quantensimulator [35].

Die Nutzung der enormen Wechselwirkung zwischen Rydbergatomen zur Erzeugung starker Nichtlinearitäten zwischen einzelnen Photonen, wurde erstmals im Jahr 2005

von Friedler *et al.* vorgeschlagen [36]. Dem Vorschlag liegt die Kopplung eines Rydbergzustands in einem EIT-Schema zugrunde. Dadurch werden Photonen in einem optisch dichten Medium in sich langsam bewegende Polaritonen umgewandelt, also in Quasiteilchen welche sowohl photonische als auch atomare Eigenschaften besitzen [12]. Wegen der Rydberg-Wechselwirkung können sich zwei Polaritonen nicht gemeinsam durch das Medium bewegen wenn ihr Abstand kleiner als die Größe der Rydbergblockade ist. Dies hat stark nichtlineare Transmissionseigenschaften und die Änderung der Photonenstatistik des transmittierten Lichtfeldes zur Folge. Die erste experimentelle Umsetzung dieses Vorschlags gelang im Jahr 2010 der Gruppe von Charles Adams [37]. Experimentelle Verbesserungen ermöglichten im Folgenden die Beobachtung von nichtklassischem Licht, welches durch die Wechselwirkung einzelner Photonen verursacht wird [38, 39, 40]. Weitere Meilensteine waren die Realisierung eines gebundenen Zustands bestehend aus zwei Photonen [41] und die Messung eines Phasenschubs von π, ausgelöst von einem einzelnen Photon [42]. Basierend auf diesen beeindruckenden Ergebnissen wurde ein tiefgreifendes theoretisches Verständnis entwickelt [43]. Darauf aufbauende Arbeiten sagen beispielsweise neuartige, auf der Wechselwirkung zwischen drei Photonen beruhende Eigenschaften [44, 45] oder die kristallartige Anordnung von Photonen [46] voraus. Ein Übergang von eindimensionalen zu zwei- oder dreidimensionalen Geometrien wird in zukünftigen Experimenten den Übergang zu aus Photonen bestehenden Vielteilchensystemen ermöglichen.

Ergebnisse dieser Arbeit

Im Rahmen dieser Arbeit wurde, beginnend im Juli 2012, ein Experiment zur Untersuchung starker optischer Nichtlinearitäten aufgebaut. Der Aufbau der Experimentapparatur beruht auf den gängigen Kühlmethoden für neutrale Atome und ermöglicht die Erzeugung atomarer Ensembles mit Temperaturen im Bereich weniger Mikrokelvin. Die Verwendung optischer Dipolfallen stellt eine hohe Flexibilität bei der Kontrolle von Form und Größe des atomaren Mediums zur Verfügung. Durch die Kopplung von Rydberg-Wechselwirkungen an das Lichtfelds mittels EIT, ermöglichte diese Apparatur die experimentelle Umsetzung eines Einzelphotonen-Transistors, welcher mittels eines einzigen Schaltphotons die Transmission von über hundert Zielphotonen an- oder ausschalten kann [47, 48].

Auf der daraus gewonnenen Erkenntnis, starke Wechselwirkungen zwischen einzelnen Photonen erzielen zu können aufbauend, werden in dieser Arbeit zwei weiterführende Experimente beschrieben. Die experimentellen Ergebnisse und deren Interpretation sind dabei sowohl in theoretische Ausarbeitungen der Rydberg-Rydberg Wechselwirkung und der Atom-Licht Wechselwirkung, als auch eine kurze Beschreibung des experimentellen Aufbaus eingebettet.

Im Einzelnen, wurde während dieser Arbeit zunächst die Transmission von Photonen durch die Atomwolke untersucht, wobei das Lichtfeld mittels EIT an einen Rydberg D-Zustand (L=2) gekoppelt wurde. Dieses Experiment ermöglichte es, neue Erkenntnisse

über die Propagationseigenschaften von Polaritonen unter Beachtung anisotroper Wechselwirkungen zu gewinnen [49]. Zeitabhängige Messungen der Transmission durch die Atomwolke zeigten sowohl die bereits bekannte optische Nichtlinearität [41, 37], verursacht durch die starken Rydberg-Rydberg Wechselwirkungen, als auch eine zeitabhängige Abnahme der Transmission. In verschiedenen Messreihen wurde die Skalierung dieses neuen Effekts mit der Photonenrate, der Rabifrequenz des Kontrolllasers und der Hauptquantenzahl untersucht. Besonders der Befund, dass die Abnahme der Transmission mit der Wahrscheinlichkeit gleichzeitig zwei Polaritonen im Medium zu finden skaliert, motivierte dabei folgende Erklärung: Die durch die anisotrope Rydberg-Wechselwirkung verursachte Mischung entarteter Zeeman-Zustände verursacht die Besetzung von vom Lichtfeld abgekoppelten Spin-Zuständen, welche als stationäre Rydberganregungen in der Atomwolke zurückbleiben und diese blockieren. Zur weiteren theoretischen Beschreibung wurden deshalb winkel- und abstandsabhängige Wechselwirkungspotentiale ausgerechnet. Diese Potential ermöglichten die Berechnung von Dephasierungsraten aus dem vom Lichtfeld gekoppelten Zustand in ungekoppelte Zustände. Vergleiche mit dem anisotropen Rydbergblockaderadius zeigten, dass diese Dephasierungsraten für Rydberg D-Zustände im Vergleich zu S-Zuständen außerhalb der Blockade nicht vernachlässigt werden dürfen. Der zusätzliche Einbau der berechneten Dephasierungsraten in numerische Simulationen für die Propagation von Polaritonen durch ein dreidimensionales Medium ergab qualitative Übereinstimmung mit dem Experiment.

Durch die extreme Verkleinerung der Atomwolke mit Hilfe eines zusätzlichen Fallenlasers war es möglich, in einen Parameterbereich einzutreten in welchem aufgrund der Rydbergwechselwirkung nur ein einzelnes Atom in den Rydbergzustand angeregt werden kann [50]. In diesem Fall muss die Ununterscheidbarkeit der Atome berücksichtigt werden, da sich prinzipiell jedes Atom im Rydbergzustand befinden kann. Dieser Tatsache kann Rechnung getragen werden, indem neue, kollektive Zustände betrachtet werden. Die entsprechende Basistransformation liefert neben dem Grundzustand $|\mathcal{G}\rangle$ einen vom Lichtfeld gegkoppelten Zustand $|\mathcal{W}\rangle$ und $N-1$ ungekoppelte Zustände $|\mathcal{D}_j\rangle$. Die gesamte kohärente Entwicklung des Vielteilchensystems kann also durch zwei Zustände beschrieben werden, weswegen ein solches System häufig als „Superatom“ beschrieben wird. Im Experiment wurde die durch die Absorption des ersten Photons entstandene Rydberganregung vom Lichtfeld abgekoppelt um Rabioszillationen des Superatoms zu verhindern. Um dies zu erreichen wurde der lichtgekoppelte Zustand $|\mathcal{W}\rangle$ an die ungekoppelten Zustände $|\mathcal{D}_j\rangle$ gekoppelt [51]. Als Mechanismus dienten dabei die Dephasierung des Superatoms aufgrund der thermischen Bewegung der Atome, die inhomogene Linienverbreiterung durch die optische Falle und die Linienverbreiterung durch die Bildung von Rydbergmolekülen. Messungen der Zahl der durch die Atomwolke transmittierten Photonen und der Vergleich mit der Anzahl der in die Wolke gesendeten Photonen zeigten, dass auf diese Weise ein effizienter Absorber für einzelne Photonen realisiert werden kann. Diese Behauptung wurde durch gemessene Statistik der angeregten Rydbergatome eindrucksvoll bestätigt.

2 Introduction

The manufacturing of tiniest structures of matter atom by atom is nowadays an established technology which made the integration of computers in everydays life possible. However, both the bandwidth and the heat transport of the semiconductor components in modern processors will soon impose a limit on future progress. Based on their ability to almost frictionless travel with high speed over long distances, photons are an ideal candidate to replace electronic parts in future computers [1].

Besides the applications in classical computation, photons are not only since the first demonstration of entangled photon pairs [2, 3] an ideal candidate for quantum computation [4] and simulation [5]. The building blocks of such implementations, like all-optical gates and transistors, necessitate strong interactions between individual photons. As photons are per se non-interacting this demand triggered the search for strongly nonlinear media mediating effective interactions between individual photons. In conventional optical materials, photon interactions are negligible and nonlinear effects, such as frequency doubling [6] or sum-frequency generation [7], do only occur at very high intensities.
The most basic system to think of in this research direction consists of a single atom being coupled to a weak light field [8]. Achieving strong effective interactions between the individual photons of the probe field demands saturation of the atomic absorption with a single photon. The tiny atom-photon scattering cross section demands to match the shape of the light field to the dipolar emission pattern of the single atom. Even having in mind the vast progress in engineering of precision optics, up to now only weak coupling efficiencies have been reached [9].
Alternatively, optical nonlinearities have been investigated in ensembles of atoms where light pulses are compressed inside the medium by means of slow light [10] offered by electromagnetically induced transparency (EIT) [11, 12]. Although the interaction strength is in principle limited [13], recently a cross-phase modulated phase shift exceeding π induced by a weak field containing eight photons has been realized [14].
Great enhancement of optical nonlinearities has been realized with single atoms placed in the node of high-finesse cavities [15]. In such systems, the light-matter interaction is greatly enhanced by the many round-trips a single photon can make inside the cavity before it gets lost. Among other achievements demonstrating nonlinearities on the single photon level, the outstanding results of cavity QED utilizing single atoms are the entanglement of a photon-pair [16], demonstration of a single photon transistor gated by one photon [17], and a deterministic phase shift induced by a single photon [18]. The high technical demands on the design and stability adversely affect the required scalability of

cavity systems. On top, the high finesse demanded to enter the strong coupling regime sets an upper limit to the achievable bandwidth.
A complementary approach utilizes the strong dipole-dipole interactions between pairs of Rydberg atoms in cold atomic gases by mapping these onto photons. In general, Rydberg atoms, with at least on of their electrons excited to a state with large principal quantum number (typically $n > 10$), have become a central research topic in the framework of atomic physics. Over the last decade this field has evolved into diverse directions, ranging from studies of cold atomic collisions of single electrons with ultra-cold matter [19, 20], over single-qubit quantum gates [21, 22] to the realization of quantum many-body systems [23, 24]. In this thesis, the Rydberg excitation blockade [25] serves as underlying mechanism, exploited in the framework of various theoretical and experimental work. When resonantly driven by a laser field, inside a so-called Rydberg blockade region only a single excitation to a Rydberg state can occur, energy levels of atoms surrounding a present excitation are shifted out of resonance by the strong Rydberg-Rydberg interactions. This effect gives rise to coherent many-body dynamics in mesoscopic ensembles and entanglement of large atom numbers. Although interaction induced broadening of excitation lines was for the first time observed in a hot cesium vapour [26], the availability of cooling techniques for neutral atoms [27, 28] and precision spectroscopy revolutionized the Rydberg field. At temperatures in the micro-Kelvin regime the interaction energies on the order of GHz become the dominating terms, allowing the observation of e.g. coherent evolution entangled atom pairs [29, 30] and ensembles [52, 53], tunability of the interaction strength from van-der-Waals type $1/R^6$ interaction [31] to resonant dipole-dipole $1/R^3$ interaction [32, 33], or the formation of ordered structures [34]. Especially the meanwhile available coherent control techniques make ensembles of Rydberg atoms a promising candidates to realize model systems with well controllable geometries and parameters for quantum simulation purposes [35].

Employing the strong interactions among Rydberg atoms to mediate strong nonlinearities between individual photons dates back to the first proposal of Friedler *et al.* in 2005 [36]. The proposal is based on addressing a Rydberg state in an EIT scheme, transforming photons inside an optically dense medium into slowly propagating dark state polaritons [12], quasi-particles with both photonic and atomic character. As a consequence of the Rydberg interaction, two polaritons cannot travel through the medium at distances smaller than the Rydberg blockade, resulting in nonlinear transmission and change of the photon statistics at the output of the medium. The group of Charles Adams reported the experimental realization of such optical nonlinearities for the first time in 2010 [37]. Subsequent experimental advances facilitated the generation of non-classical light due to interactions on the level of single photons, changing the quantum statistics of the transmitted light [38, 39, 40]. A further milestone in the field was the observation of a photonic bound state by Firstenberg *et al.* [41] and a phase shift of π induced by a single photon [42]. Triggered by the groundbreaking experimental results, a thorough theoretical understanding was developed [43]. Further work predicts for example three-photon interactions showing novel features [44, 45] or crystalline arrangement of

photons [46]. Transition from one-dimensional to two- or three-dimensional geometries in future experiments will enable transitions from few- to many-body systems of interacting photons.

This thesis

In the framework of this thesis, starting in July 2012 an apparatus has been build with the goal of realizing such strong optical nonlinearities mediated by Rydberg interactions. Simultaneously with the group of Gerhard Rempe at the Max Planck Institute of Quantum Optics in Munich, this apparatus enabled the realization of an all-optical transistor switching up to 100 signal photons with a single incident gate photon [47, 54, 48].
Based on this outstanding demonstration of huge optical nonlinearities on the level of single photons, this thesis treats two nonlinear experiments coming from slightly different directions. The first experimental result utilizes the approach introduced before by applying a resonant EIT scheme to convert photons into polaritons [12] slowly propagating through a elongated atomic medium. During the propagation time of hundreds of nanoseconds two polaritons can interact inside the medium resulting in strong effective photon-photon interactions. In contrast to earlier work the experiments are performed with Rydberg D-states showing a rich angular dependence in their interaction which imposes additional nonlinear effects. These experiments are highly interesting in view of many other proposals and experiments investigating the angular dependence of Rydberg interactions [55, 56, 57, 58].
The second experimental achievement of this thesis is realized by a rather complementary approach. Instead of an EIT scheme, the Rydberg state is addressed in a two-photon Raman scheme, i.e. the photons are travelling with the speed of light. In combination with an extremely short medium allowing only the excitation of a single Rydberg atom at a time this opens another branch of Rydberg mediated nonlinear quantum optics. The single excitation shared among a large number of ground state atoms results in a coherent superposition state, a so-called superatom [59, 51], resulting in an enhancement of the driving Rabi frequency with the square root of the atom number [30, 29, 52, 53]. In contrast to a single atom coupled to a light field, such a superatom can still carry only a single excitation, but the light matter interaction is enhanced due to the large number of ground state atoms. By decoupling the light field from the superatom after the excitation of a first photon, the demonstration of a deterministic single-photon absorber was realized in the scope of this thesis.

This thesis is structured as follows:

In chapter 3, an overview of the exaggerated properties of Rydberg atoms stemming from the low binding energy of the Rydberg electron is given. The chapter summarizes the tools required to describe the interaction of a pair of Rydberg atoms in the presence of electric fields and arbitrary arrangement of the Rydberg atoms in space. The last section motivates the need for the full calculation of Rydberg-Rydberg interaction by comparison of calculated potentials with current experiments. Chapter 4 introduces the transmission properties of an atomic three-level system coupled by two driving laser fields. Based on the solution of the Master equation the transmission properties of a weak probe light through an atomic ensemble is derived for different parameters like intensity

or detuning of the driving lasers or intrinsic atomic properties causing decoherence. At the end of the second chapter understanding of Rydberg interactions is combined with the derived transmission properties to draw conclusions which requirements have to be experimentally fulfilled to observe nonlinear effects on the level of single photons.
Chapter 5 introduces the apparatus which has been built during the thesis. The primary focus in this chapter is put on the implementation of an atomic medium with tunable size and high density. Additionally, the measurement techniques and concepts used in the experiment are presented.
Subsequently, chapter 6 reports about the nonlinear effects investigated by applying the Rydberg-EIT scheme to Rydberg atoms in a D-state ($L = 2$). In contrast to previous experiments working with S-states, the transmission of weak light pulses through the medium on EIT resonance shows a time dependence which scales quadratically with the input photon number. Based on experimentally determined scaling laws with light intensities and principal quantum number, a model is developed explaining the observed effect by dephasing of polaritons into stationary Rydberg excitations decoupled from the light field. This dephasing is caused by the angular dependence of the Rydberg interaction of D-states, resulting in a coupling of different magnetic spin states. Full numerical simulation of the two-photon wave function reveals qualitative agreement with the experiment.
Chapter 7 reports the realization of a deterministic single-photon absorber based on strong coupling of a light field to a Rydberg superatom. Fast engineered dephasing decouples the Rydberg atom from the light field ones a first photon is absorbed, rendering the medium transparent for subsequent photons. A detailed discussion explicates this process, measurements of both transmitted photons and excited Rydberg atoms for input photon numbers up to $\overline{N}_{in} = 35$ demonstrate strong evidence for the realization of such an saturable absorber.
Finally, the work within this thesis is summarized and a short outlook presents future perspectives of the research direction.

Part I

THEORETICAL FOUNDATIONS

I... a universe of atoms, an atom in the universe.

Richard Feynman

3 Rydberg atoms and their interaction

The expression Rydberg atom refers to atoms which have at least one of their electrons excited to large principal quantum number n, with typically $n > 10$. In such states, the Rydberg electron has only very small overlap with the core (nucleus and inner electron shells) of the atom, resulting in numerous of extreme properties. Due to the low binding energy, Rydberg atoms are extremely sensitive to external perturbations by both electric and magnetic fields. But even the presence of other Rydberg atoms nearby can influence the energy levels.

The first section of this chapter summarizes the most important properties of Rydberg atoms which are relevant for the experiments within this thesis. It follows a detailed discussion of the calculation of angular dependent Rydberg-Rydberg interaction potentials, parts of this discussion were published within the scope of this thesis in [60]. The results of this section play an important role for the experiments presented later on in chapters 6 and 7. The third section compares example calculations of the full Rydberg-Rydberg interaction with current experiments. A open-source software programmed by Sebastian Weber which is based on the formalisms summarized here and in [60], allows fast computation of numerous Rydberg potentials[1]

3.1 BASIC PROPERTIES OF RYDBERG ATOMS

Although the internal structure of Alkali atoms is due to the larger nucleus number much more complicated, Alkali Rydberg atoms with one electron far out from the core share some basic properties with the well understood Hydrogen atom. Reason is the shielding of the nucleus by the inner electrons forming closed shells. As a consequence, the outer Rydberg electron "feels" an almost pure Coulomb potential. It was at first Johannes Rydberg who found that the spectra observed with Alkali atoms obey a similar law like the ones of Hydrogen.

In many textbooks the potential energy E_{nLJ} of an electron excited to a Rydberg state is nowadays described by

$$E_{nLJ} = -\frac{hcR^*}{(n^*)^2} = -\frac{hcR^*}{(n-\delta_{nLJ})^2}. \tag{3.1}$$

[1] https://github.com/pairinteraction/pairinteraction

Property	**n scaling**	$5S_{1/2}$	$100S_{1/2}$
binding energy	$(n^*)^{-2}$	4.18 eV	1.435 meV
orbit radius	$(n^*)^2$	5.632 a0	13810 a_0
level spacing	$(n^*)^{-3}$	$5S \leftrightarrow 6S$: 2.5 eV	$99S \leftrightarrow 100S$: 29.05 µeV
trans. dipole moment	$(n^*)^{-3/2}$	$5S \leftrightarrow 5P$: 4.227 ea_0	$5P \leftrightarrow 100S$: 0.0047 ea_0
polarizability	$(n^*)^7$	-79.4 mHz/(V/cm)^2	-6.197 GHz/(V/cm)^2

Table 3.1: **Properties of Rydberg atoms** This table gives an overview over the extreme properties of Rydberg atoms and how their scaling with the effective principal quantum number n^*. Exemplary values calculated for an Rydberg atom excited to $100S_{1/2}$ indicate the extreme properties Rydberg atoms can reach. The corresponding values of ^{87}Rb ground state atoms for comparison are taken from [64].

Here, R^* is the modified Rydberg constant and n^* the effective quantum number. Latter one can be expressed as $n^* = n - \delta_{nLJ}$ including the quantum defect δ_{nLJ} [61]. These parameters incorporate species dependent modifications to the bare Coulomb potential occurring in multi-electron atoms with filled inner shells. A detailed analysis of these parameters is given in B.1.

The decrease of the binding energy with $(n^*)^2$ revealed by eq. (3.1) gives reason to the extreme properties of Rydberg atoms. First, as a direct consequence, the extend of the electron wave function has only small overlap with the nucleus. Excited to high principal quantum numbers, Rydberg atoms can thus form macroscopic objects [62]. Second, the weak binding energy results in a high sensibility to perturbations, for example to weakest electric fields. This makes Rydberg atoms a promising candidate for electric field sensing [63].

Table 3.1 lists some of the extreme properties of Rydberg atoms and compares them to ground state atoms. As one example, the properties are calculated for $100S_{1/2}$ in ^{87}Rb. From the given scaling laws with n^*, corresponding values for other principal quantum numbers can be estimated. The values for $5S_{1/2}$ are taken from [64].

3.2 INTERACTION BETWEEN TWO RYDBERG ATOMS

The typical picture usually considered when calculating Rydberg-Rydberg interaction is sketched in Fig. 3.1 (a). Two neutral atoms (these can be different chemical species) which are separated by the interatomic distance R are each excited to a Rydberg state. The typical question popping up is: *How does the interaction change the energy level of this pair of Rydberg atoms, and what is the probability to couple to such a doubly excited state with a light field.*

As long as the separation R of the two nuclei is large compared extension of the atoms the interaction is dominated by the interactions of the Rydberg electrons. In the Born-

Oppenheimer approximation [65] the two-atom Hamiltonian describing this two-body problem can then be written in the form

$$\hat{H}(\boldsymbol{R}) = \hat{H}_0 + \hat{H}_{\text{int}}(\boldsymbol{R}). \tag{3.2}$$

In this sum $\hat{H}_0$ contains the energies of the unperturbed Rydberg states, while $\hat{H}_{\text{int}}$ represents the interaction between the two valence electrons in the Rydberg state, the two ionic cores, and the cross terms resulting from interaction of the Rydberg electron of one atom and the ionic core of the other atom. This standard treatment of two interacting Rydberg atoms in detail in [66, 31, 67, 68].

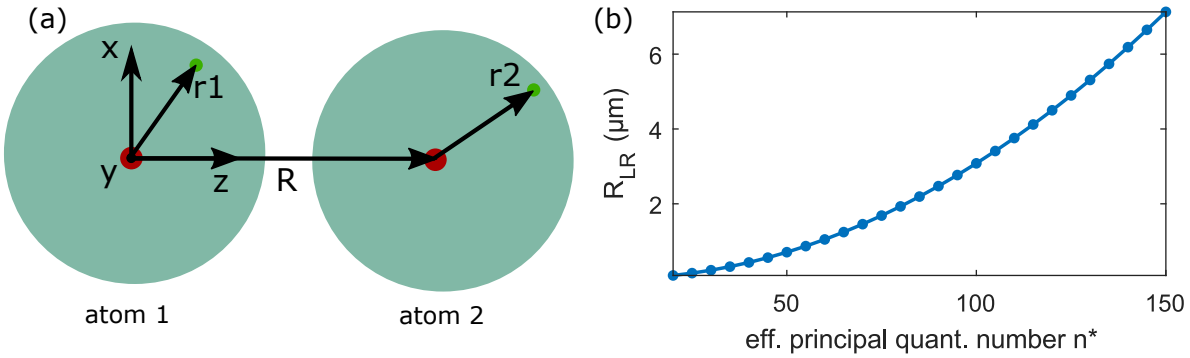

Figure 3.1: **Interaction of two Rydberg atoms** (**a**) System considered for the calculation of Rydberg-Rydberg interactions. To simplify the calculations, two Rydberg atoms with their interatomic axis R aligned along the z-axis of a coordinate system are regarded. The positions of the respective electrons in atom 1 and atom 2 are denoted by the labels r_1 and r_2. The separation R of the Rydberg atoms has to extend the Le Roy radius R_{LR} such that the wave functions of the atoms do not overlap. (**b**) Calculated Le Roy radius for different nS-nS Rydberg pairs in ^{87}Rb according to eq. (3.4).

As the hyperfine splitting of Rydberg states is typically smaller than the interaction energy [69, 70, 71], it is convenient to treat the interaction problem in the fine structure basis. Assuming, that the two Rydberg atoms are distinguishable it is evident to work with product states $|n_1 L_1 J_1 m_{J1}; n_2 L_2 J_2 m_{J2}\rangle = |n_1 L_1 J_1 m_{J1}\rangle \otimes |n_2 L_2 J_2 m_{J2}\rangle$. In this product basis the operator $\hat{H}_0$ reads

$$\begin{aligned}\hat{H}_0 = \quad & \textstyle\sum_{n_1,L_1,J_1,m_{J1}} E_{n_1 L_1 J_1} \, |n_1 L_1 J_1 m_{J1}\rangle \langle n_1 L_1 J_1 m_{J1}| \otimes \mathbb{1} \\ & + \mathbb{1} \otimes \textstyle\sum_{n_2,L_2,J_2,m_{J2}} E_{n_2 L_2 J_2} \, |n_2 L_2 J_2 m_{J2}\rangle \langle n_2 L_2 J_2 m_{J2}| \ ,\end{aligned} \tag{3.3}$$

where $E_{n,L,J}$ is the binding energy of the Rydberg electron in the state $|n, L, J, m_{J1}\rangle$ defined in eq. (3.1).

An important assumption for the calculation of the interaction energy $\hat{H}_{\text{int}}$ is that the interatomic distance R is larger than the Le Roy radius [72]

$$R_{\text{LR}} = 2\left(\sqrt{\langle n_1 L_1 J_1 | \hat{r}_1^2 | n_1 L_1 J_1\rangle} + \sqrt{\langle n_2 L_2 J_2 | \hat{r}_2^2 | n_2 L_2 J_2\rangle}\right). \tag{3.4}$$

The terms under the square roots are individual matrix elements for each atom estimating the size of each valence electron wave function. This requirement ensures that the electron wave functions do not overlap. Consequently, not the full molecular problem has to be treated, i.e. both charge overlap interaction and exchange interaction can be neglected. This extremely simplifies the calculation as the electrons can be assigned to their respective atoms. In Fig. 3.1 (b) the Le Roy radius is plotted for different $nS - nS$ Rydberg pairs of ^{87}Rb atoms to give an example of the length scale on which the calculations are valid.

The interaction problem is now treated in total analogy to the case of classical electrostatics. Both atoms can be considered as individual charge distributions which can be expressed in a multipole expansion series [73]. The electrostatic interaction energy of the atoms then takes the form

$$H_{\mathrm{int}}(\boldsymbol{R}) = \frac{e^2}{4\pi\epsilon_0}\left(\frac{1}{|\boldsymbol{R}+\boldsymbol{r}_2-\boldsymbol{r}_1|}+\frac{1}{|\boldsymbol{R}|}-\frac{1}{|\boldsymbol{R}-\boldsymbol{r}_1|}-\frac{1}{|\boldsymbol{R}+\boldsymbol{r}_2|}\right). \tag{3.5}$$

While $\boldsymbol{R}$ is the distance vector pointing from one nucleus to the other, $\boldsymbol{r}_1$ and $\boldsymbol{r}_2$ are the positions of the two valence electrons given as relative coordinates in the body frame of the respective atom, like illustrated in Fig. 3.1 (a). Evaluation of the multipole expansion in this coordinate frame leads to

$$H_{\mathrm{int}}(\boldsymbol{R}) = \sum_{\kappa_1,\kappa_2=1}^{\infty} \frac{V_{\kappa_1\kappa_2}}{4\pi\epsilon_0|\boldsymbol{R}|^{\kappa_1+\kappa_2+1}}, \tag{3.6}$$

derived in several publications [74, 75, 76]. The exact expression of $V_{\kappa_1\kappa_2}$ depends on the choice of the coordinate systems used to label the positions of the electrons. If it is chosen such that the z-axis coincides with interatomic axis $\boldsymbol{R}$, $V_{\kappa_1\kappa_2}$ takes the comparatively simple form

$$V_{\kappa_1\kappa_2} = (-1)^{\kappa_2} \sum_{q=-\kappa_<}^{\kappa_<} \sqrt{\binom{\kappa_1+\kappa_2}{\kappa_1+q}\binom{\kappa_1+\kappa_2}{\kappa_2+q}}\, p^{(1)}_{\kappa_1 q} p^{(2)}_{\kappa_2 - q}, \tag{3.7}$$

with $\kappa_< = \min(\kappa_1\kappa_2)$. This still classical result is subsequently transferred into a quantum mechanical expression by canonical quantization - the spherical multipole moments $p^{(1)}_{\kappa q}$ and $p^{(2)}_{\kappa q}$ become spherical multipole operators $\hat{p}^{(1)}_{\kappa q}$ and $\hat{p}^{(2)}_{\kappa q}$, operating on the Rydberg electron of the first and second atom, respectively. The operators are of the form

$$\hat{p}^{(i)}_{\kappa q} = e\,\hat{r}_i^{\kappa} \cdot \sqrt{\frac{4\pi}{2\kappa+1}} \hat{Y_{\kappa q}}(\hat{\vartheta}_i, \hat{\varphi}_i)\ , \tag{3.8}$$

where $\hat{Y_{\kappa q}}(\hat{\vartheta}, \hat{\varphi})$ are spherical harmonics. Similarly, the electron wave function $\psi(r, \vartheta, \varphi)$ separates into a radial part $R_{nLJ}(r)$ and an angular part $Y_{LSJm_J}(\vartheta, \varphi)$ as a product state

$$\psi(r, \vartheta, \varphi) = R_{nLJ}(r) \cdot Y_{LSJm_J}(\vartheta, \varphi), \tag{3.9}$$

in total analogy to the Hydrogen atom because the potential is radially symmetric [77]. As a consequence, the radial and angular matrix elements in eq. (3.8) can be independently evaluated according to the general formalisms described in B.2 and B.3.

The multipole expansion in eq. (3.6) can be considered as a series expansion of the interaction potential in powers

$$\varrho = \kappa_1 + \kappa_2 + 1 \tag{3.10}$$

of the inverse interatomic distance R. Of course, as neutral atoms do not have a net charge, the lowest multipole moment in this power series is the dipole moment. Therefore the series expansion of the interaction potential only starts with $\varrho = 3$.

With this method calculation of the Rydberg-Rydberg interaction boils down to the evaluation of matrix elements up to a certain order and a large number of input states. Subsequent numerical diagonalization of the Hamilton operator of (3.2) gives the new eigenenergies and eigenstates in the presence of interaction.

Hitherto, for the theoretical modeling of Rydberg experiments it was mostly sufficient to calculate the interaction problem perturbatively [31, 78]. In doing so, only the lowest order in the interaction Hamiltonian (3.6) is taken into account. In the case of weak interactions, where the level shift caused by the interaction is much smaller than the splitting of nearby energy levels (perturbation theory is anyway only valid in this regime), the interaction induced energy shift is determined by second order non-degenerate perturbation theory and can be calculated by [79]

$$\Delta E_{int} = \sum_{i \neq j} \frac{|\langle \psi^i_{nLJm_J} | V_{dd} | \psi^j_{nLJm_J} \rangle|^2}{E_i - E_j}. \tag{3.11}$$

Here, V_{dd} denotes the dipole-dipole operator resulting from evaluation eq. (3.6) only to the first order, i.e. for $\kappa_1 = \kappa_2 = 1$. The resulting $1/R^3$ dependence of V_{dd} manifests in a van-der-Waals type interaction of the form

$$V_{vdW} = -\frac{C_6}{r^6}, \tag{3.12}$$

where the C_6 coefficient is strongly scaling with the principal quantum number as $(n^*)^{11}$ and can be angular dependent [80].

In contrast, sec. (3.3.1) discusses an example where the higher order terms in the series expansion of eq. (3.6) become relevant and result in deviations from the van-der-Waals regime. The order at which the expansion series can be reasonably truncated in general increases with decreasing interatomic distance between the atoms. Then, the shift caused by the interaction exceeds the spacing of neighboring states.

3.2.1 *External fields*

Besides the high interaction among Rydberg atoms, the weak binding energy and the large extend of the electron wave function also result in a large sensitivity of Rydberg atoms to electric fields. This allow to precisely tune the energies of Rydberg atoms, for example to enhance interactions by tuning to Förster resonances where the interaction strength can be efficiently enhanced by the degeneracy of two Rydberg levels, see sec. (3.3.2).

Under the assumption that the electric field is static and homogenous, but points in an arbitrary direction with respect to the interatomic axis, the electric interaction energy takes the form

$$\hat{V}_\mathrm{e} = -\hat{\boldsymbol{d}} \cdot \boldsymbol{E} \quad \text{with} \quad \hat{\boldsymbol{d}} = e\hat{\boldsymbol{r}}, \tag{3.13}$$

where $\hat{\boldsymbol{d}}$ is the electric dipole operator. To calculate the interaction in the presence of an electric field, this term has to be added to the Hamiltonian of eq. (3.2). Care has to be taken as the electric interaction only acts on single Rydberg atoms and not on the pair state, thus the final Hamiltonian takes the form

$$\hat{H}(\boldsymbol{R}) = \hat{H}_0 + \hat{H}_\mathrm{int}(\boldsymbol{R}) + \hat{V}_\mathrm{e} \otimes \mathbb{1} + \mathbb{1} \otimes \hat{V}_\mathrm{e}. \tag{3.14}$$

In order make use of the formalism introduced in B.3 for the calculation of matrix elements, the electric field operator $\hat{V}_\mathrm{e}$ has to be transferred into the spherical basis $\{\boldsymbol{e}_\pm = \mp\frac{1}{\sqrt{2}}(\boldsymbol{e}_x \mp i\boldsymbol{e}_y),\ \boldsymbol{e}_0 = \boldsymbol{e}_z\}$. After the transformation the components of the electric field are given by

$$E_\pm = \mp\frac{1}{\sqrt{2}}(E_x \pm iE_y)\ ,\ E_0 = E_z. \tag{3.15}$$

This leads to the expression for the interaction of an atom with an electric field according to

$$-\hat{\boldsymbol{d}} \cdot \boldsymbol{E} = -e\,\hat{r} \cdot \sqrt{\frac{4\pi}{3}}\left(\hat{Y}_{1,0}E_0 - \hat{Y}_{1,1}E_- - \hat{Y}_{1,-1}E_+\right), \tag{3.16}$$

with spherical harmonics $Y_{\kappa q}(\hat{\vartheta}, \hat{\varphi})$.

To get an impression how an electric field interacting with a Rydberg atom changes the energy-levels of the atom, Fig. 3.2 shows a Stark-map in the vicinity of the $100S_{1/2}$ state of ^{87}Rb. For low angular momentum states with $L < 4$ the non-integer quantum defects lift the degeneracy of the different levels. For this reason, when the energy shifts

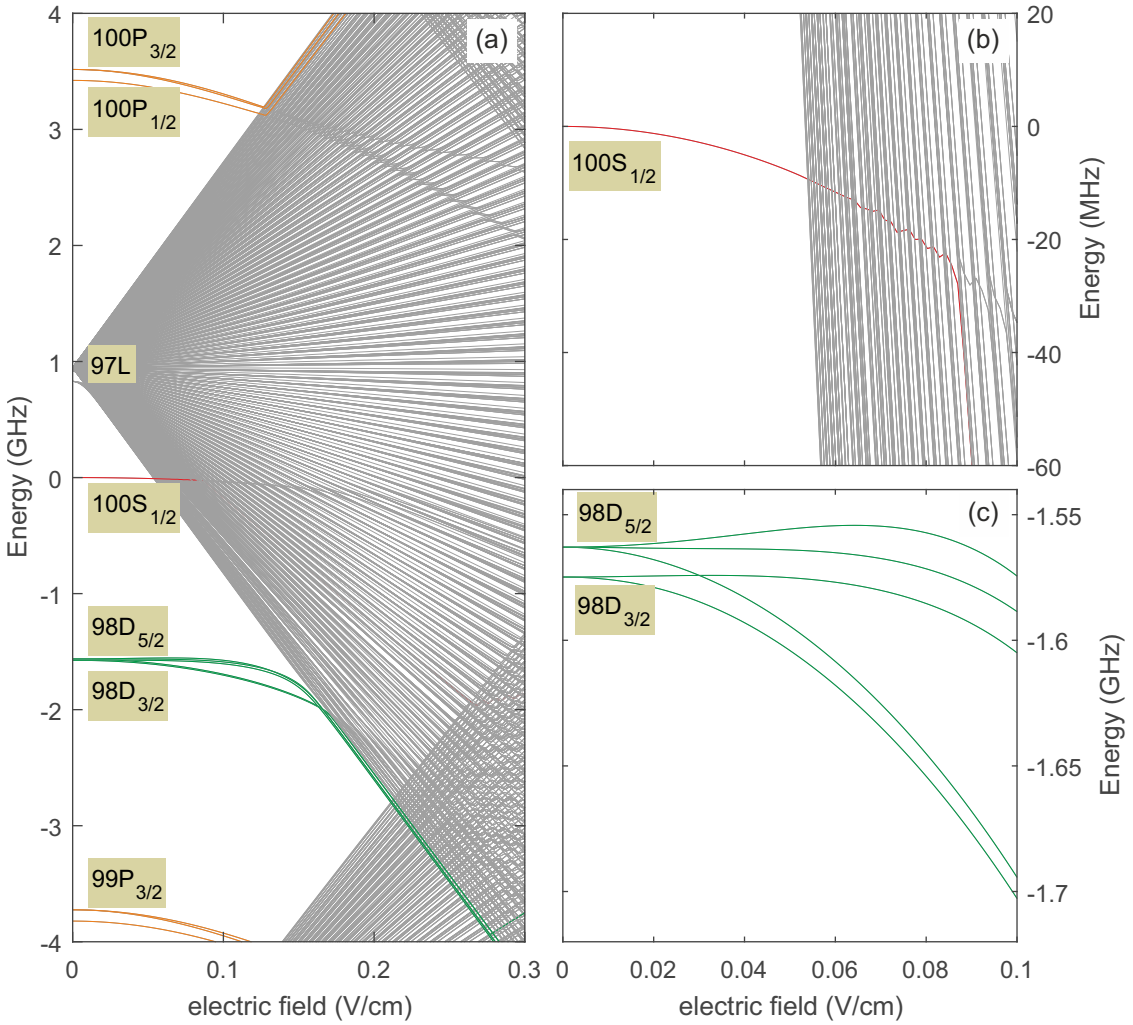

Figure 3.2: **Rydberg atoms in an electric field** (**a**) Stark map for ^{87}Rb in the vicinity of $100S_{1/2}$. The states with low angular momentum quantum number $L < 4$ show a quadratic Stark effect as the quantum defects δ_{nLJ} lift the degeneracy of the levels. On the other hand, high L states show a linear Stark effect as the levels are degenerate. (**b**)+(**c**) More detailed view of the Stark effect for $100S_{1/2}$ and $98D_{1/2}$. As these states are not degenerate, they obey a quadratic Stark effect until the manifold states mix in.

are calculated perturbatively, the first correction is provided by the second order term. As a consequence, the level shift

$$\Delta E_{\text{Stark}} = \frac{\alpha}{2}|\boldsymbol{E}|^2 \tag{3.17}$$

increases quadratically with the electric field. On the other hand, for high angular momentum states ($\delta_{nLJ} = 0$) degenerate perturbation theory has to be used. Mixing of states with different parity results in a nonzero first-order contribution. As a consequence, states with $L > 4$ experience a linear Stark effect. Both effects can be nicely seen in Fig. 3.2.

3.2.2 *Restriction of the basis size*

Calculation of the matrix elements and subsequent numerical diagonalization of the Hamiltonian (3.14) for different interatomic distances R yields the new eigenenergies and eigenvectors in the presence of interaction. Further evaluation yields potential curves in the presence of interaction and their overlap with unperturbed $|n_1 L_1 J_1 m_{J1}; n_2 L_2 J_2 m_{J2}\rangle$ pair states. From these quantities like e.g. the optical excitation strength for doubly excited Rydberg states can be derived. For highest precision this requires in principle inclusion of a large number of states and arbitrary orders in the multipole expansion. As a consequence the matrix presenting the interaction Hamiltonian becomes extremely large and numerical diagonalization impracticable. However exploitation of some symmetries and selection rules allows to shrink the basis size and make fast computation feasible.

One major restriction on the number of basis states is a direct consequence of the selection rules for the matrix elements in the multipole operator $\hat{p}_{\kappa q}$. These are listed in table 3.2, derived from the symmetry properties of the spherical harmonics $\hat{Y}_{\kappa q}(\vartheta, \varphi)$.

quantum number	**selection rule**
principal quantum number n	no restriction
angular momentum L	$L \to \begin{cases} L' \pm 0, 2, ..., \kappa & \text{for even } \kappa \\ L' \pm 1, 3, ..., \kappa & \text{for odd } \kappa \end{cases}$
total angular momentum J	$J \to J' \pm 0, 1, ..., \kappa$ with $J + J' \geq \kappa$
magnetic quantum number m_J	$m_J \to m'_J + q$ with $q \in \{-\kappa, -\kappa + 1, ..., \kappa\}$

Table 3.2: **Selection rules for multipole operators** The selection rules for the single atom matrix elements $\langle nLJm_J|\hat{p}_{\kappa q}|n'L'J'm'_J\rangle$ of the multipole operators $\hat{p}_{\kappa q}$ allow a reduction of the number of basis states taken into account for the interaction calculation. These selection rules are calculated from the symmetry properties of the spherical harmonics $\hat{Y}_{\kappa q}(\vartheta, \varphi)$.

On top, the rotational symmetry about the interatomic axis results in the conservation of the projection of the total angular momentum onto the interatomic axis. As for the calculations interatomic axis and quantization axis are identical, the total magnetic quantum number $M = m_{J1} + m_{J2}$ is conserved as well, limiting the size of the basis even more.

Further cutoff criteria have to be determined individually and depend on the particular interaction problem which has to be solved. The scaling of eq. (3.6) with the inverse interatomic distance to the power of ϱ suggests that it is reasonable to limit the orders in the multipole expansion. Especially for large interatomic distances it is sufficient to include only dipole-dipole interaction. Only with decreasing distance R between the Rydberg atoms, higher order terms in the series expansion become relevant. Sec. (3.3.1)

discusses an experiment, where higher orders in the multipole expansion lead to new features.

The possibility to restrict the order ϱ also implies to reduce the difference ΔL of the angular momentum (see table 3.2. However, attention has to be paid when an electric field is included (compare Fig. 3.2). The strength of the dc-Stark effect strongly depends on the degenerate manifold states with $L > 4$, thus restriction of L falsifies energy levels in this case.

Furthermore, Fig. 3.3 reveals that the radial matrix elements $\langle nLJm_J|r|n'L'J'm'_J\rangle$ and $\langle nLJm_J|r^2|n'L'J'm'_J\rangle$ showing up in the dipole-moment and quadrupole-moment operators peak around $n = n'$. This observation allows to take into account only states with a small difference in principal quantum number. This criterion goes hand in hand with limiting the maximum energy difference between pair sates, motivated by the form of the perturbatively calculated interaction energy (eq. (3.11)).

Due to this large number of possible constraints, the convergence of the calculation has to be tested for each Rydberg interaction problem individually. If necessary, the basis size has to be increased until convergence is reached. An elaborate discussion on this topic is provided in [68].

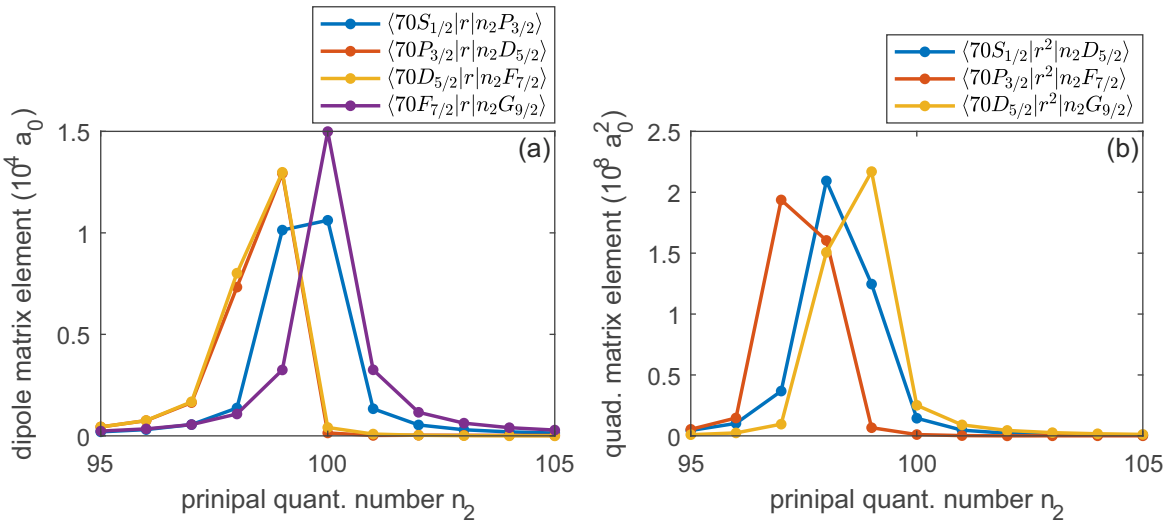

Figure 3.3: **Numerically calculated radial matrix elements** (**a**) Radial dipole matrix elements for rubidium for different dipole transitions $\langle n_1L_1J_1|r|n_2L_2J_2\rangle$ with $n_1 = 100$ and varying principal quantum number n_2. (**b**) Radial quadrupole matrix elements for different quadrupole transitions $\langle n_1L_1J_1|r^2|n_2L_2J_2\rangle$ at fixed $n_1 = 100$. The strong decrease of the matrix elements with large differences $\Delta n = n1 - n2$ legitimates the restriction of the basis size by the principal quantum number n.

3.2.3 *Angular dependent Rydberg interaction*

As mentioned before, the derivation of $V_{\kappa_1\kappa_2}$ given in eq. (3.7) requires alignment of the interatomic axis $\boldsymbol{R}$ with the z-axis (quantization axis) of the coordinate system in which the interaction is calculated. On the other hand, in an experiment the quantization axis

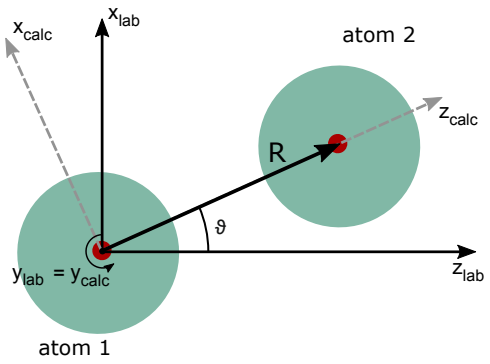

Figure 3.4: **Rotation of the coordinate system** For a pair of atoms whose interatomic axis R is not parallel to the z-axis of a lab-coordinate system, eq. (3.7) cannot be applied. However, first performing the calculations in a coordinate system C_{calc} and subsequent rotation of the results by an angle ϑ around $\mathrm{y_{lab}} = \mathrm{y_{calc}}$ allows to perform the calculation. To do so, the atoms have to be placed in the xz-plane.

is defined by e.g. the propagation direction of excitation lasers or the direction of strong magnetic fields. In a three-dimensional geometry, the interatomic axis of a pair of Rydberg atoms can thus enclose an angle ϑ with the quantization axis. As a consequence the expression for $V_{\kappa_1\kappa_2}$ is more complicated such that the evaluation of the multipole operators becomes more involved.

Alternatively, the calculations can be simplified by choosing an appropriate coordinate system C_{calc} for the calculation, in which the condition for the validity of eq. (3.7) is satisfied. Subsequently the results can be rotated into the lab-coordinate system C_{lab} by a proper choice of rotation matrices. If C_{lab} is chosen such, that the atoms are lying in the xz-plane, transformation into the coordinate system for the calculation requires rotation by an angle ϑ around the y-axis (Fig. 3.4). The states $|nLJm_J\rangle_{\mathrm{lab}}$ and $|nLJm_J\rangle_{\mathrm{calc}}$, in the lab-coordinate system respective the coordinate system for the calculation, are then related via Wigner-d-matrixes [81]

$$|nLJm_J\rangle_{\mathrm{lab}} = \sum_{m'_J} d^J_{m_J m'_J}(\vartheta)\, |nLJm'_J\rangle_{\mathrm{calc}}\,. \tag{3.18}$$

I.e. the states in the lab-coordinate system are superpositions of the states in the fixed coordinate system. As a consequence, the total magnetic quantum number $M = m_{J1} + m_{J2}$ is not preserved any more. This means, that different Zeeman spinstates couple under the presence of interaction [80]. In chapter 6 it will be shown that this influences the nonlinearity in experiments applying an EIT scheme to Rydberg D-states.

3.3 APPLICATIONS OF THE RYDBERG POTENTIAL CALCULATION

This section discusses two examples where the full calculation of the Rydberg interaction is relevant for recent experiments. Comparison with experimental results enables validation of the numerical results and demonstrates the applicability of full potential calculations to state-of-the-art experiments. It also allows to benchmark the influence of the basis size and of the truncation order on the interaction potentials.

3.3.1 *Relevance of higher-order multipole terms and basis size*

The relevance of multipole terms in the interaction potential of order higher than dipole-dipole, i.e. $\varrho > 3$ in equation (3.10), has been highlighted in several recent experiments [82, 83, 84, 68]. One example among many others is the observation of Rydberg aggregation dynamics in a vapor cell at room temperature by Urvoy *et al.* [84]. In this experiment, the high atomic densities and the spectral width of the laser pulses allow to probe Rydberg interaction at short interatomic distances. The main observation of this experiment is that the correlated excitation of Rydberg atoms is driven by the dipole-quadrupole ($\varrho = 4$) contribution to the interaction.

More specifically, this experiment investigates the Rydberg excitation in a Cesium vapor cell. The excitation is driven by a two-photon scheme with a detuning of $\Delta = \omega_{\text{Laser}} - \omega_{\text{Atom}} = -2$ GHz with respect to the $32S$ Rydberg state. Only including terms with $\varrho = 3$ in the multipole expansion corresponding to dipole-dipole coupling, results in a repulsive van-der-Waals type interaction, shown in Fig. 3.5 (a). This suggests that the presence of a Rydberg atom does not influence the probability to excite another Rydberg atom with the red-detuned excitation lasers.

However, when dipole-quadrupole interaction ($\varrho = 4$) is included in the series expansion, several close-by pair states are admixed to the $|32S_{1/2}; 32S_{1/2}\rangle$ pair state. This results in additional potential lines appearing both at lower and higher energies compared to the addressed state (Fig. 3.5 (b)). Following [84], the admixture of $|32S - 32S\rangle = |32S_{1/2}, m_J = 1/2; 32S_{1/2}, m_J = -1/2\rangle$ to any Rydberg pair state $|\psi\rangle$ is quantified by $\varepsilon_{|32S-32S\rangle}(\Delta) = |\langle\psi|ss\rangle|$. The calculated admixtures are shown in the color coding in Fig. 3.5. Any admixture at the detuning Δ of the excitation lasers results in efficient optical excitation of additional Rydberg atoms at specific distances to a first seed excitation. In particular, Urvoy *et al.* identified the resulting resonances at $R/R_{\text{LR}} \approx 2.1$ (where R_{LR} is the Le Roy radius) as the dominant underlying mechanism for the correlated Rydberg aggregation observed in the experiment [84].

Based on this finding, an obvious question is how additional multipole orders further modify the interaction potential. Fig. 3.5 (c), shows the resulting potential map when one more order in the series expansion is taken into account, this corresponds to the $\varrho = 5$ term including up to quadrupole-quadrupole and dipole-octuple interactions. While the admixture at the position relevant for the experiment remains almost unchanged, significant effects occur only at small interatomic distances $1 < R/R_{\text{LR}} < 1.7$, for example in the detuning region between 2 GHz and 4 GHz.

For better comparison, Fig. 3.5 (d) shows the for the experiment relevant quantity $\varepsilon_{|32S-32S\rangle}(\Delta = -2 \text{ GHz})$ for the three different potential calculations ($\varrho = 3, 4, 5$). While the inclusion of the $\varrho = 5$ terms modifies $\varepsilon_{|32S-32S\rangle}$ at short distances, the main relevant resonance feature at $R/R_{\text{LR}} \approx 2.1$ is not modified compared to the expansion up to $\varrho = 4$. Thus, the quantitative differences in the potential landscape due to the next higher-order terms do not affect the conclusions in [84].

In contrast, the features at small distances are relevant for example for formation of bound pair states of Rydberg atoms [85, 82, 86, 67, 87], requiring inclusion of even further

orders in the calculation [87, 68]. In general, when increasing ϱ, care has to be taken that the pair state basis truncation is appropriately adapted to include enough coupled states. The constraints used in this example on the difference in quantum numbers of the individual included Rydberg states are $\Delta n = 5$ and $\Delta L = 6$ with respect to the state $|32S_{1/2}, 32S_{1/2}\rangle$. These cutoff criteria are motivated by the selection rules for the different interaction orders and the scaling of the electric multipole matrix elements as discussed in sec. (3.2.2).

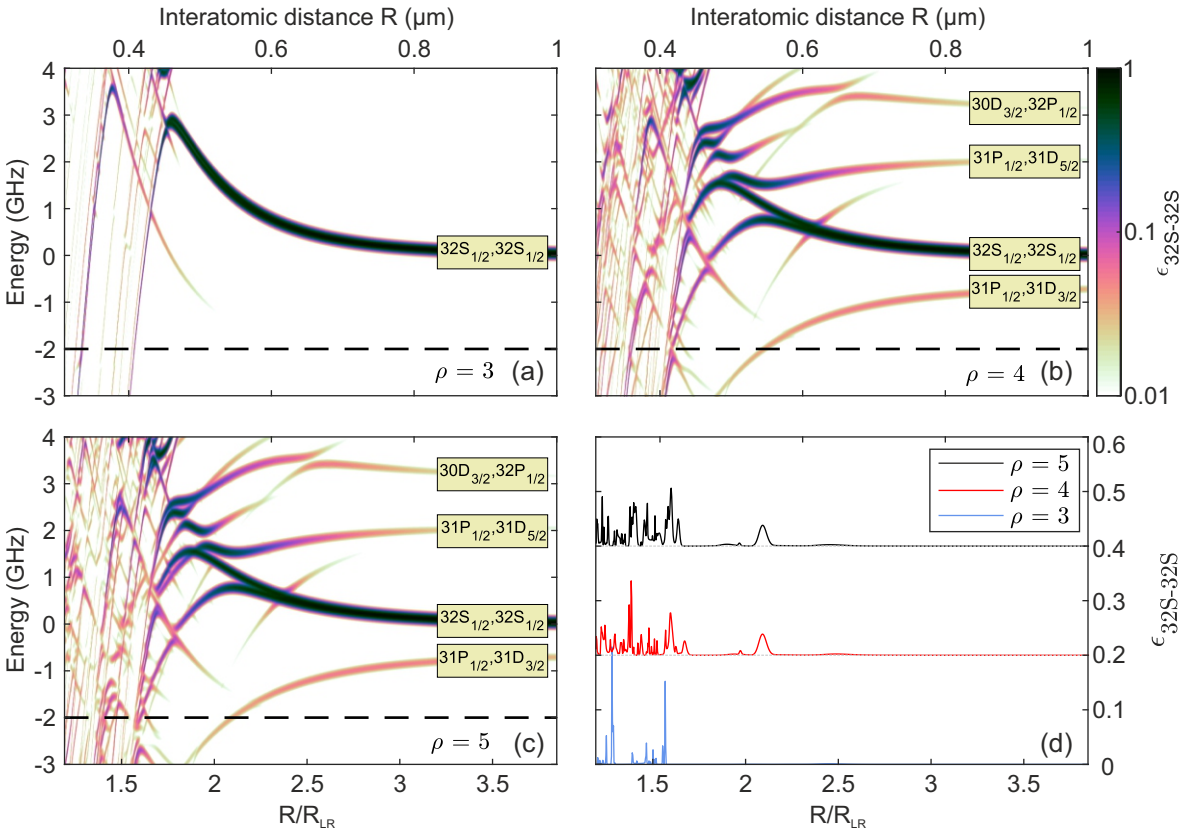

Figure 3.5: **Influence of higher order terms on the interaction potential** (**a**)-(**c**) Potential landscape around the unperturbed Cs $|32S_{1/2}; 32S_{1/2}\rangle$ state calculated up to order $1/R^{\varrho}$ in the interaction series. Specifically, the values chosen for the potentials are $\varrho = 3$ (a), $\varrho = 4$, (b) and $\varrho = 5$ (c). (**d**) Admixture $\varepsilon_{|32S-32S\rangle}$ to the perturbed pair states for a cut through the potential at a red detuning of $\Delta = -2$ GHz. Cuts for $\varrho = 4$ and $\varrho = 5$ are shifted by an offset of 0.2 and 0.4, respectively. The inclusion of the dipole-quadrupole term ($\varrho = 4$) results in the resonance feature at $R/R_{\mathrm{LR}} \approx 2.1$, which is identified in [84] as the dominant underlying mechanism for the experimentally observed formation of Rydberg aggregates.

3.3.2 *Angular dependence of the interaction near a Förster resonance*

The second example demonstrates the calculation of anisotropic Rydberg interactions in the presence of electric fields, as discussed in sec. (3.2.1) and sec. (3.2.3). The calculations

are motivated by the beautiful experiments of Ravets *et al.* in [88]. Here, two single ^{87}Rb atoms were prepared in their ground state in two tightly focussed optical dipole traps. Both the distance R between the two atoms and the angle ϑ between the interatomic axis and the external fields could be precisely tuned. Using a two-photon excitation scheme, both atoms were excited to the $|59D_{3/2}, m_J = 3/2\rangle$ state by applying a π-pulse. In the pair state basis and at zero electric field, the state $|DD\rangle = |59D_{3/2}, m_J = 3/2; 59D_{3/2}, m_J = 3/2\rangle$ is detuned by 8.69 MHz from the state $|PF\rangle = |61P_{1/2}, m_J = 1/2; 57F_{5/2}, m_J = 5/2\rangle$. Due to the different polarizabilities of the states, both pair states could be tuned into degeneracy by applying a weak electric field of 34.3 mV/cm. With this approach, Ravets *et al.* were able to map out the angular shape of the electric dipole-dipole interaction between the two atoms [88].

More specifically, the strength of the interaction was measured by letting the two-atom system evolve after the Rydberg excitation and in the presence of the electric field. After a variable hold time, a second optical π-pulse coupling to the $|DD\rangle$ state was employed to bring the atoms back to their ground state. By measuring the ground-state population after the full sequence, the time-evolution of the $|DD\rangle$ Rydberg pair state population could be reconstructed. Performing this experiment for various angles ϑ and fixed distance $R = 9.1$ µm resulted in the beautiful dipole-dipole pattern of the interaction shown by the blue crosses in Fig. 3.6 (d).

This experiment is especially suited to benchmark the interaction calculation including finite electric fields and different angles ϑ. As a first example, Fig. 3.6 (a) and (b) show the interaction potentials obtained for $\vartheta = 0°$ (atoms aligned with respect to the external fields) and $\vartheta = 14°$, respectively. On top of the potential lines which are shifted by the interaction, here the probability $a_k = |\langle DD|\psi_k\rangle|^2$ to find an overlap of the initially prepared state $|DD\rangle$ with the new eigenstates $|\psi_k\rangle$ is shown. For $\vartheta = 0°$, Fig. 3.6 (a) shows that a two-level approximation is valid for most of the distances between 7 µm and 20 µm. Most importantly, at the experimentally relevant distance $R = 9.1$ µm, the system can be treated as a two-level system.

However, the situation changes already dramatically for an angle of $\vartheta = 14°$, where the two-level approximation breaks down. This is a consequence of the mixing of different fine structure states of the $|57F\rangle$ state and of different magnetic levels coupled for non-zero interaction angles as M is not conserved anymore.

From the calculated overlap probabilities a_k, it is straight-forward to calculate the coherent time evolution of an excited Rydberg state in the presence of interaction. When the interaction is turned on by jumping on resonance with the electric field, the time-dependent probability of being in the state $|DD\rangle$ is given by $p_{|DD\rangle}(t) = |\sum_k a_k \exp\left(i\frac{E_k}{\hbar}t\right)]|^2$. Examples for two different angles and $R = 9.1$ µm are shown in Fig. 3.6 (c). For $\vartheta = 0°$ the time evolution yields an undamped sinusoidal oscillation with a frequency of $\nu = 9.2$ MHz, corresponding to the splitting of the most strongly populated pair potentials. In the case of $\vartheta = 14°$ the significant coupling to multiple other pair states leads to a dephasing that effectively damps out the Rabi oscillations. These results agree very well with the experimental time-evolution reported in [88].

Fig. 3.6 (d), shows all frequencies contributing to the time evolution at an interatomic distance $R = 9.1$ µm and varying angles ϑ, obtained from the energy differences $E_m - E_n$ of the pair states overlapping with the initial state (red points). The size of each point encodes the relative weight of each frequency, which is proportional to $a_m \cdot a_n$. For comparison, the single frequencies at each angle ϑ extracted from the experiment are shown by the blue crosses. One can see that for $0° \leq \vartheta \leq 5°$ and for $55° \leq \vartheta \leq 90°$ the calculations find a single dominant contribution, which is in excellent agreement with the experimental data. In contrast, for angles outside these regions, the increased number of pair states contributing to the time evolution explains the damped oscillations measured in the experiment.

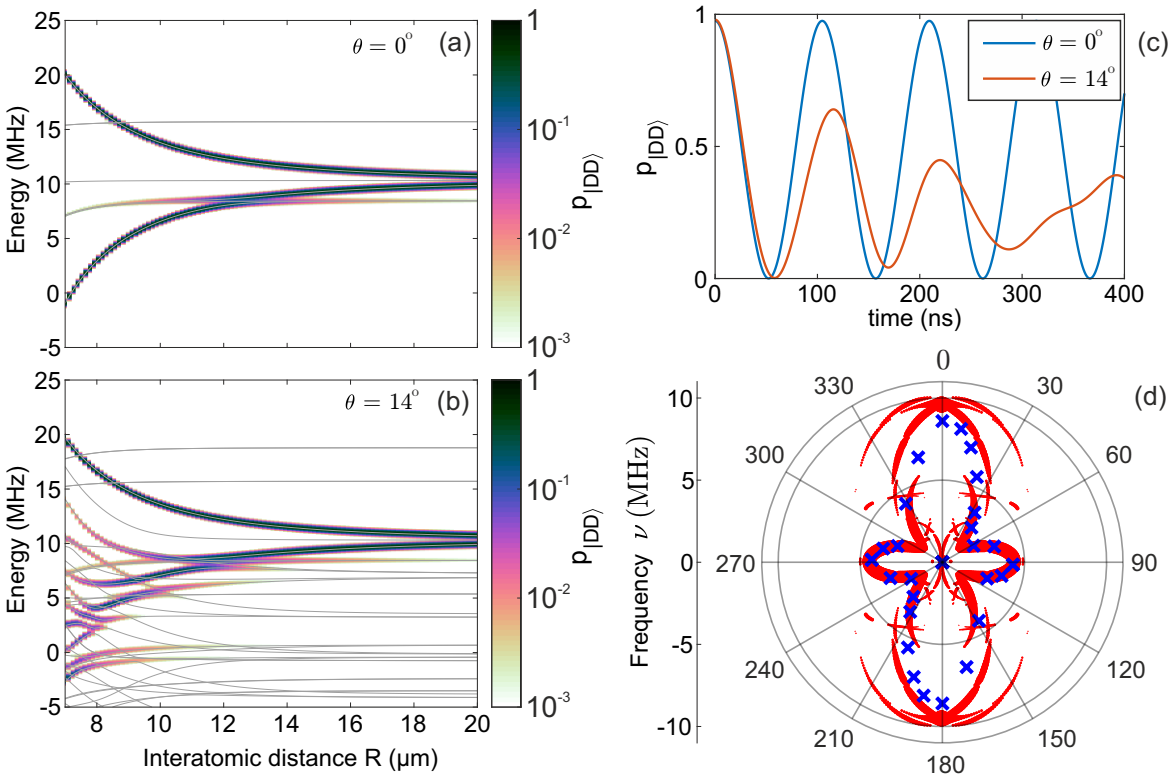

Figure 3.6: **Angular dependence of the Rydberg interaction in the presence of electric and magnetic fields** (**a**) Pair potential of the state $|DD\rangle = |59D_{3/2}, m_J = 3/2; 59D_{3/2}, m_J = 3/2\rangle$ tuned into Förster resonance with the state $|PF\rangle = |61P_{1/2}, m_J = 1/2; 57F_{5/2}, m_J = 5/2\rangle$ by applying an electric field of 34.3 mV/cm for $\vartheta = 0°$, i.e. both atoms aligned along the quantization axis. (**b**) Same pair potential as in (a) but calculated for an angle $\vartheta = 14°$ between the interatomic and the quantization axis. (**c**) Time evolution of the probability to find the system in the $|DD\rangle$ state in the presence of an electric field. For $\vartheta = 0°$ the probability $p_{|DD\rangle}(t)$ shows undamped oscillations with a frequency of 9.2 MHz. The multi level structure occurring at $\vartheta = 14°$ in (b) results in a damping of the oscillations due to dephasing (red line). (**d**) Angular dependence of the multiple oscillation frequencies out of the $|DD\rangle$ state. To illustrate how strong different frequencies do show up in the time evolution the size of the points encodes the relative weight of each frequency.

4 Photon interaction in an atomic three-level ladder system

Based on the description of interacting Rydberg atoms in chapter 3, this chapter will give a brief overview how these strong Rydberg interactions are used to mediate giant interactions between individual photons. In the first part of this chapter, a three-level ladder type atomic system is described, which is coupled by two laser fields, a weak probe field and a strong control field. Depending on parameters like detunings and intensities of the laser fields such a driven three-level system can exhibit rich physics.

This chapter first discusses the treatment of the coupled system including decay and dephasing processes via the common density matrix approach. Having found the time evolution of a single atom this allows to subsequently predict the transmission properties through an ensemble of atoms including absorption and diffraction. For a consistent notation throughout the thesis, the two distinct cases of *electromagnetically induced transparency* and *offresonant two-photon excitation* are introduced as they are applied in chapters 6 and 7. Finally the derived transmission properties of such a coupled three-level system are brought together with the results found in chapter 3 about interacting Rydberg atoms. In this context both the dissipative and dispersive *EIT* regime are discussed qualitatively and possible applications presented.

4.1 DRIVEN THREE-LEVEL SYSTEM IN THE DENSITY MATRIX APPROACH

The system mostly investigated throughout this thesis is illustrated in Fig. (4.1). A weak probe field Ω_p couples the atomic ground state $|g\rangle$ with the intermediate state $|e\rangle$, which in turn is coupled to the Rydberg state $|r\rangle$ by a strong control field Ω_c. To provide strong laser coupling the transitions $|g\rangle \leftrightarrow |e\rangle$ and $|e\rangle \leftrightarrow |r\rangle$ are dipole allowed, directly implicating that $|g\rangle \leftrightarrow |r\rangle$ is dipole forbidden. The detunings $\Delta_p = \hbar(\omega_p - \omega_{ge})$ and $\Delta_c = \hbar(\omega_{er} - \omega_c)$ present the energy differences between the coupling fields and the atomic transitions.
While the ground state is stable, both the intermediate and Rydberg states can decay with their respective decay rates $\Gamma_e \gg \Gamma_r$ determined by the natural linewidth. The decay rates result in population transfer from energetically higher lying states to lower lying states. Additionally, the dephasing terms γ_e and γ_r take into account effects like finite laser linewidth, atom-atom collisions or thermal movement reducing the coherence of the system.

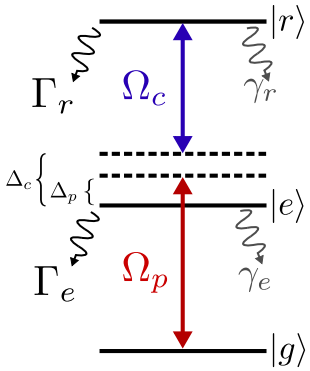

Figure 4.1: **Level scheme of a driven three-level system.** The ground state $|g\rangle$ in which the atoms are initially prepared is coupled to the Rydberg state $|r\rangle$ via a weak probe field Ω_p and a strong coupling field Ω_c. With respect to the atomic transitions the frequencies of the driving laser fields are detuned by Δ_p and Δ_c, respectively. On top of the coherent dynamics the system exhibits decay due to the natural decay rates Γ_e, Γ_r, but also dephasing with γ_e, γ_r caused by collisions and stray fields.

For modelling the system it is convenient to move to the dressed state picture where the different energies of the involved states and laser fields are reduced to the detunings Δ_p and Δ_c. Then, after applying the rotating wave approximation which neglects the fast rotating terms and moving into the rotating frame, the Hamilton operator describing the atom-light interaction of such a three-level system takes the form

$$H_{\text{3level}} = \frac{\hbar}{2}\begin{pmatrix} 0 & \Omega_p & 0 \\ \Omega_p & 2\Delta_p & \Omega_c \\ 0 & \Omega_c & 2(\Delta_c - \Delta_p) \end{pmatrix}. \tag{4.1}$$

The off-diagonal elements represent the strength of the light coupling in terms of a Rabi frequency $\Omega_j = -\frac{\boldsymbol{d}_j \mathcal{E}_j}{\hbar}$ where $\boldsymbol{d}_j$ is the dipole matrix element of the according transition and $\mathcal{E}_j$ the amplitude of the electric field driving the transition. Note that in the common literature two different conventions are used. Depending on the definition of the electric field in complex notation or using sin/cos the Rabi frequencies might appear as 2Ω instead of Ω. In this thesis all formulae are written in consistency with the notation specified in eq. (4.1).

Neglecting the decay- and dephasing effects the time evolution of the system can be determined by solving the time-dependent Schrödinger equation. However, when decay and dephasing terms are included, treatment by the density matrix approach allows both coherent and incoherent evolution to be accounted for. The density matrix of a single atom with the three discussed states is defined as

$$\rho = \begin{pmatrix} \rho_{gg} & \rho_{ge} & \rho_{gr} \\ \rho_{eg} & \rho_{ee} & \rho_{er} \\ \rho_{rg} & \rho_{re} & \rho_{rr} \end{pmatrix}, \tag{4.2}$$

where the diagonal elements represent the populations of the individual states and the off-diagonal terms are the coherences. The populations give the probability to find the

atom in a specific state at time t. As the total population has to be conserved the condition $\rho_{gg} + \rho_{ee} + \rho_{rr} = 1$ has to be satisfied for all times t, i.e. decay out of an excited state has to increase the population of a lower lying state. On the other hand, the value of the coherences in the density matrix are a measure for the phase relation between the different states. Vanishing coherences mean that the phase between two states is totally random such that no coherent processes, like Rabi oscillations, can be observed.

In the presence of the atom light coupling described by H_{3level} the time evolution of the density matrix is governed by the Lindblad Mater-equation

$$\frac{\partial}{\partial_t}\rho(t) = -\frac{i}{\hbar}[H, \rho] + \mathcal{L}(\rho). \tag{4.3}$$

where $[,]$ denotes the commutator of $\rho(t)$ and H_{3level}. The additionally introduced Lindblad operator $\mathcal{L}(\rho)$ comprises the effects resulting from the decay terms (Γ_e, Γ_r) and dephasing rates (γ_e, γ_r). The non-trivial derivation of this term is presented in [89], leading to

$$\begin{aligned}\mathcal{L}(\rho)/\hbar \;=\; & \begin{pmatrix} \Gamma_e\rho_{ee} & -\frac{\Gamma_e}{2}\rho_{ge} & 0 \\ -\frac{\Gamma_e}{2}\rho_{eg} & -\Gamma_e\rho_{ee} & -\frac{\Gamma_e}{2}\rho_{er} \\ 0 & -\frac{\Gamma_e}{2}\rho_{re} & 0 \end{pmatrix} + \begin{pmatrix} 0 & 0 & -\frac{\Gamma_r}{2}\rho_{gr} \\ 0 & \Gamma_r\rho_{rr} & -\frac{\Gamma_r}{2}\rho_{er} \\ -\frac{\Gamma_r}{2}\rho_{rg} & -\frac{\Gamma_r}{2}\rho_{re} & -\Gamma_r\rho_{rr} \end{pmatrix} \\ + \; & \begin{pmatrix} 0 & -\frac{\gamma_e}{2}\rho_{ge} & 0 \\ -\frac{\gamma_e}{2}\rho_{eg} & 0 & -\frac{\gamma_e}{2}\rho_{er} \\ 0 & -\frac{\gamma_e}{2}\rho_{re} & 0 \end{pmatrix} + \begin{pmatrix} 0 & 0 & -\frac{\gamma_r}{2}\rho_{gr} \\ 0 & 0 & -\frac{\gamma_r}{2}\rho_{er} \\ -\frac{\gamma_r}{2}\rho_{rg} & -\frac{\gamma_r}{2}\rho_{re} & 0 \end{pmatrix}. \end{aligned} \tag{4.4}$$

The first two parts in this representation of $\mathcal{L}(\rho)$ account for the contributions caused by the decay rates Γ_e and Γ_r. As the radiative decay only leads to a occupation of lower lying levels and as a consequence of the selection rules for dipole transitions, population can only decay from $|r\rangle$ to $|e\rangle$ and $|e\rangle$ to $|g\rangle$, respectively. Interestingly, the coherences only decay with half the decay rates.

Both the third and forth terms in $\mathcal{L}(\rho)$ include the dephasing mechanisms the system is exposed to. These parts take the same form except that the dephasing only affects the coherences and not the populations.

In principle, eq. (4.3) allows to calculate the full time evolution of all populations and coherences of the system. However, on timescales $t \gg \Gamma$ the system reaches a steady-state due to damping by the decay rates. In comparison, the experiments take place on a longer timescale, thus it is sufficient to calculate the steady state solution of eq. (4.3) with $\frac{\partial}{\partial_t} = 0$. These steady state results are discussed in the following sections for different parameter ranges of Ω_c, Δ_p and Δ_r in view of the experimental results of this thesis.

4.2 TRANSMISSION THROUGH AN ATOMIC MEDIUM

The density matrix approach described in the section before allows determining the evolution of the atomic states resulting from all coherent and incoherent atom-light interactions. The aim of this section is to find out how the back action of the atom-light coupling influences the laser fields. From the experimental point of view, in principle the transmission of both control and probe field could be monitored. As the control field however is only used to achieve strong coupling to the Rydberg state and all nonlinearities discussed within this thesis occur in the probe field, the discussion is restricted to the latter one.

In order to calculate the transmission properties of the probe field Ω_p self-consistently, one has to take into account the effect of the light-induced dipole moment of an atom onto the light field itself [90]. The induced dipole moment $\langle d \rangle$ is connected to the density matrix by

$$\begin{aligned} \langle d \rangle &= -e\boldsymbol{r} \\ &= -e \underbrace{\left(|g\rangle\langle g| + |e\rangle\langle e|\right)}_{=\mathbb{1}} \boldsymbol{r} \underbrace{\left(|g\rangle\langle g| + |e\rangle\langle e|\right)}_{=\mathbb{1}} \\ &= \mu_{eg}\rho_{eg} + \mu_{eg}^{*}\rho_{ge}, \end{aligned} \tag{4.5}$$

where $\mu_{eg} = \mu_{ge}^{*}$ is the dipole-matrix element of the $|g\rangle \leftrightarrow |e\rangle$ transition. The matrix elements $\langle e|\boldsymbol{r}|e\rangle$ and $\langle g|\boldsymbol{r}|g\rangle$ in eq. (4.5) vanish due to parity considerations. As each atom in an ensemble of N atoms confined in a volume V contributes with its induced dipole moment, a macroscopic polarizability $\boldsymbol{P}$ of the ensemble given by

$$\boldsymbol{P} = \frac{N}{V}\left(\mu_{eg}\rho_{eg} + \mu_{eg}^{*}\rho_{ge}\right) \tag{4.6}$$

can be defined. This approach is only valid if the ensemble satisfies some constraints. First of all, there must not be collisions between the atoms changing the internal state of the atoms. Second, the atoms should couple to different modes such that no coherent effects between the atoms occur. This sets a limit on the distance between the atoms which is given by the wavelength. It should be also noted at this point that in this derivation the polarization caused by all other atomic coherences, like e.g. ρ_{er} is completely negligible. This is only valid as long as the Rabi frequency of the probe is very weak and the population of the initial state ρ_{gg} is hardly changed.

Having found the polarizability induced in the atomic medium, its back action on the electric field is now governed by the wave equation for the electric field in a polarizable medium without charge sources which takes the form [73]

$$\left(\Delta - \frac{1}{c^2}\frac{\partial}{\partial t^2}\right) E(\boldsymbol{r}, t) = \frac{1}{\epsilon_0 c^2}\frac{\partial^2}{\partial t^2} P(\boldsymbol{r}, t). \tag{4.7}$$

A solution to the wave equation (4.7) are plane waves, which in the complex notation are given by

$$E(\boldsymbol{r},t) = \mathcal{E}_+(\boldsymbol{r},t)\exp[i(kz-\omega t)] + \mathcal{E}_-(\boldsymbol{r},t)\exp[-i(kz-\omega t)]. \tag{4.8}$$

For simplicity, the direction of propagation of this monochromatic wave (wave vector k) is limited to the z-direction. However, the amplitudes $\mathcal{E}_+(\boldsymbol{r},t) = \mathcal{E}_-(\boldsymbol{r},t)^*$ can vary in time and both the propagation direction and the transversal directions x and y. As the polarizability P in eq. (4.6) is induced by the electric field it has the same spatial and temporal dependence such that a proper expression is given by

$$P(\boldsymbol{r},t) = \mathcal{P}_+(\boldsymbol{r},t)\exp[i(kz-\omega t)] + \mathcal{P}_-(\boldsymbol{r},t)\exp[-i(kz-\omega t)]. \tag{4.9}$$

With these definitions for $E(\boldsymbol{r},t)$ and $P(\boldsymbol{r},t)$, the individual terms in eq. (4.7) read

$$\begin{aligned}
\Delta E(\boldsymbol{r},t) &= \left(\Delta + 2ik\frac{\partial}{\partial z} - k^2\right)\mathcal{E}_+(\boldsymbol{r},t)\exp[i(kz-\omega t)] + c.c. \qquad (4.10)\\
\frac{\partial^2}{\partial t^2}E(\boldsymbol{r},t) &= \left(\frac{\partial^2}{\partial t^2} - 2i\omega\frac{\partial}{\partial t} - \omega^2\right)\mathcal{E}_+(\boldsymbol{r},t)\exp[i(kz-\omega t)] + c.c.\\
\frac{\partial^2}{\partial t^2}P(\boldsymbol{r},t) &= \left(\frac{\partial^2}{\partial t^2} - 2i\omega\frac{\partial}{\partial t} - \omega^2\right)\mathcal{P}_+(\boldsymbol{r},t)\exp[i(kz-\omega t)] + c.c.
\end{aligned}$$

Under the assumption that focusing and diffraction can be neglected, which is a somewhat crude approximation as a dense atomic media can show strong lensing effects [91], the transversal terms can be neglected such that e.g. $\Delta\mathcal{E}_+(\boldsymbol{r},t)$ reduces to $\frac{\partial^2}{\partial z^2}\mathcal{E}_+(\boldsymbol{r},t)$.

Another justified assumption which holds for all the experiments described within this thesis is that the envelopes/amplitudes of the electric field only change slowly compared to the oscillation frequency ω. Mathematically this condition can be expressed by the terms

$$\begin{aligned}
k\mathcal{E}_\pm &\gg \frac{\partial\mathcal{E}_\pm}{\partial z} \qquad (4.11)\\
\omega\mathcal{E}_\pm &\gg \frac{\partial\mathcal{E}_\pm}{\partial t}\\
\omega\mathcal{P}_\pm &\gg \frac{\partial\mathcal{P}_\pm}{\partial t}.
\end{aligned}$$

This so-called *slowly varying envelope approximation (SVEA)* causes vanishing higher order derivatives in eq. (4.10)[92]. Using these approximations and $\omega = c\cdot k$, substitution of eq. (4.10) into the wave equation (4.7) leads to

$$\begin{aligned}
\left(\frac{\partial}{\partial z} + \frac{1}{c}\frac{\partial}{\partial t}\right)\mathcal{E}_+(\boldsymbol{r},t) &= \frac{ik}{2\epsilon_0}\mathcal{P}_+(\boldsymbol{r},t) \qquad (4.12)\\
\left(\frac{\partial}{\partial z} + \frac{1}{c}\frac{\partial}{\partial t}\right)\mathcal{E}_-(\boldsymbol{r},t) &= -\frac{ik}{2\epsilon_0}\mathcal{P}_-(\boldsymbol{r},t).
\end{aligned}$$

When only the spatial dependence of the electric field is considered, the solutions of these differential equations are governed by

$$\begin{aligned} \mathcal{E}_+(\boldsymbol{r}) &= \mathcal{E}_+(0) \cdot \exp\left(\frac{ik}{2}\chi z\right) + \text{const.} \\ \mathcal{E}_-(\boldsymbol{r}) &= \mathcal{E}_-(0) \cdot \exp\left(-\frac{ik}{2}\chi z\right) + \text{const.}, \end{aligned} \tag{4.13}$$

where χ is the electric polarizability which connects the induced polarizability $\boldsymbol{P}$ with the applied electric field $\boldsymbol{E}$ by

$$\boldsymbol{P} = \epsilon_0 \chi \boldsymbol{E}. \tag{4.14}$$

From this result and taking into account eq. (4.6) one directly finds that the transmission and refraction properties of an atomic system are determined by atomic density N/V, the dipole matrix elements $\mu_{eg} = \mu_{ge}^*$ and the coherences in the density matrix $\rho_{ge} = \rho_{ge}^*$. While the real part of χ results in a phase shift of the light travelling through the atoms, the imaginary part leads to absorption in the medium. Including the Rabi frequency $\hbar\Omega_p = -\mu_{eg}\mathcal{E}_+$, the resonant scattering cross section $\sigma_0 = \frac{3\lambda^2}{2\pi}$ and the decay rate $\Gamma_e = \frac{\omega^3 \mu_{eg}^2}{3\pi\epsilon_0 \hbar c^3}$ the spatial dependence of the intensity can be written as

$$\begin{aligned} I(\boldsymbol{r}) &= \frac{1}{2}\epsilon c \mathcal{E}_+(\boldsymbol{r})\mathcal{E}_-(\boldsymbol{r}) \\ &= I_0 \exp\left(-\frac{N}{V}\frac{\gamma}{\Omega_p}\sigma_0 \,\mathrm{Im}(\rho_{eg}) z\right), \end{aligned} \tag{4.15}$$

which results in an exponential decay of transmission through the atomic ensemble as the sign of $\mathrm{Im}(\rho_{eg})$ is always positive. From the experimental point of view, the transmitted intensity through an atomic medium with length L is of interest. Thus it is convenient to introduce the *optical density* OD as a quantity, which is determined by

$$OD = \frac{N}{V}\sigma_0 L. \tag{4.16}$$

Correspondingly reaching high OD either requires a long medium at relatively low atomic density or high atomic densities. Up to now, the derivation assumed a one dimensional medium which of course is a somewhat crude approximation for a realistic experiment. In reality the atomic density is a 3-dimensional quantity $n(\boldsymbol{r})$ superimposed with a probe field with Gaussian intensity distribution $I(\boldsymbol{r})$. As a consequence the *optical density* for such a geometry is determined by the integral

$$OD = \sigma_0 \int n(\boldsymbol{r}) I(\boldsymbol{r}) d\boldsymbol{r} \tag{4.17}$$

averaging over the different spatial distributions.

At the same time, and also according to the Kramers-Kronig relation, eq. (4.13) includes as well the dispersion properties the atoms impose on the probe field. A similar derivation as for the transmission yields the real part of the refraction index or equivalently the phaseshift

$$\delta\phi_{probe} = \frac{\Gamma_e}{2\Omega_p} OD \cdot \mathrm{Re}(\rho_{eg}) \tag{4.18}$$

which the probe light picks up when propagating through the medium compared to light traveling through vacuum.

4.2.1 *Application on a driven two level system*

In the absence of the control field Ω_c the Rydberg level $|r\rangle$ is uncoupled, such that the Hamilton (4.1) and the Lindblad (4.4) operators reduce to 2×2 matrices describing a two-level system. As the transmission properties of such a system are well-known (Lorentz model) it is an ideal candidate to test the derived formulae of eq. (4.15) and (4.18).

Solving the Master equation for the steady state of the density matrix provides

$$\rho_{eg,\mathrm{2level}} = \frac{i\Gamma_e(\gamma_e + \Gamma_e - 2i\Delta_p)\Omega_p}{\Gamma_e((\gamma_e+\Gamma_e)^2 + 4\Delta_p^2) + 2(\gamma_e+\Gamma_e)\Omega_p^2} \tag{4.19}$$

as solution of the relevant coherence in the density matrix. Based on some experimental parameters this expression can be further simplified. First, the experiments carried out in this thesis employ $|g\rangle = |5S_{1/2}\rangle$ and $|e\rangle = |5P_{3/2}\rangle$, realizing the strongest transition in ^{87}Rb with a decay rate $\gamma_e = 2\pi \cdot 6.05$ MHz [93]. At the temperatures of the atoms in a cold atom experiment, typically a few micro-kelvin, one finds a dephasing rate $\gamma_e < 2\pi \cdot 100$ kHz. Thus the sum terms $\Gamma_e + \gamma_e$ in $\rho_{eg,\mathrm{2level}}$ can be approximated by the decay rate Γ_e. Second, for all experiments carried out in the scope of this thesis the probe fields is very weak with a maximum value of $\Omega_p < 1$ MHz, allowing to neglect terms of the order $(\Omega_p/\Gamma_e)^2$. Under these approximations plugging eq. (4.19) into eqs. (4.15) and (4.18) yields

$$T_{\mathrm{2level}} = \exp\left(-\frac{OD}{1+4\frac{\Delta_p^2}{\Gamma_e^2}}\right) \tag{4.20}$$

and

$$\delta\phi_{\mathrm{2level}} = OD\frac{\Gamma_e\Delta_p}{1+4\frac{\Delta_p^2}{\Gamma_e^2}}. \tag{4.21}$$

As expected the absorption of the two-level system is well described by a Lorentzian in the absence of any inhomogeneous line broadening, plotted for different optical densi-

ties ($OD = 1, 10, 100$) in Fig. 4.2 (a). Although the linewidth Γ_e remains constant, for different values of OD the width of the absorption valley broadens due to saturation of transmission. Preparation of a dense atomic ensemble with $OD > 10$ thus allows blocking the transmission of probe photons over a wide range. Fitting eq. (4.20) to experimental data allows extracting the optical density of the atomic cloud. At the same time the derived phase shift ϕ_{2level} shows a anomalous dispersion relation (Fig. 4.2 (b)) as it is expected for a driven two-level system.

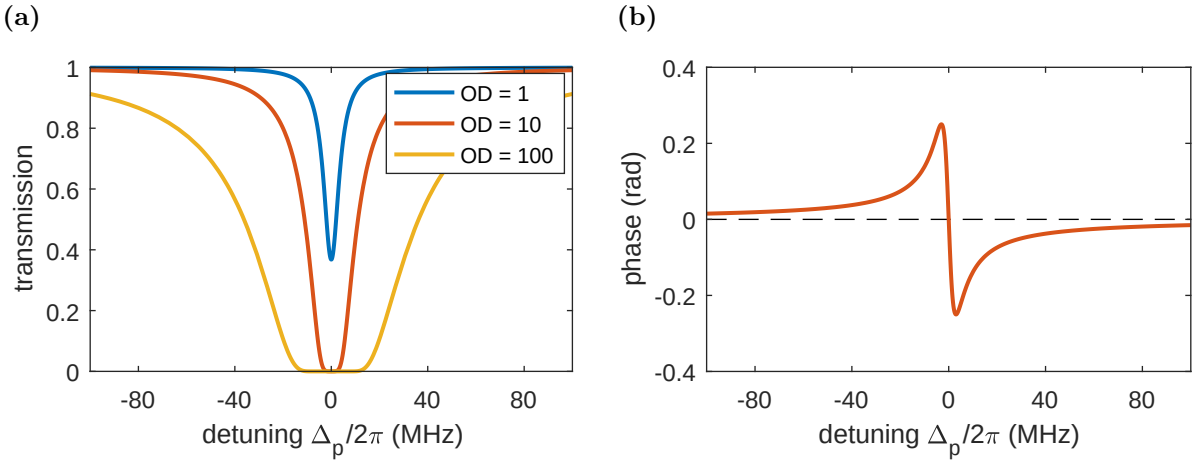

Figure 4.2: **Transmission properties with control field turned off** (**a**) Transmission spectrum of the probe beam through an atomic ensemble of ^{87}Rb atoms in the absence of the control field. The optical depth (OD) can be varied by changing the number of the atoms interacting with the probe beam leading to strong absorption. (**b**) The two-level system shows an anomalous dispersion with a maximum phase shift scaling linearly with the OD of the ensemble. For this reason only the result for $OD = 1$ is shown here.

4.3 ELECTROMAGNETICALLY INDUCED TRANSPARENCY

Having shown that the calculated equation for the transmission properties of the probe beam yield the correct results for the two-level system, in this section the properties of the full three-level system described in the first section of this chapter shall be discussed. To this end, the focus is first set to the regime of resonant *electromagnetically induced transparency* (*EIT*) which is realized when the probe field Ω_p and the control field Ω_c are resonant to their respective atomic transition, i.e. $\Delta_c = \Delta_p = 0$. Eq. (4.3) allows in principle to solve the Master equation analytically for arbitrarily chosen parameters, but the resulting expression for ρ is rather elaborate. Great simplification can be achieved in the *weak probe limit* assuming $\Omega_p \ll \Omega_c$ and $\Omega_p \ll \Gamma_e$. For the experiments within this thesis this approximation is well valid as the intensity of the probe field is only on

the order of a few photons per microsecond. A derivation in this limit is presented in the work of M. Fleischhauer *et. al.* [94], yielding the expression

$$\begin{aligned}\chi_{\mathrm{EIT}} &= \frac{\mu_{eg}^2 N}{\epsilon_0 \hbar V}\left(\frac{4\delta(\Omega_c^2 - 4\delta\Delta_p) - 4\Delta\gamma_{13}^2}{|\Omega_c^2 + (\gamma_{12} + i2\Delta_p)(\gamma_{13} + i2\delta|^2)}\right. \\ &+ \left. i\frac{8\delta^2\gamma_{12} + 2\gamma_{13}(\Omega_c^2 + \gamma_{13}\gamma_{12})}{|\Omega_c^2 + (\gamma_{12} + i2\Delta_p)(\gamma_{13} + i2\delta|^2)}\right)\end{aligned} \tag{4.22}$$

for the electric susceptibility χ_{EIT}. In this notation the expressions $\delta = \Delta_c - \Delta_p$, $\gamma_{12} = \gamma_e + \gamma_e$ and $\gamma_{13} = \Gamma_r + \gamma_r$ represent detunings and decay rates, respectively. For the experimental realization involving ^{87}Rb ground- and Rydberg- states, the decay rates can be approximated by $\gamma_{12} = \Gamma_e$ and $\gamma_{13} = \gamma_r$. This simplification is justified by the large intermediate state decay rate mentioned before dominating in ultra cold atoms over the ground state dephasing. On the other hand the long lived Rydberg states are easily perturbed by external influences like stray electric fields, justifying $\gamma_r > \Gamma_r$.

The absorptive and dispersive properties induced onto the probe field by χ_{EIT} are shown in Fig. 4.3 for different parameters. In comparison to the two level system discussed before, the probe field exhibits a transmission feature exactly on resonance $\Delta_c = \Delta_p = 0$ with the limit $T = 1$ for vanishing dephasing rate γ_r of the Rydberg state. The appearance of the narrow transmission window in the broad absorption valley resulting from the additional laser field coupling a third level is rather not intuitive but hides many fascinating properties.

From the equations derived for the probe transmission (eq. (4.15)) and the susceptibility χ_{EIT} two quantities which are somewhat important for the following part of this thesis can be calculated. First, the EIT transmission has a Gaussian line shape with a spectral width of

$$\delta\omega_{\mathrm{EIT}} = \frac{\Omega_c^2}{\Gamma_e}\frac{1}{\sqrt{OD}}. \tag{4.23}$$

In the absence of any decoherence rate γ_r of the Rydberg state the transmission peak can thus be arbitrarily narrow and still feature unity transmission (blue line). In the other limit it can be extremely broadened by a strong control field Ω_c. However, including a finite decoherence rate γ_r reduces the maximum transmission on EIT resonance to

$$T_{\mathrm{EIT}} = \exp\left(-\frac{OD}{1 + \frac{\Omega_c^2}{\Gamma_e\gamma_r}}\right). \tag{4.24}$$

As a consequence, at given γ_r and OD, not an arbitrarily low control Rabi frequency Ω_c can be applied anymore to still achieve reasonable transmission of the probe light. This effect is visualized in Fig. 4.3 by the yellow and red line showing the EIT transmission for $\gamma_r = 2\pi \cdot 200$ kHz at Rabi frequencies $\Omega_c = 2\pi \cdot 8$ MHz and $2\pi \cdot 16$ MHz.

By increasing Ω_c for higher transmission T_{EIT} according to eq. (4.23) the width of the feature will broaden. As will be demonstrated in sec. 4.5 the width of the EIT feature influences the strength of the Rydberg nonlinearity, such that in experiments a compromise between narrow linewidth and high transmission has to be found.

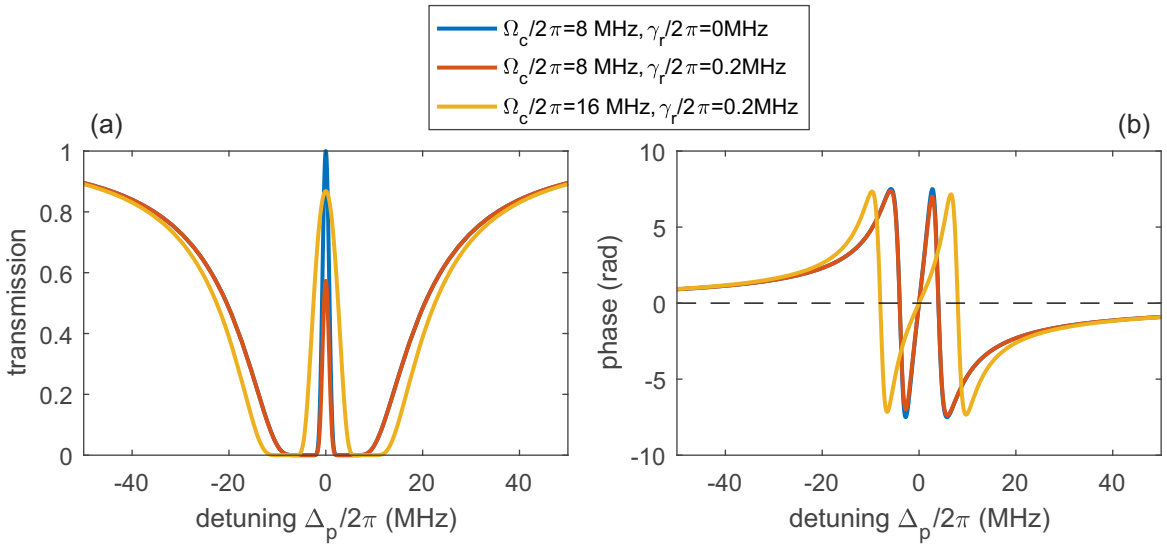

Figure 4.3: **Transmission properties when the control field is turned on (a)** Transmission spectrum of the probe beam through an atomic ensemble of ^{87}Rb atoms with a control field at different Rabi frequencies $\Omega_c = 2\pi \cdot 8$ MHz (blue line) and $\Omega_2 = 2\pi \cdot 16$ MHz (red, yellow line) at $OD = 30$. The presence of the control field renders the medium transparent when both laser fields are on resonance with the atomic transitions. For finite coherence of the Rydberg state γ_r the transmission on resonance decreases. (**b**) Apart from the medium being rendered transparent, the shape of the dispersive feature changes from anomalous to normal in the case of EIT. The steepness around resonance depends on the Rabi frequency Ω_c of the control light. This sharp dispersion causes slowing down of light pulses in the medium to group velocities of a few meters per second.

Experimentally, the effect of *EIT* was observed for the first time in 1986 in a strontium vapour [11]. This observation triggered a wide range of theoretical studies to understand this effect. Within this work, besides many distinct proposals for applications, different pictures came up to gain a more intuitive understanding of the phenomenon. Among different others a very intuitive view of EIT is given by S. Harris in [95]: When the coupling with the strong control field is considered in the dressed state picture, it results in new eigenstates $|\pm\rangle = \frac{1}{\sqrt{2}}(|e\rangle \pm |r\rangle)$ with energies $E_\pm = \pm\frac{\Omega}{2}$. Thus the probe field exhibits two resonances. This by itself does not explain why exactly in the center the medium becomes transparent. But it can be shown that on resonance the decay from the dressed states cancels out due to interference.

4.3.1 *Slow Light*

Besides the rendering the medium from opaque to transparent, the EIT regime holds another promising effect resulting from the modified dispersive properties. These are shown in Fig. 4.3 (b) for different parameters as phase shift $\delta\phi$. Compared to the dispersion of the two-level system discussed before in Fig. 4.2, the sign of the slope around resonance changes. Transmitted probe photons thus experience normal dispersion strongly affecting the propagation of a pulse inside the medium.

The propagation velocity of a light pulse inside a medium is governed by the group velocity v_g which is determined by

$$v_g = \frac{\partial\omega}{\partial k} = \left(\frac{\partial k}{\partial\omega}\right)^{-1} = \frac{c}{n(\omega) + \omega\frac{\partial n(\omega)}{\partial\omega}}, \tag{4.25}$$

where $n(\omega)$ is the index of refraction and c the vacuum speed of light c. For simplicity in the following $\gamma_r = 0$ is assumed resulting in $\mathrm{Im}(n) = 0$ as there is no absorption.

The presence of the derivative $\partial n(\omega)/\partial\omega$ in eq. (4.25) can result in extremely low group velocities in a medium with a steep normal dispersion. Remembering that the phase shift $\delta\phi = \frac{2\pi}{\lambda}(n_2 - 1)L$ picked up inside a medium resembles the refractive index, one finds from Fig. 4.3 (b) that EIT provides the required steep changes. Evaluating eq. (4.25) around resonance $\Delta_p = 0$ yields the expression [94]

$$v_g = \frac{c}{1 + \frac{N}{V}\sigma_0\frac{\Gamma_e}{\Omega_c^2}} \tag{4.26}$$

which results in a delay time of a probe pulse inside the medium of

$$\tau_{\mathrm{delay}} = OD\frac{\Gamma_e}{\Omega_c^2}. \tag{4.27}$$

In principle these equations show that by choosing a low value of Ω_c allows achieving extremely low group velocities. As seen before, this comes along with very narrow EIT transmission and also loss if at the same time γ_r does not vanish. When measuring the delay time of light pulses one therefore has to choose smooth pulses which are in the frequency domain more narrow than the EIT width $\delta\omega_{\mathrm{EIT}}$. So far a record speed of only 17 m/s was measured in a Bose-Einstein condensate of Sodium atoms in 1997 [10], though accepting large losses.

The reduction of the group velocity is accompanied by a spatial narrowing of the photon pulse during the propagation through the medium. As soon as the front part of a pulse enters the medium it gets slowed down. However, the part of the pulse still outside the medium moves with speed of light such that it "catches up", thus reducing the length of the pulse. When the experiment provides high enough OD it is possible to squeeze the

complete pulse inside the medium[1]. At the end of the medium the reverse process takes place such that the pulse recovers its original shape.

4.3.2 *Dark State Polaritons*

As a consequence of the low group velocity in a EIT medium Fleischhauer and Lukin introduced the picture of the Dark-state polariton which evolved to become a standard expression in the field of EIT [12]. Diagonalization of the Hamilton operator eq. (4.1) for $\Delta_c = \Delta_p = 0$ yields new eigenvectors of which one takes the form

$$|D_{\mathrm{EIT}}\rangle \;=\; \frac{\Omega_p|r\rangle - \Omega_c|g\rangle}{\Omega_p^2 + \Omega_c^2}, \tag{4.28}$$

e.g. its overlap with the intermediate state $|e\rangle$ is zero. For this reason this state is referred to as dark state. An atom in this state can not be transferred to $|e\rangle$, thus there is no fast decay Γ_e. When only the control field Ω_c is turned on the dark state is identical with the ground state $|g\rangle$. Sending now a probe pulse admixes some fraction of the Rydberg state $|r\rangle$ to the dark state. This process enhances the energy of the dark state. Due to energy conservation this energy has to be taken out of the light field. This means photonic character is changed into atomic excitation. After the probe pulse reached its maximum the process is reversed such that in the end the dark state becomes identical to $|1\rangle$ again.
Mathematically this picture is described by the dark state polariton

$$\Psi(z,t) = \cos(\vartheta)\mathcal{E}_p(z,t) - \sin(\vartheta)\sqrt{\frac{N}{V}}\rho_{gr}(z,t) \tag{4.29}$$

a superposition of electromagnetic field and atomic coherence. The ratio of the different terms is determined by the mixing angle $\tan^2(\vartheta) = \frac{N\sigma_0 c\Gamma_e}{V\Omega_c^2}$. For high density and small Ω_c for example, the character of the dark state polariton is dominated by the atomic character which explains the low group velocity in this case.

4.4 OFF-RESONANT TWO PHOTON EXCITATION

Apart from resonant EIT with $\Delta_c = \Delta_p = 0$ the driven three-level system can enter different regimes as well. Yet of relevance for this work is the regime where the condition $\Delta_c \gg \Omega_c, \Gamma_e$ holds. The transmission properties of this regime are shown for $OD = 30$ and a detuning $\Delta_c = 2\pi \cdot 100$ MHz for different parameters of Ω_c and γ_r in Fig. 4.4 (a). For $\gamma_r = 0$ the probe field experiences a strong absorption dip at approximately the detuning of the control field. At the same time Fig. 4.4 (b) shows a maximum in the population ρ_{rr} of the Rydberg state $|r\rangle$, i.e. photons of the probe field Ω_p are absorbed and converted into Rydberg atoms. This method to excite stationary Rydberg excitations

[1] A light pulse with a duration of 1 µs has in vacuum a spatial extend of 300 m. EIT inside a atomic ensemble can reduce this length to less than a millimeter

will be used in chapter 7 to subtract exactly one photon from the light field. For vanishing dephasing of the Rydberg state, the ultimate linewidth of the absorption line is in the limit $\Delta_c \gg \Omega_c$ solely given by the lifetime of the Rydberg state.

This scheme is used in many experiments for effective excitation of Rydberg atoms as it brings some advantages compared to direct excitation via UV light [64]. First, it allows addressing S- and D-Rydberg states which are not addressable by direct excitation with one photon as a consequence of the selection rules. Second, the effective Rabi frequency given by $\Omega_{\text{eff}} = \frac{\Omega_p \Omega_c}{2\Delta_c}$ can be extremely large by the right choice of parameters.

Finite decoherence γ_r plays a similar role in the off-resonant case as in the resonant EIT case discussed before. While before it resulted in imperfect transmission, in the off-resonant case the absorption probability decreases and the line broadens. For the parameters chosen in Fig. 4.4, $\Omega_c = 2\pi \cdot 8$ MHz and $\gamma_r = 2\pi \cdot 0.4$ MHz the absorption is already reduced roughly by a factor 2. If still strong absorption is required, this can be achieved by higher Ω_c at the cost of linewidth. For given parameters OD, Ω_c and γ_r the effective optical density attenuating the probe beam at Δ_p can be estimated by [51]

$$OD_{\text{Raman}} = \frac{\Omega_c^2}{4\Delta_c^2} \frac{\gamma_e}{\gamma_r + \Gamma_r} OD. \tag{4.30}$$

The difference in line positions for the Rabi frequencies $\Omega_c = 2\pi \cdot 8$ MHz and $\Omega_c = 2\pi \cdot 16$ MHz showing up in Fig. 4.4 is a consequence of the ac-Stark shift of the Rydberg level due to the control light. For efficient Rydberg excitation this ac-Stark shift has to be accounted for in the probe detuning. Thus, resonant two photon excitation of the Rydberg level is achieved for Δ_c at the probe detuning

$$\Delta_p \;=\; \Delta_c + \frac{\Omega_c^2}{4\Delta_c}. \tag{4.31}$$

However, also the regime $\Delta_p = \Delta_c$ is of interest for some applications, see sec. (4.5.2). Reason for the ac-Stark shift is the coupling of $|e\rangle$ and $|r\rangle$ by the control light. This does not only lead to a shift of these states but also to some admixing of the intermediate state to the Rydberg state. This admixing reduces the lifetime of the Rydberg state as the lifetime of the intermediate state is short. The strength of the admixing depends on Ω_c and Δ_c such that the decay rate of the Rydberg-level is given by

$$\gamma_{\text{Raman}} = \Gamma_e \left(\frac{\Omega}{2\Delta_c} \right)^2. \tag{4.32}$$

When long lifetimes of the Rydberg states are required, it is therefore necessary to work at large intermediate state detunings or if possible switch the control light off after the excitation. The reduction of the Rydberg lifetime due to admixing of the intermediate level is the main disadvantage of this two-photon excitation scheme compared to one-photon excitation with UV light.

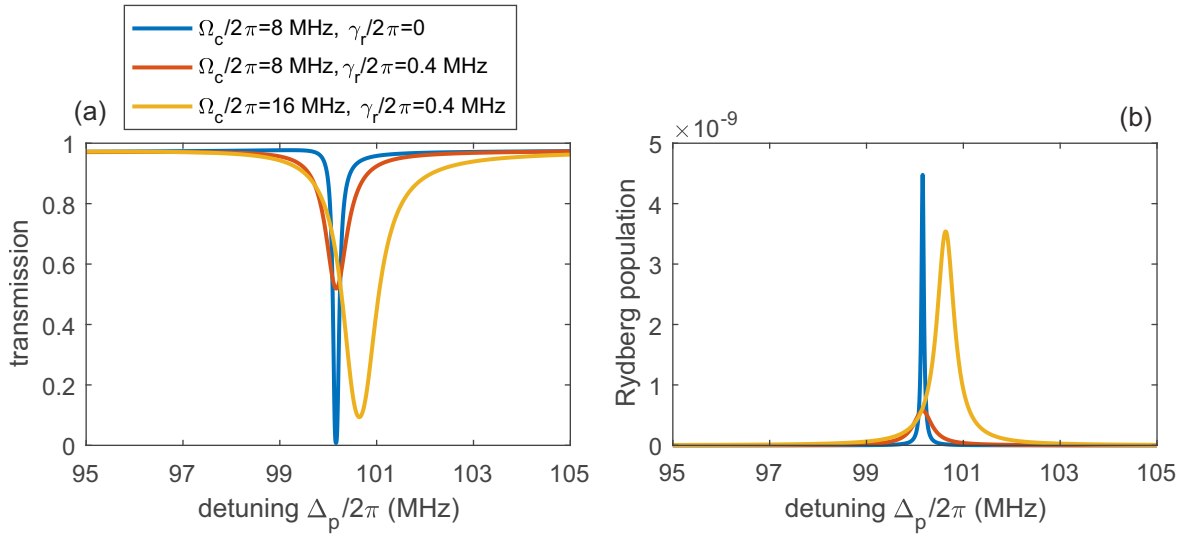

Figure 4.4: **Off-resonant Rydberg EIT**(**a**) Spectrum of the probe light for $OD = 30$ and $\Delta_c = 2\pi \cdot 100$ MHz. In the off resonant case the probe field is strongly attenuated close to $\Delta_p = \Delta_c$. Strength and width of the absorption are determined by Ω_c and γ_r. (**b**) The population ρ_{gg} of the Rydberg state shows a peak at the position of the dip in transmission of the probe field. This means that probe photons are absorbed and converted into Rydberg excitations.

4.5 RYDBERG MEDIATED PHOTON NONLINEARITIES

The equations derived In this chapter up to this point account only for the atom-light interaction, but not the interaction between atoms. On the other hand the introduction to interacting Rydberg atoms in chapter 3 revealed strong interactions between a pair of Rydberg atoms on a micro-meter length scale. Inclusion of these giant interaction effects between pairs of Rydberg atoms to the atom-light coupling leads to strong excitation blockade [25] investigated in numerous theoretical and experimental publications.

The principle of the excitation blockade is illustrated in Fig. 4.5 for two atoms interacting via *van-der-Waals* interaction when excited to the Rydberg state. The frequencies of the probe and control field are chosen such that they are on resonance with the $|g\rangle \leftrightarrow |e\rangle$ transition of *atom 1*. This allows transferring the population from $|g\rangle$ to $|r\rangle$. *Atom 2*, which is displaced from *atom 1* by a distance r, is addressed with the same laser field. For large distances where the Rydberg interaction is negligible *atom 2* is also resonant with the laser fields such that excitation to $|r\rangle$ is possible as well. For shorter distances however, the energy-shift V(r) has to be taken into account for the doubly excited state. Due to energy conservation, excitation of the doubly excited state can only occur when the energy shift V(r) is smaller than the excitation linewidth of the Rydberg state $|r\rangle$. The region were the excitation of a pair of Rydberg atoms is energetically forbidden is referred to as blockade region. For isotropic interactions this results in a sphere with radius r_b (blockade radius) which is defined as the distance where $V(r)$ and the excitation linewidth intersect.

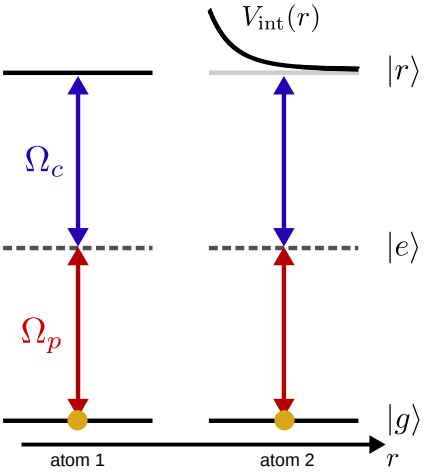

Figure 4.5: **Rydberg excitation blockade** For the explanation of the Rydberg excitation blockade two atoms separated by a distance r are considered. Via a two photon excitation the first atom is excited from the ground state $|g\rangle$ to the Rydberg state $|r\rangle$. For the excitation of a second atom the spatially dependent shift $V(r)$ of the Rydberg-Rydberg pair state has to be taken into account. Thus excitation of the double excited state is energetically forbidden when $V(r)$ exceeds the excitation linewidth.

A more profound treatment of the excitation of doubly excited Rydberg states can be found in sec. (6.2) in a more general context not restricted to the special case of van-der-Waals interaction.

Of course the excitation blockade influences both the excitation statistics of the atoms as well as the transmission properties of the light through an atomic ensemble. While the former is primarily investigated in the context of the realization of atomic qubits [21, 22], the latter gives rise to huge optical nonlinearities enabling the creation of non-classical states of light or toolboxes for all optical quantum computing.

4.5.1 *Dissipative Rydberg EIT regime*

Very efficient interactions between individual photons occur when EIT and interacting Rydberg atoms are brought together. As introduced in sec. (4.3.2) the photon pulse slowly travelling through the medium under EIT can be considered as a quasi-particle with partly photonic character and partly atomic character of a Rydberg atom. Two polaritons can however only propagate through the cloud at the same time when the distance between them is larger than the blockade radius r_b. Accounting for the EIT linewidth in eq. (4.23) and assuming van-der-Waals type interaction of the form $V(r) = \frac{C_6}{r^6}$ the blockade radius at given Ω_c is

$$r_b = \sqrt[6]{\frac{C_6 \Gamma_e \sqrt{OD}}{\Omega_c^2}}. \tag{4.33}$$

When two polaritons come closer than this distance, the level shift can be considered as a change of the resonance condition for the control light. This means the EIT condition $\Delta_c = \Delta_p = 0$ is not fulfilled anymore for two polaritons which are too close. Under the assumption that the transversal size of the system is smaller than r_b this renders the three-level system to an effective two-level system obeying strong scattering at the intermediate state with given OD, i.e. one of the polaritons gets lost due to scattering

at the intermediate state [36]. The result is a strong optical nonlinearity of the outgoing photon flux and anti-bunching in the temporal intensity correlation of the output [38].

Based on some simplifying assumptions both the nonlinear transmission and the photon statistics can be simulated by means of numerical Monte-Carlo simulations. The assumptions made for the results shown in Fig. 4.6 are a tiny medium which is blockaded by a single Rydberg atom, one-dimensionality and perfect blockade. The actual simulations are very similar to the ones described in chapter 7. First, a input pulse with a certain amount of time bins and Poissonian photon statistics is generated. Then, after a fist photon has been transmitted, all other entries in the time bins closer than a certain defined delay time are deleted (photons are scattered). After one delay time, the process of transmission and scattering is restarted. Fig. 4.6 (a) shows the input-photon-rate-dependent nonlinear transmission of this simulation for different delay times τ.

Fig. 4.6 (b) shows the cross-correlation function $g_2(\tau)$ obtained for pulses at a photon rate of $r_{in} = 2.5\ \mu\text{s}^{-1}$ and a delay time of $\tau_{\text{delay}} = 0.2\ \mu\text{s}$. While the reference signal reveals $g_2(\tau) = 1$ over the whole time range, the simulated transmitted signal shows the characteristic anti-bunching feature caused by the Rydberg interaction, occurring on the time given by the delay in the medium. In the simulation for the red data curve a second channel was introduced allowing the propagation of two polaritons side by side. This reduces the contrast of the anti bunching feature as the two different channels are not correlated. To measure non-classical light it is therefore important to implement an experiment with small transversal extend.

Comparison with experimental data [38] shows, that the assumptions made in the simulations discussed above are quite crude. Especially, when investigating the temporal width of the anti-bunching feature in the cross-correlation of the transmitted light, it turns out that this width is always on the timescale of the delay time inside the medium. This is very surprising, as for a medium longer than the blockade radius one would naively expect antibunching only for the time a polariton travels through the blockade region, given by $2r_b/v_g$. More advanced full calculations in which a two photon wave function is numerically propagated, taking into account the polariton wave equations, reproduce the experimental results correctly [43, 96].

4.5.2 *Rydberg mediated photon-photon phase shift*

Besides the dissipative EIT regime, where the Rydberg interaction leads to a blockade of the atomic medium by a single polariton for further incoming photons, the system described above can also be tuned to a dispersive regime. In this regime, the Rydberg mediated interaction does not lead to a saturation of transmission, but to a phase shift conditioned on the presence of a second photon [42, 41]. The principle is illustrated in Fig. 4.7. To work in the dispersive regime, the detuning of the control field is chosen to be offresonant from the $|e\rangle \leftrightarrow |r\rangle$ transition by a few times the intermediate state decay rate, in this example it is chosen to be $\Delta_c = 4\Gamma_e$. This results in additional absorption feature at $\Delta_p \approx \Delta_c$ (blue line in Fig. 4.7 (a)). When the probe detuning is set to $\Delta_p = 2\pi \cdot 24.7\,\text{MHz}$, as denoted by the dashed vertical line, the two-level

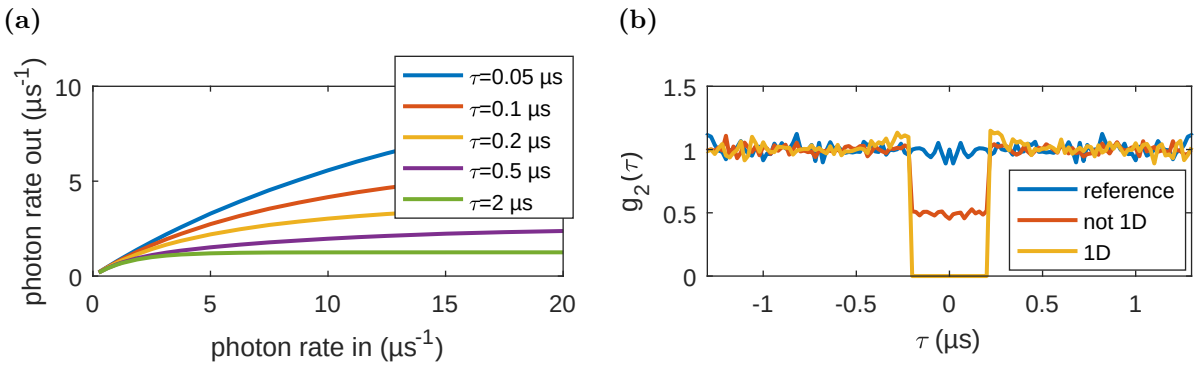

Figure 4.6: **Dissipative Rydberg EIT nonlinearities** (**a**) Simulation of the interaction mediated nonlinear transmission of photons through an atomic medium. In a fully blockaded medium, the transmission saturates at a input rate approximately given by the inverse of the pulse delay time inside the medium (τ_{delay}^{-1}). (**b**) Simulated g_2 cross-correlation function for a delay time $\tau_{\text{delay}} = 0.2$ μs. The EIT photon filtering of an input pulse with Poissonian statistics results in a train of photons coming out of the medium photon by photon. This leads to an antibunching effect on the timescale of the delay time inside the medium.

system which a second photon encounters in the presence of interaction has the same transmission. Unlike for the *dissipative* regime, the interaction has no influence on the transmission here. Interestingly, at this frequency the phase picked up in the two different cases can be, depending on Δ_c and OD, quite different. For the parameters presented in Fig. 4.7 the phase different is

$$\Delta\phi = \phi_{\text{interaction}} - \phi_{\text{no interaction}} = 1.81 \text{ rad} - (-1.81 \text{ rad}) = 3.62 \text{ rad}. \tag{4.34}$$

This large phase difference suggests Rydberg EIT in the dispersive regime to be an ideal candidate for the implementation of a controlled two qubit phase gate (cPhase gate). The difficulty for this step is to realize both a control and a target qubit, which in principle can be done by using different light polarizations (e.g. σ^+ and σ^-).

As discussed in chapter 5 it is experimentally feasible to couple only one light polarization to a Rydberg state. This allows coupling a target qubit $|0\rangle$ to a Rydberg state, while a second target qubit $|1\rangle$ is uncoupled. Storing a gate photon as a Rydberg excitation in the atomic ensemble before sending the target photon will result in the operations

$$\begin{aligned} |0\rangle &\rightarrow |0\rangle \\ |1\rangle &\rightarrow e^{i\phi}|1\rangle. \end{aligned}$$

By reading out the gate photon after the operation, it is possible to entangle gate and target photons and in principle realize high fidelity Rydberg based photonic quantum gates. Experimental dephasing mechanisms which impose a fundamental limit are discussed in sec. (5.3.2).

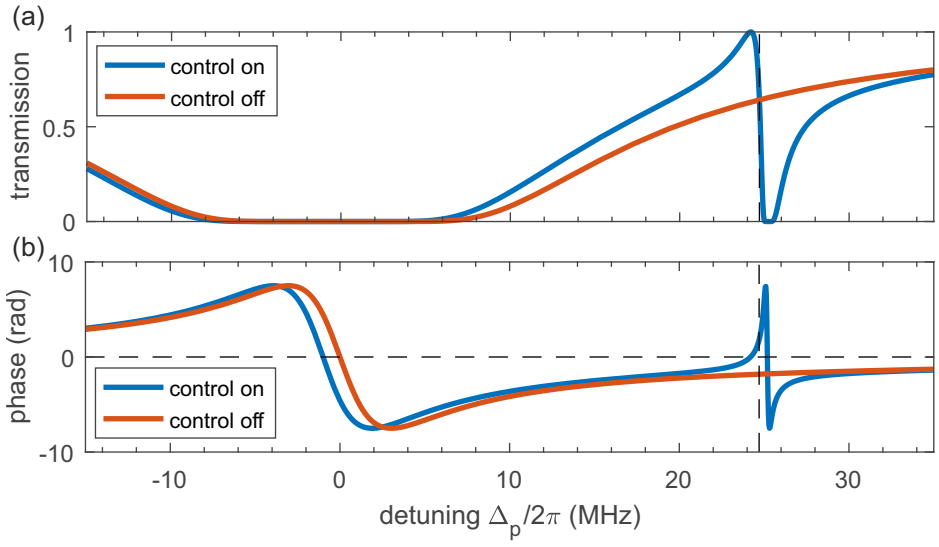

Figure 4.7: **Rydberg interaction mediated phase shift** (**a**) Transmission spectrum through an atomic sample with $OD = 30$ with applied control field with $\Omega_c = 2\pi \cdot 15$ MHz (blue) line and without control field (red line). The detuning of the control field is chosen to be $\Delta_c = 4\Gamma_e$. For these parameters, the two transmission lines intersect at $\Delta_p = 2\pi \cdot 24.7$ MHz, yielding same transmission for the two different cases. (**b**) The phase difference at the crossing point of the transmission lines is $\Delta\phi = 3.62$ rad for this set of parameters, however it is tunable by a different choice of Δ_c and OD.

Part II

EXPERIMENTAL RESULTS

Grau ist im Leben alle Theorie, aber entscheidend ist auf dem Platz!

Alfred Preißler,
Ehemaliger Fußballspieler

5 A system for interacting single photons

In chapters 3 and 4 the theoretical foundations for the promising application of Rydberg-mediated photon-photon interactions were discussed. Building on that, this chapter briefly summarizes both the experimental setup and the measurement procedures to probe the large optical nonlinearities. For this purpose, first the vacuum chamber for the preparation of a dense sample of ultra cold ^{87}Rb atoms by means of all optical trapping and cooling is introduced. Second, the manipulation techniques to address high lying Rydberg states are discussed, including the detailed excitations and detection schemes of photons and Rydberg atoms. Finally, a few basic results are shown to demonstrate the capability of this apparatus to perform applications in the field of quantum nonlinear optics. The description of the setup reduced to the minimally required information to understand the experiments in chapters 6 and 7. Especially many technical aspects can be found additionally found in the thesis of my PhD co-worker Hannes Gorniaczyk [97].

5.1 REQUIREMENTS AND SETUP OVERVIEW

The properties explained in chapter 3 and 4 set the conditions a setup designed to investigate Rydberg mediated photon nonlinearities in free-space without using a confining hollow core fiber or cavity has to fulfill. These are: a high optical depth on the transition $|g\rangle \leftrightarrow |e\rangle$, narrow excitation linewidths to achieve large blockade radii, a strongly focused probe beam to reach a one dimensional system size, high stability of electric fields and low temperatures of the atomic ensemble to obtain small dephasing rates.

One possible approach could be the usage of a vapour cell at room temperature [98, 99]. However, one limitation in such a system is the huge excitation linewidth due to Doppler/transit time broadening and motional dephasing caused by the high kinetic energy of the Rydberg atoms. For this reason interaction effects on the single photon level could not been shown so far in hot vapor experiments.

A contrary method is the application of the EIT technique onto a Bose-Einstein condensate, offering low temperatures and high densities. Yet, in a BEC it turns out that the extremely high atomic densities lead to inhomogeneous line broadening due to ground state atoms interacting with the Rydberg electron [100, 19].

Cold thermal atoms at densities around 10^{12} cm^{-3} are a good compromise between these two extreme cases. As of today, construction of the required vacuum apparatuses is state of the art. A layout drawing of the apparatus constructed during the scope of the thesis can be found in A.1. It consists of a vacuum chamber made of stainless

steel, to which a large glass cell providing excellent optical access from all directions is attached. An ion getter pump connected to the chamber sustains a constant pressure of $\approx 10^{-10}$ mbar. The pressure is mainly limited by background pressure of Rubidium atoms, which are released from dispensers driven with a current of $2\,\mathrm{A} - 4\,\mathrm{A}$. From the background pressure, atoms are directly loaded into a magneto-optical trap (MOT), which is located in the center of the glass cell. For this purpose, six laser beams with a diameter of 2.54 cm are passing through the chamber, cooling ^{87}Rb atoms on the $|5S_{1/2}, F = 2\rangle \leftrightarrow |5P_{3/2}, F = 3\rangle$ transition. After a loading time of ≈ 1 s around $5 \cdot 10^6$ are captured in the MOT and subsequently transferred into the optical dipole trap where they are further cooled and the shape of the atomic medium is arranged. Both the setup of the optical dipole trap and further cooling techniques are described in more detail in sec. (5.2.1) and sec. (5.2.2).

After the atomic sample has been produced following the procedure described above, the experiments are performed. For this purpose, the optical setup illustrated in Fig. 5.1 is built around the glass chamber. Each two 780 nm probe beams and 480 nm control beams are overlapped with the center of the atomic medium. To guarantee the one-dimensionality of the system for polariton propagation at Rydberg states with high principal quantum number, both probe beams are focused down to a beam waist of $w_{\mathrm{probe}} = 6.2\ \mu\mathrm{m}$. This is attained by two achromatic lenses with a focus length of 50 mm outside the glass chamber. In principle, an even smaller waist at the position of the atoms is desirable. This would allow working at lower principal quantum numbers and thus being less sensitive to fluctuations in the electric field. However, it requires either optics with a larger diameter or a lens with a shorter focal length inside the glass cell. The former is not possible as there are some spatial constraints mainly determined by the setup of the dipole trap (see sec. 5.2.1), the latter might pose a risk to the temporal stability of electric fields due to charges on the surface.

The control beams are overlapped with the probe beams using dichroic mirrors, but focused less strongly. A beam waist of $w_{\mathrm{control}} = 14\ \mu\mathrm{m}$ guarantees a quite homogeneous Rabi frequency Ω_c over the full width of the probe beam.

For the excitation of a single spin state a well-defined polarization of the excitation lasers is required. A detailed excitation scheme illustrating the polarizations to address Rydberg S- and D-states is provided in the thesis of Hannes Gorniaczyk [97]. As all laser used for the Rydberg excitation are guided to the experiment chamber using optical single mode fibers to filter the spatial mode, the polarizations are first filtered again using polarizing beamsplitter cubes (PBS). Subsequently, the light is send through quarter- and half-waveplates to obtain the desired polarization. As for the Rydberg excitation only σ^+ light for the lower transition and σ^+/σ^- for the upper transition are required, in principle only quarter-waveplates are necessary. Yet, the combination of both waveplates allows to compensate for birefringent optics in the setup, like e.g. the glass cell. For best performance the axis of all waveplates has to be aligned on the atomic spectrum.

After passing through the glass cell, both probe beams are collected again with non-polarization-maintaining single mode fibers. In a Hanbury Brown and Twiss setup, each

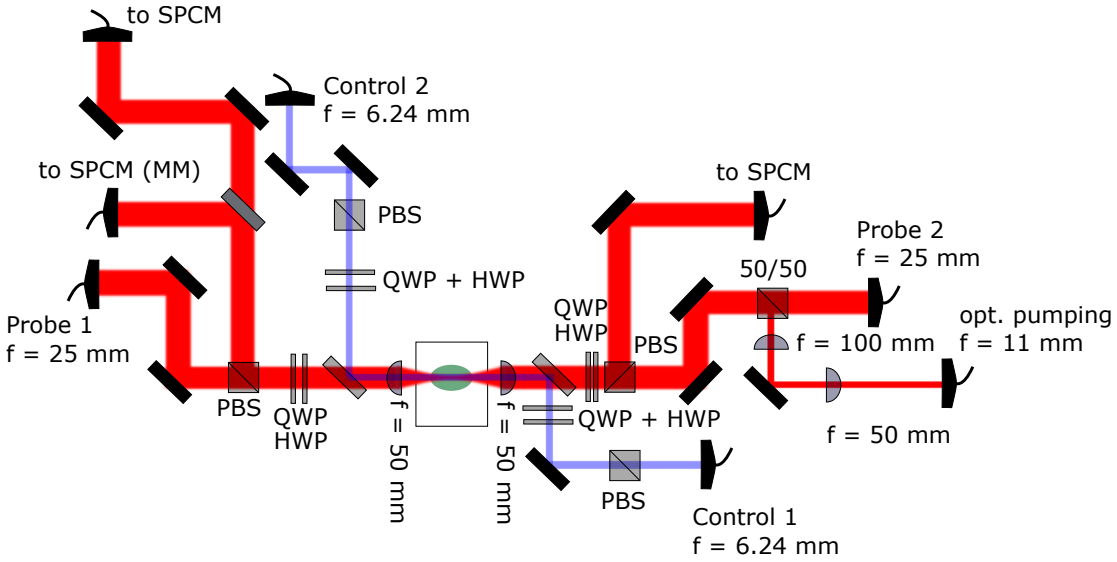

Figure 5.1: **Optical setup for probing Rydberg mediated optical nonlinearities** Sketch of the optical setup to measure the optical nonlinearities caused by the Rydberg-Rydberg interaction. Two 780 nm laser beams (Probe 1 + 2) are aligned to the center of the ultra cold atomic cloud with a waist of $w_{\text{probe}} = 6.2$ µm. The light transmitted through the vacuum chamber is collected by fiber coupled SPCM modules. For coupling to a Rydberg state, the probe beams are overlapped with two independent 480 nm control beams with a waist $w_{\text{control}} = 14$ µm. The polarization in each beam is adjusted by a pair of $\lambda/2$- and $\lambda/4$- waveplates.

beam is afterwards split and detected on two single photon counter modules [1,2] (SPCM). This techniques allows to measure temporal correlation functions of the transmitted light on timescales shorter than the dead time of the SPCM modules.

Both preparation of the atomic sample and probing of the nonlinearities require fast switching of laser fields, voltages and currents on the timescale of 10 ns. To this end, components like acousto-optical modulators (AOM) or power supplies for coils are controlled by a computer aided control system[3] featuring 32 digital and 16 analog channels. These channels can be programmed via a convenient graphical user interface (GUI), programmed by Michael Schlagmüller during his Ph.D. thesis [101]. This system is limited to a time resolution of 20 µs, which is fast enough for the preparation of the ultra cold atoms. On top, for driving fast pulses of the Rydberg lasers and gating of the SPCMs, a 24 channel digital pulse generator with a time resolution of 2 ns manufactured by *Swabian Instruments* is used[4].

For data acquisition, the TTL pulses of the photon counters indicating the detection of a photon, are tracked by a fast time tagger with a maximum time resolution of 20 ps[5] and saved on a data storage computer for evaluation.

[1]Laser Components, Count-250C-FC
[2]Excilitas, SPCM-AQRH-23 FC
[3]Jäger Messtechnik, Adwin II pro
[4]we used a first prototype, now available as Pulse Streamer 8/2
[5]Swabian Instruments, Time Tagger 20

Typical measurements to extract parameters of the setup are shown in Fig. 5.2. The optical density of the atomic cloud is determined by measuring a spectrum of the probe field across the resonance of the $|g\rangle \leftrightarrow |e\rangle$ transition in absence of the control field. Fitting eq. (4.20) to the data yields the resonant optical density. For the data presented in subfigure (a) the extracted value is $OD = 108$. Turning on the control field on resonance with the $|e\rangle \leftrightarrow |r\rangle$ transitions renders the medium for the probe beam from opaque to transparent. By a fit of the transmission based on the susceptibility in eq. (4.22), both the control field Rabi frequency $\Omega_c = 2\pi \cdot 11.4$ MHz and the dephasing rate $\gamma_r = 2\pi \cdot 103$ kHz of the Rydberg state can be extracted from this measurement.

Fig. 5.2 (b) presents a measurement of pulse arrival times at the photon detectors. In comparison to a reference pulse sent through the glass cell without medium, the maximum of the pulse transmitted through the atomic cloud on EIT resonance is delayed by $\tau_{\text{delay}} = 0.42$ µs. This value, obtained by fitting a Gaussian to the measured photon pulses, is in good agreement with the value $\tau_{\text{calc}} = 0.40$ µs predicted by eq. (4.27) for the experimental parameters $OD = 8.5$ and $\Omega_c = 2\pi \cdot 4.5$ MHz.

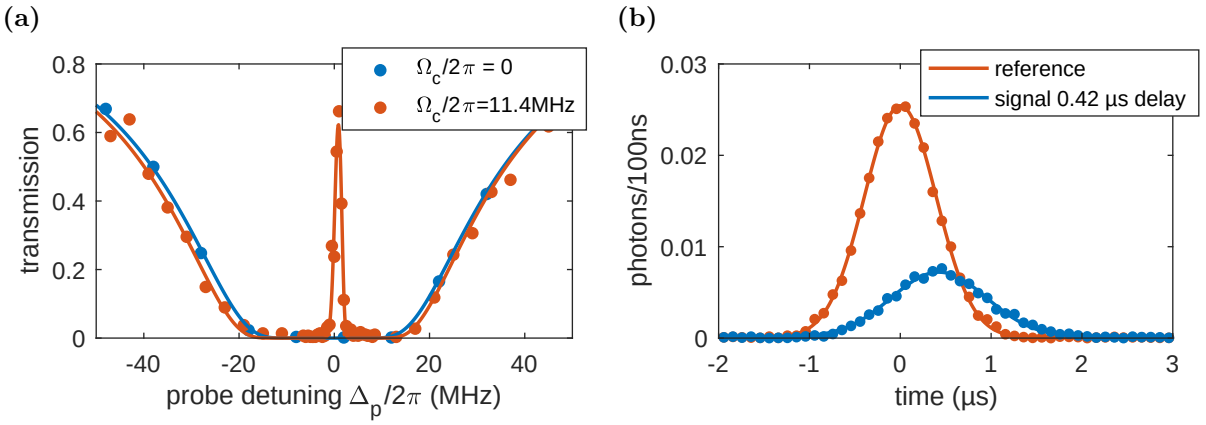

Figure 5.2: **Transmission measurements** (**a**) Frequency scan of the probe laser across the $|g\rangle \leftrightarrow |e\rangle$ resonance. In the absence of the control field the optical density on resonance is $OD = 108$. In the presence of a control field resonant to the $|e\rangle \leftrightarrow |r\rangle$ transition EIT occurs. (**b**) Measurement of the pulse delay on EIT resonance for $OD = 8.5$ and $\Omega_c = 2\pi \cdot 4.5$ MHz. The reduction of the group velocity due to the steep dispersion on EIT resonance results in a delay of $\tau_{\text{delay}} = 0.42$ µs of the signal pulse compared to the reference pulse.

5.1.1 *Laser system*

For preparation of the ultra-cold atomic ensemble and probing the nonlinearities different lasers are required. Depending on the exact transition, the linewidth of the laser driving the transition has to be on the order of a few kilohertz (for Rydberg excitations) to a few megahertz (ground state transitions). Apart from the laser light at 480 nm coupling

to the Rydberg state, all wavelengths required in the experiment for the preparation and manipulation of ultra cold ^{87}Rb atoms are sketched in Fig. 5.3. The involved frequencies differ mainly by the hyperfine splitting of the ground state $5S_{1/2}$ which is 6.835 GHz. In comparison, the splitting of the four hyperfine states of the first excited state $5P_{3/2}$ is comparatively small.

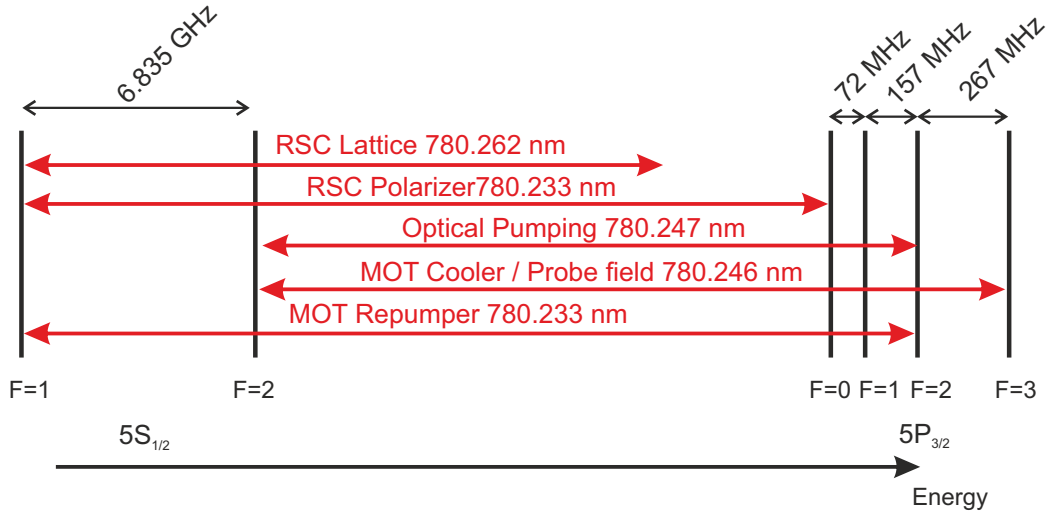

Figure 5.3: **Laser wavelengths required for preparation of cold ^{87}Rb atoms** Preparation of a cold atomic ensemble of ^{87}Rb requires a variety of wavelengths to address the different hyperfine structure levels F of both the ground state $5S_{1/2}$ and the first excited state $5P_{3/2}$.

For high experimental flexibility the different wavelengths are realized using six external cavity diode lasers which are set up on an additional table. Light is transferred to the main chamber with optical fibers, also yielding the advantage of a clean Gaussian mode. One of these lasers is stabilized onto an optical cavity with a high finesse of $\mathcal{F} = 15000$ by means of the Pound-Drever-Hall technique. This allows to narrow the frequency linewidth of this laser to approximately 5 kHz [102]. Due to this small linewidth and extremely good longtime stability, this laser serves as a frequency reference for all other lasers. For this purpose, of each laser a small fraction of light is overlapped with light of the master laser and focussed onto a fast ac-coupled photo diode[6] with a electronic bandwidth exceeding 8 GHz. These photodiodes allow to measure the beating pattern oscillating with the frequency difference of the two lasers. Fast feedback electronics using self-build PID controllers [101] allows to stabilize this beat pattern to a desired frequency provided by a stable rf-source[7]. Generation of the error signal which is required as input of the PID is on the one hand done by using delay line detectors [103] resulting in a linewidth of the beat pattern on the order of 100 kHz. This is stable enough for all applications involving only ground state transitions. On the other hand Rydberg transitions can be

[6] Hamamatsu G4176-03

[7] Typically the usage of direct digital synthesizers (DDS) is suggested

even more narrow. To be not limited by the laser linewidth resulting in a decoherence rate γ_r, the lasers used for Rydberg excitation are stabilized to the reference laser using a phase locked loop [104]. With this method, a linewidth of less than one kilohertz is achieved.

For fast switching of the laser light and pulses with arbitrary duration, shape and intensity, in each laser beam guided to the experiment an acousto-optical modulator (AOM) is used. Additional mechanical shutters allows to completely block leakage light when the AOMs are switched off.

5.1.2 *Electric Field Control/ Rydberg Ionization*

The calculation of dc-Stark shifts of Rydberg levels in sec. (3.2.1) has shown, that due to their large polarizability high lying Rydberg atoms are extremely sensitive to tiniest electric fields. Experimentally, this has two consequences. First, the position of the Rydberg line can shift over time. This makes measurements requiring a lot of statistics very time consuming as the position of the line has to be remeasured after short time intervals. Second, inhomogeneous electric fields result in an effective linebroadening affecting the strength of the interaction. To control both absolute field, direction of an applied electric field and electric field gradients, a steel construction composed of eight independent field plates is mounted inside the glass cell. The construction of this electric field control was part of the Master thesis of Johannes Schmidt [105], a scheme of the construction and how voltages are applied to generate a field in a certain direction is shown in A.2. Cancelling the electric field in all three direction of the laboratory coordinate system allows to reach narrow excitation spectra for high principal quantum numbers up to $n = 150$ with typical linewidths smaller than 1 MHz. Typically the day to day stability of the electric fields is on the order $\Delta E \approx 2\ \mathrm{mV/(cm)}$.

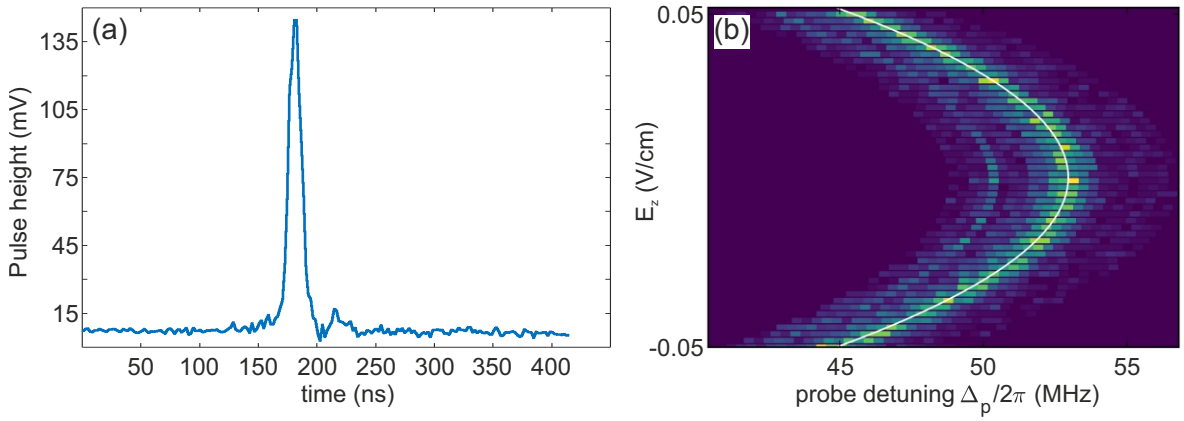

Figure 5.4: **Electric field control and ion detection** (**a**) Averaged signal of the MCP measured on a fast oscilloscope. (**b**) Stark map taken by varying the electric field. Such measurements are used in the experiment to calibrate and cancel electric fields.

At the same time, the in-vacuum electric field control also allows for another detection scheme of Rydberg (besides the optical detection via the probe light). Resulting from the weak binding energy of the Rydberg electron, a strong electric field pulse can be utilized to tear the Rydberg electron off the ionic core [106]. Subsequent detection of either Rydberg electron or ionic core with a ion-detector allows reconstructing the number of excited Rydberg atoms. To this end, to two of the electrodes a voltage up to 500 V can be applied which is sufficient to ionize Rydberg states with $n > 40$.

Fig. 5.4 (a) shows a typical trace of an ion count on the MCP measured on a fast oscilloscope. The good signal to noise ratio and the low ringing of the signal allow measuring this counts digitally on the same time-tagger as used for counting the clicks of single photon counters. In Fig. 5.4 (b) the ion signal of a Stark map measurement is presented. For each value of the electric field, the position of the Rydberg line is measured by scanning detuning of the probe laser over the resonance. From the electric field offset of the measured parabola stray electric fields can be determined and compensated.

5.2 PREPARATION OF A DENSE ATOMIC SAMPLE WITH TUNABLE SIZE

In section 5.1 the procedure of capturing and cooling atoms is already briefly summarized. Taking for granted, that the atoms have already been loaded into the MOT from the Rubidium background gas in the chamber, this section introduces the implementation of the optical dipole trap in the experiment and how it enables shaping the geometry of the atomic medium. Additionally, with the technique of *Raman sideband cooling* a method to efficiently cool atoms at a very low loss rate is introduced.

5.2.1 *Optical Dipole trap / dimple*

Trapping of atoms on a timescale of a few seconds is one of nowadays standard techniques in state of the art cold atom experiments. There are mainly two different approaches to realize this. On the one hand, magnetic traps offer a high robustness due to their mechanical stability and convenient cooling mechanisms by forced evaporation with radio- or microwave fields [107, 28]. With regard to Rydberg experiments, magnetic traps have the advantage that all low field seeking spin states of both ground state and Rydberg state can be trapped at the same time. Using optical dipole traps (ODT) [108, 109, 110] this requires to work at a so-called *magical wavelength* [111, 112], but then even all magnetic spin states can be trapped. However, although optical traps might lack some mechanical stability, their high flexibility concerning different trapping potentials gives a huge advantage over magnetic traps. Both depth and shape of the traps can be simply varied by the selection of beam shapes or laser intensities. As different experiments, as discussed in chapter 6 and 7, impose different needs on the shape of the atomic medium, it is evident that an ODT is the better choice. The geometry of the ODT used for the experiments in this thesis is illustrated in Fig. 5.5 (a). After the atoms have been loaded into the MOT, they are transferred into the crossed ODT consisting of two laser beams at a wavelength of $\lambda_{\mathrm{ODT}} = 1064\,\mathrm{nm}$ crossing under an angle ϑ. Loaded into this trap,

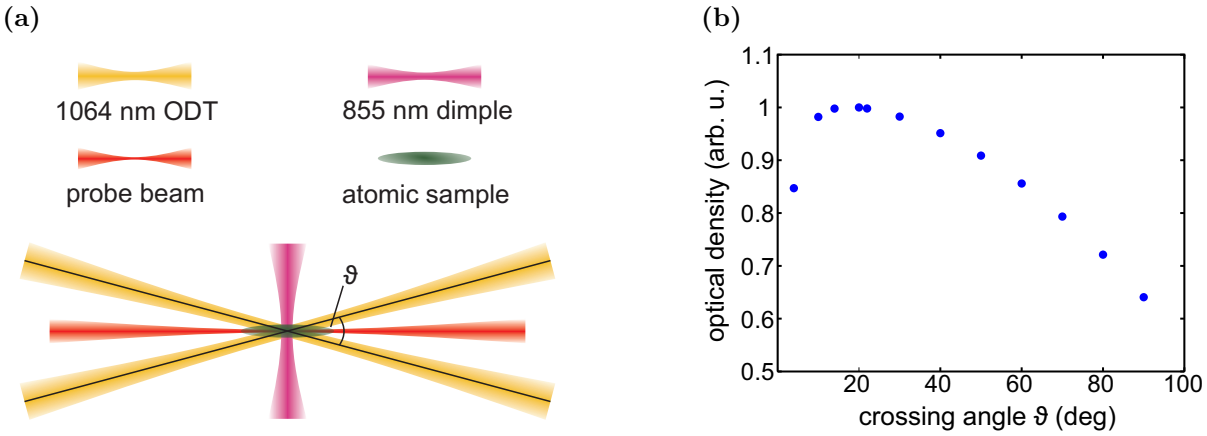

Figure 5.5: **Setup of the crossed optical dipole trap** (**a**) Configuration of crossed optical dipole trap at $\lambda_{\mathrm{ODT}} = 1064$ nm and dimple at $\lambda_{\mathrm{dimple}} = 855$ nm. (**b**) Calculated optical depth in the probe beam for an atomic sample trapped in the crossed ODT for different crossing angles ϑ. As the value of the total OD depends on the atom number in the trap, it is normalized to its maximum.

the atoms are subsequently cooled down to temperatures of $T \approx 5$ µK by means of forced evaporative cooling and Raman sideband cooling (sec. (5.2.2). Additionally, depending on the experiment in mind, the length L of the atomic cloud along the probe beam, can be altered using an additional dimple beam at $\lambda_{\mathrm{dimple}} = 855$ nm. In the following, properties as the landscape of the trapping potential or trap frequencies are calculated.

The principle of optical dipole traps is based on the ac-Stark shift imposed onto atoms [113] by a light field. The underlying mechanism stems from the atom-light coupling discussed in sec. 4.2, inducing a polarizability in an atom. While before the back action of the induced dipole moment onto the electric field was of interest, for all optical trapping one can assume that the number of photons is so much larger than the amount of atoms, such that these effects are negligible.

Treating the atom as a polarizable medium in a semiclassical approach, the induced dipole moment is given by $\boldsymbol{p}(t) = \alpha \boldsymbol{E}(t) = \frac{\epsilon_0 \chi}{N} \boldsymbol{E}(t)$, where $\alpha(t)$ is the polarizability of the atom. The energy in the laser field is thus given by

$$U_{\mathrm{dip}}(\boldsymbol{r}) = -\frac{1}{2}\langle \alpha(t) E(,\boldsymbol{r},t)\rangle = -\frac{1}{2}\,\mathrm{Re}(\alpha) I(\boldsymbol{r}), \tag{5.1}$$

where $I(\boldsymbol{r}) = \frac{1}{2}\epsilon_0 c |E(\boldsymbol{r})|^2$ is the intensity of the trapping laser. In the context of optical dipole traps the polarizability α is often calculated using the Lorentz model for a damped harmonic oscillator. However, the solution calculated in sec. (4.2) considering only two coupled levels leads to exactly the same result. Eq. (5.1) then takes the form

$$U_{\mathrm{dip}}(\boldsymbol{r}) = -\frac{3\pi}{2\omega_0^3} \cdot \frac{\Gamma}{\omega_0 - \omega} I(\boldsymbol{r}), \tag{5.2}$$

where ω_0 is the transition frequency of the atom and ω the frequency of the trapping laser. This potential results in a frequency and intensity dependent dipole-force $F(\boldsymbol{r}) = -\nabla U(\boldsymbol{r})$ on the atoms, which is

$$F_{\mathrm{dip}}(\boldsymbol{r}) = \frac{3\pi}{2\omega_0^3} \cdot \frac{\Gamma}{\omega_0 - \omega} \nabla I(\boldsymbol{r}). \tag{5.3}$$

From eq. (5.3) it becomes apparent, that the detuning $\Delta = \omega_0 - \omega$ plays a crucial role for the sign of the dipole-force. On the one hand for red detuning, when $\Delta < 0$, the dipole-force points towards the position of highest intensity. On the other hand a blue detuned laser field, $\Delta > 0$, results in a force pointing away from the position of highest light intensity. While traps for the latter case are much more difficult to realize experimentally, these traps offer the advantage that the trap does hardly influence the energy levels of inclosed atoms. On top, eq. (5.3) reveals that the dipole-force can be dramatically increased by working at small detunings Δ. However, since the scattering rate scales with $\left(\frac{1}{\omega_0-\omega}\right)^2 I(\boldsymbol{r})$ [113] this results in stronger heating. For this reason it is better to increase the dipole-force by using higher intensities of the laser field if affordable.

In a real atoms multiple levels are present, all contributing to the potential energy of a considered state. To take these into account, eq. (5.2) transforms to a sum over the contributions of different levels

$$U_{\mathrm{dip,total}}(\boldsymbol{r}) = -\frac{3\pi}{2} I(\boldsymbol{r}) \sum_i \frac{1}{\omega_{0,i}^3} \cdot \frac{\Gamma_{0,i}}{\omega_{0,i} - \omega}. \tag{5.4}$$

Here, $\omega_{0,i}$ and Γ_i are the energies and decay rates of the different included levels. The relevance of different states in the sum of eq. 5.4 depends strongly on both the scattering cross section of each level and the detuning of the ODT with respect to the particular state. For example, in Rubidium it is sufficient to include only D_1[8]- and D_2[9]-lines when calculating the trapping potential of the ground state in a $\lambda_{\mathrm{ODT}} = 1070$ nm trap. These transitions share both the smallest detuning and strongest coupling strength in Rb.

The total trapping potential generated by multiple lasers can be calculated by summing over the potentials of each individual laser. This allows modeling the trapping potential realized by the crossed ODT and the additional dimple in the experiment. As in the setup only Gaussian laser beams are used, the respective intensities $I(\boldsymbol{r})$ can be parameterized in the $\{x, y, u\}$ coordinate using a few parameters only, namely the total power P_{trap} of each beam, the beam waist in the focus w_{trap} and the pointing direction of the respective beam. Initially, from such calculations the angle ϑ enclosed by the beams of the crossed ODT was optimized for the highest OD in the probe beam provided by a given number of atoms. The dependence of resulting OD for the probe beam on the crossing angle ϑ is shown in Fig. 5.5 (b). Due to spatial constraints arising from the lenses focusing the probe beam a value of $\vartheta = 31°$ was realized in the experiment, which

[8] $|5S_{1/2}\rangle \leftrightarrow |5P_{1/2}\rangle$
[9] $|5S_{1/2}\rangle \leftrightarrow |5P_{3/2}\rangle$

is close to the ideal value occurring at $15° < \vartheta < 30°$.

Cuts through $z = 0$ of the according to eq. (5.4 calculated potentials of the geometry illustrated in Fig. 5.5 (a) are shown in Fig. 5.6 (a)+(b). The depth of the potentials is encoded in the colormap in units of MHz. In subfigure (a) the potential resulting from the crossed ODT is calculated for the experimental parameters $\vartheta = 31°$, $P_{\mathrm{ODT}} = 0.6\,\mathrm{W}$ and $w_{\mathrm{ODT}} = 37\,\mu\mathrm{m}$. With these parameters, the two laser beams result in an elongated potential along the y-direction, i.e. the direction along which the probe beam is propagating. Loading a large number of atoms in this potential results in a high optical depth for the probe beam.

The effect of the dimple beam becomes clear from Fig. 5.6 (b). The parameters for this calculations are again adapted to the experimental realization. While waist and angle of the crossed trap are the same compared to the calculations in subfigure (a), the power is changed to $P_{\mathrm{ODT}} = 0.3\,\mathrm{W}$. The parameters of the dimple are $P_{\mathrm{dimple}} = 200\,\mathrm{mW}$, $w_{\mathrm{dimple,y}} = 18\,\mu\mathrm{m}$ and $w_{\mathrm{dimple,z}} = 44\,\mu\mathrm{m}$. The different waists of the dimple in y- and z-direction are chosen to not decrease the size of the atomic cloud in the direction perpendicular to the probe beam which would result in weaker absorption. While the depth of the potential at these parameters remains approximately the same, the length of the potential along the z-direction changes dramatically.

In the vicinity of the trap center, the trapping potentials can be well approximated by a harmonic function $U_{\mathrm{harmonic}}(x, y, z) = \frac{1}{2} m \omega^2_{\{x,y,z\}}$, where $\omega_{\{x,y,z\}}$ are the trap frequencies. Plugging the Boltzman distribution $p(\boldsymbol{r}) = \exp(-U(\boldsymbol{r})/k_B T)$ into this harmonic potential allows to calculate a density profile for a given number of atoms at a mean temperature of T.

For the crossed ODT with the parameters introduced before, the trap frequencies are $\omega_r = 2\pi \cdot 690$ Hz and $\omega_y = 2\pi \cdot 190$ Hz, determined by fitting the harmonic approximation to the full calculation of the potential. At a atom number of $N = 25000$ atoms and a temperature of 5 μK typically achieved in this configuration, this results in cloud dimensions of $\sigma_r = 7.1\,\mu\mathrm{m}$ and $\sigma_y = 25.9\,\mu\mathrm{m}$. $sigma_y$ ad $sigma_r$, respectively, are defined as $1/e$-width of the Gaussian density distribution along and transverse the direction of the probe beam propagation. These calculated numbers are in good agreement with the cloud dimensions measured by absorption imaging, shown in Fig. 5.6 (c).

As discussed before, usage of the additional dimple beam modifies the trapping potential in y-direction. This mainly results in an increase of the trap-frequencies in this direction. For the potential shown in Fig. 5.6 (b), the trap frequencies are determined to be $\omega_y = 2\pi \cdot 1400$ Hz and $\omega_r = 2\pi \cdot 600$ Hz. In this configuration typically $N = 20000$ atoms can be loaded at a temperature of $T = 8\,\mu\mathrm{K}$ (this increase is due to stronger heating in the 855 nm light). The resulting dimensions are $\sigma_r = 11.0\,\mu\mathrm{m}$ and $\sigma_y = 4.8\,\mu\mathrm{m}$. These values are in less good agreement with the atomic densities obtained by absorption images from the experiment, shown in Fig. 5.6 (d). Main reason is that the absorption imaging optics in the experiment are not designed to resolve such small structures. This results for example in the brighter spot in the center of the dense region as a consequence of diffraction at the dense medium.

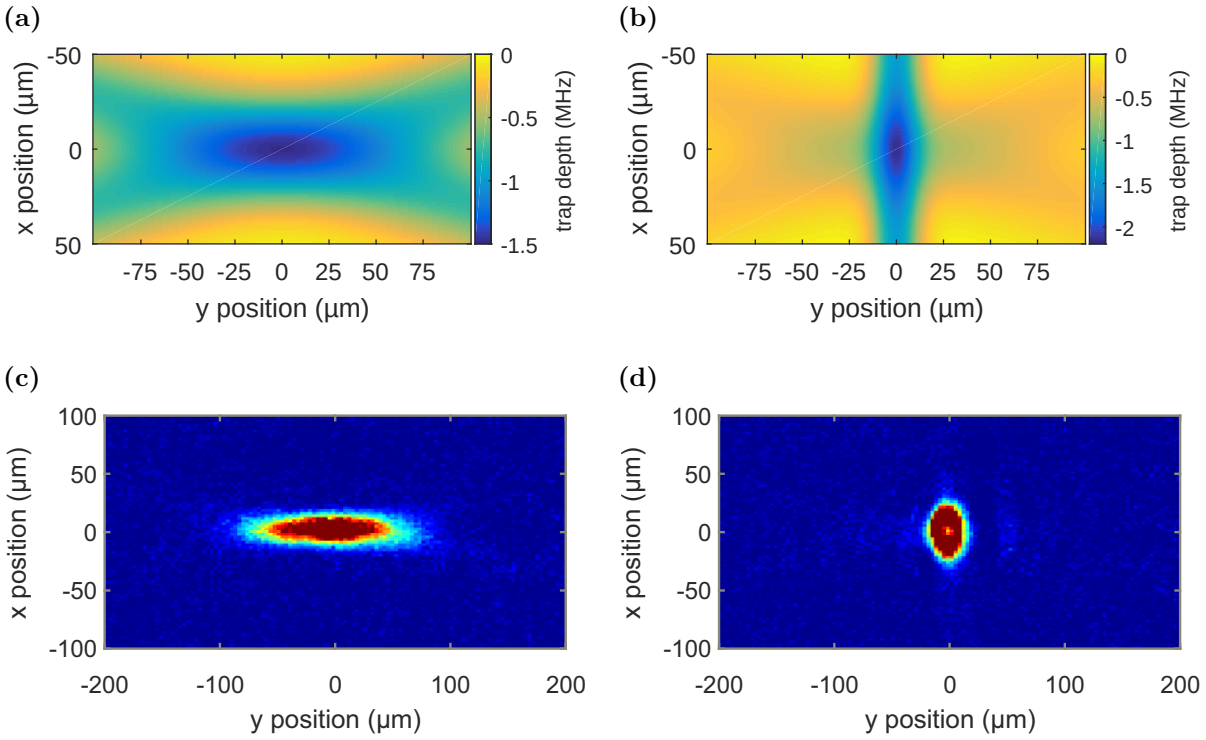

Figure 5.6: **Trapping atom in an optical dipole trap** (**a**) Calculated trapping potential of the crossed optical dipole trap at 1070 nm operated at a power of 0.6 W. (**b**) Calculated trapping potential of the crossed optical dipole trap superimposed with the dimple beam at 855 nm. The length of the atomic medium along y can be dramatically reduced by the dimple beam to fit only a single Rydberg atom in. (**c**)+(**d**) Atomic densities measured by absorption imaging of atoms trapped in the potentials shown in (a)+(b). As expected from the calculated potentials, the crossed ODT leads to a elongated cigar shaped atomic sample, while the additional dimple results in a reduced length in y-direction.

5.2.2 *Raman sideband cooling*

Crucial for low dephasing rates and long experiment time in a single MOT cycle is a low temperature of the atomic ensemble. As an example, a lower temperature yields a narrower Rydberg excitation linewidth as the effect of Doppler broadening scales with the square root of the temperature [64]. Hence, the mediated Rydberg interactions become stronger due to the dependence of the blockade radius on the excitation linewidth. Second, the ballistic expansion of the atomic ensemble when the trapping potential is switched off occurs on a longer timescale when the temperature is reduced. This allows to recapture the atoms after a experiment time of about 20 µs in the optical trap. Especially for the measurements of photon correlation functions requiring a large amount of statistics, such a recapture procedure allows to decrease the required experiment time tremendously.

Using the optical dipole trap the atoms can in principle be efficiently cooled by forced evaporation [114, 115]. In doing so, the depth of the trapping potential is decreased gradually over time, such that the hottest atoms of the Boltzmann distribution can escape the trap. As a consequence, both the mean temperature and the total atom number of the ensemble is reduced. In order to achieve strong nonlinearities, besides low temperatures also a high OD is important, thus a cooling method which is not based on loss of atoms is desired. One among many different options is Raman sideband cooling (RSC), implemented in the experiment during the Bachelor thesis of Christoph Braun [116]

The principle of Raman sideband cooling originates from cooling techniques developed for cold ions trapped in electric harmonic oscillator potentials [117] like e.g. a Paul trap, but can be applied to cold atoms as well [118]. While there are even for ^{87}Rb different approaches, Fig. 5.7 (a) represents the scheme implemented for the experiments within this thesis. After loading of the ODT, atoms are first transferred to the $|5S_{1/2}, F = 1\rangle$ state. Subsequently a deep optical lattice is ramped up, where each of the lattice sites can be modeled by a harmonic oscillator potential. When the lattice is steep enough, the equally spaced levels n of the harmonic oscillator potential are well separated in energy. These levels represent the quantized kinetic energy of the atoms. Since the atoms have a finite temperature at the beginning of the cooling process, the harmonic oscillator levels are distributed accordingly. The lowest temperature of the sample is reached when all atoms are in the ground state of the harmonic oscillator potential. Goal of the cooling mechanism is thus to gather all atoms in this state.

By applying a magnetic field the degeneracy of the three spin state $m_F = -1, 0, 1$ of the $F = 1$ hyperfine state can be lifted due to the Zeeman effect. To start the cooling process the magnetic field is chosen such that the relative Zeeman shift of the different spin states equals the energy spacing ΔE_n of the harmonic oscillator levels of the lattice. As a consequence different oscillator levels assigned to different spin states are tuned to degeneracy as illustrated in the sketch. As the sample is not spin polarized yet, atoms are distributed over all different possible states. Therefore each atom can be described by its spin state m_F and the motional quantum number n, in the following expressed by $|m_F, n\rangle$. Two-Photon Raman transitions driven by the lattice light result in a transfer of atoms between the degenerate harmonic oscillator levels. For example an atom starting in $|1, 8\rangle$ can be transferred to $|-1, 6\rangle$, i.e. the atom is loosing two quanta of kinetic energy and changes its spin state by $\Delta m_F = 2$. To achieve further cooling the atom has to be transferred back to $m_F = 1$ to start over the same process. This is not possible with Raman transitions as it would cost the same amount of energy and thus not result in a cooling. Instead the atom is pumped to $|5P_{3/2}, F = 0, mF = 0\rangle$ by an additional σ^+ polarized "polarizer" which is on resonance with the $|5S_{1/2}, F = 1\rangle \leftrightarrow |5P_{3/2}, F = 0\rangle$ transition. From the excited state the atom can decay back to $|F = 1, m_F = 1\rangle$ or $|F = 1, m_F = 0\rangle$. Subsequently, Raman transitions changing the spin state to $m_F = -1$ can further reduce the kinetic energy. Yet, a net cooling can only occur if the optical pumping process with the polarizer does not result in a strong change of the kinetic quantum number n. This condition is met in the Lamb-Dicke regime, which is entered when

the recoil energy $\mathrm{E_r} = \hbar^2 k^2/(2m)$ an atom picks up during the absorption of a photon is smaller than the spacing ΔE_n of the harmonic oscillator levels [119]. Then transitions changing the motional quantum number n by more than one are strongly suppressed. Due to the choice of σ^+ polarization of the polarizer, $|1,1\rangle$ is a dark state from which no optical pumping occurs. Additionally, for this state no Raman coupling occurs as no other degenerate level can be populated. As a consequence, all atoms finally end up in this state. The final temperature of the sample is reached at an equilibrium value determined by the heating rate introduced by scattering of lattice light and the cooling rate.

The realization of Raman sideband cooling in the experiment is illustrated in Fig. 5.7 (b). The optical lattice is formed by three laser beams, one in vertical direction and two in horizontal direction. Each of the beams has a beam waist of $w_0 = 1.1$ mm. Due to spatial constraints imposed by MOT and ODT the crossing angles between the horizontal beams is $\theta = 55°$. On top, one of these beams is retro-reflected to form a standing wave. The overlap region of the beams forming the lattice is aligned onto the center of the optical dipole trap to achieve efficient loading of the lattice. The polarizations of the laser beams are chosen as depicted in the sketch. Either of the propagating beams has its polarization pointing along the direction of the other one, the polarization of the standing wave encloses an angle of 55° with the x-y-plane. This choice of polarizations guarantees maximum lattice depth for a given power of 35 mW in each beam and detuning. The wavelength of the lattice is chosen to be 780.262 MHz, resulting in a detuning of ≈ 12 GHz with respect to the $|5S_{1/2}, F = 1\rangle \leftrightarrow |5P_{3/2}, F = 2\rangle$ transition. This detuning exceeds the bandwidth of the fast photodiodes and the amplifiers used for the stabilizing the laser frequency. For this reason the laser is free running which results in a drift on the order of 10 MHz per day. As this is very small compared to the overall detuning it is not influencing the depth of the optical lattice an the final temperatures obtained by the cooling. Calculation of the lattice for the given experimental parameters [116] yield a global depth of each lattice site of $U_{\mathrm{Lattice}} = 142\ \mu\mathrm{K} = 786\,\mathrm{E_r}$ and trap frequencies of $\{\omega_x, \omega_y, \omega_z\} = 2\pi \cdot \{161, 66, 57\}$ kHz. The trap frequencies determine the spacing $\Delta E_n = \hbar\omega$ of the harmonic oscillator levels, resulting in $\{\Delta E_{n,x}, \Delta E_{n,x}, \Delta E_{n,x}\} = \{7.7, 3.2, 2.7\}\ \mu$K. In comparison, the recoil energy of the D_2 line in ^{87}Rb at a wavelength of 780 nm is $\mathrm{E_r} = 0.18\ \mu$K. As this value is small compared to the level spacing, the lattice is operated deep in the Lamb-Dicke regime.

The polarizer for optical pumping is superimposed from top with the lattice beam pointing in z-direction and σ^+ polarized with respect to the magnetic field pointing in z-direction as well. To bring atoms ending up in $|0,1\rangle$ back in the cooling cycle the polarization contains a small fraction of π-light.

Once all beams are aligned with respect to the optical dipole trap, all available parameters have to be optimized. The most crucial parameter to play with is the direction and strength of the magnetic field, which can be applied by three Bias coils (compare A.1). First, for defined σ^+ polarization of the polarizer beam it is necessary to avoid any magnetic field in the x-y-plane. An appropriate method to find a good starting parameter is

to perform microwave spectroscopy on the hyperfine splitting of the ground state. Only if the magnetic field is canceled out well enough, the positions of transitions between different magnetic spin states in the spectrum coincide. Second, to achieve the required degeneracy of different oscillator levels the strength of the magnetic field in z-direction has to be chosen according to oscillator level spacing. Having found these starting parameters the performance of the Raman sideband cooling interval in the sequence can be optimized by changing power and detuning of the polarizer on maximum atom number and lowest temperature for a given final trap depth of the ODT.

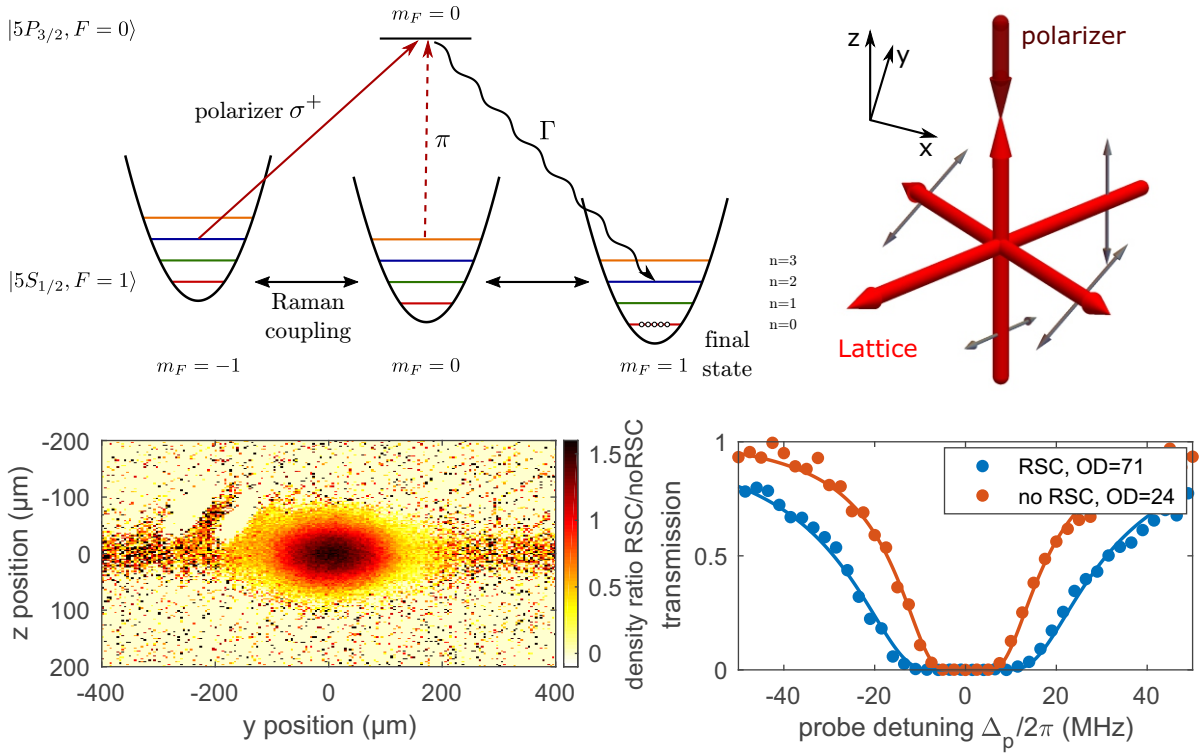

Figure 5.7: **Raman sideband cooling in Rb** (**a**) Working principle of Raman sideband cooling. Two-photon Raman transitions between degenerate motional levels n of different spin states result in a loss of kinetic energy. By optical pumping with the polarizer in the Lamb-Dicke regime atoms can be transferred back to $m_F = 1$ without changing the motional quantum number by more than 1. After several cooling cycles all atoms end up in the oscillator level denoted as final state. (**b**) Arrangement of the laser beams forming the optical lattice and the polarizer for optical pumping. Bold arrows at the end of each arrow represent the propagation direction of the laser beam, the thinner gray arrows indicate the polarization. (**c**) Ratio of the atomic density with and without RSC after a time of flight of 2 ms. (**d**) Transmission of the probe laser through the cold atomic cloud. The resonant optical density obtained by fitting eq. (4.20) to the data changes from $OD = 24$ without RSC to $OD = 71$ after RSC.

Fig. 5.7 (c) shows the ratio of the atomic density measured by absorption imaging after a time of flight of (ToF) 2 ms with and without RSC. After this ToF, utilization

of RSC in an otherwise identical sequence results in an increase of the peak density by more than a factor 1.5. Additionally, as a consequence of the lower temperature the cloud expands slower after switching of the optical dipole trap. By measuring the dimensions of the cloud in a time of flight series the final temperature of the atoms is determined to by $T_{\mathrm{RSC}} = 2.9\ \mu\mathrm{K}$. This is more than a factor of 3 lower compared to the temperature of 10.9 μK measured at same parameters without RSC.

More important for the experiment is the increase of optical density for the probe beam. Again for same starting parameters but with and without RSC, Fig. 5.7 (d) shows a transmission spectrum of the probe field with respect to the atomic resonance. Fitting eq. (4.20) to the spectra yields a change of optical density from $OD = 24$ without RSC to $OD = 71$ with RSC. This change is of huge benefit for the experiment as it reduces the delay time of polaritons in the medium and thus yields stronger optical nonlinearities.

5.3 MEASUREMENT OF RYDBERG MEDIATED NONLINEARITIES

Having introduced the general experiment setup in this section typical experiments demonstrating the giant optical nonlinearities are discussed. Out of a wide range of possible applications, the focus is put on two distinct examples. A first example is the nonlinear transmission on EIT resonance and its impact on the temporal correlation function of the transmitted light. The second example discusses the influence of photon scattering on storage and readout experiments and their possible application in quantum information science.

5.3.1 *Nonlinear EIT transmission and photon statistics*

The nonlinear transmission, strongly depending on the intensity of the applied probe field, was the first quantity investigated in Rydberg-EIT experiments [37]. Once the setup has been built, the measurement of such nonlinearities is straightforward. Fig. 5.8 (a) presents the rate of transmitted probe photons R_{out} as a function of the input rate R_{in}. The measurement shows a clear saturation of transmitted photons already at input rates of the order $R_{\mathrm{in}} = 1\ \mu\mathrm{s}^{-1}$. In fact, maximising the nonlinearity by changing the position of the atomic cloud allowed to align the cloud to the focus spot of the probe beam.

The strong nonlinearity is also reflected in the measurement of the intensity correlation function $g_2(\tau)$ shown in Fig. 5.8 (b). As the waist of the probe beam at the position of the atomic cloud is more narrow than the Rydberg blockade, $g_2(\tau)$ reveals strong antibunching at $\tau = 0$, i.e. the generation of non-classical light.

5.3.2 *Transistor measurement with readout*

The availability of two independent probe and control lasers in the optical setup allows for measurements of all optical switches [120] and transistors [47, 54, 48]. The idea is, in analogy to an electric transistor, to switch a rather large source current (stream of photons) by a very tiny gate current. In the absolute limit of an all optical transistor, a

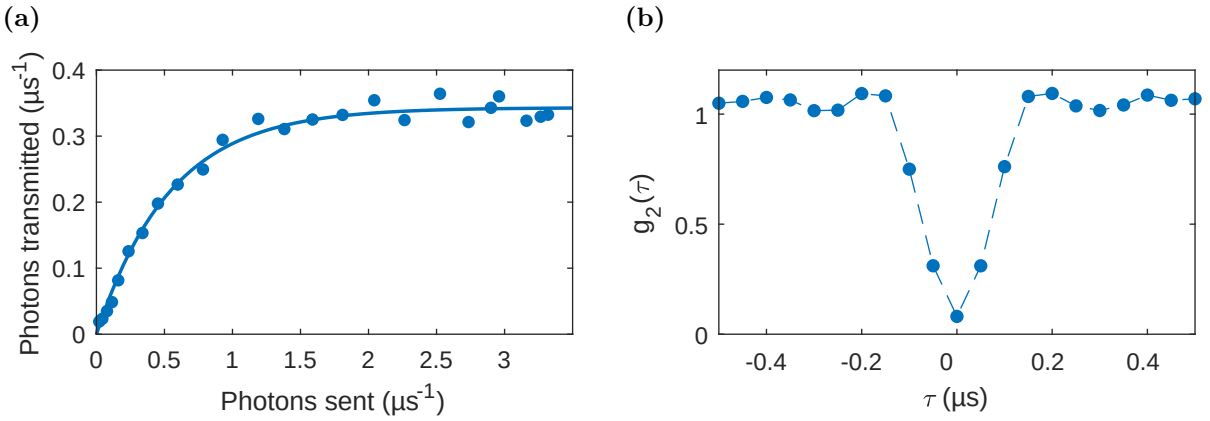

Figure 5.8: **Photon nonlinearities mediated by Rydberg interactions** (**a**) Rate of transmitted photons R_{out} as a function of input photon rate R_{in} measured on EIT resonance with $\Delta_p = \Delta_c = 0$. (**b**) Measured intensity correlation function $g_2(\tau)$. As a consequence of the Rydberg interaction two polaritons cannot come too close to each other inside the medium. This affects the photon statistics when polaritons are converted back into photons outside the medium and results in antibunching.

single gate photon has the ability to modulate a large number of source photons. With this setup such a single photon transistor was realized with a record optical gain $\mathcal{G}$ of up to 200, where the optical gain is a measure how many source photons can be attenuated by a single gate photon. The results of these measurement can be found in the thesis of Hannes Gorniaczyk [97].

The data discussed in this section is relevant for the implementation of all-optical quantum gates as e.g. the approach for a phase gate described in sec. (4.5.2). For such an application, the gate photon, which induces the gate operation on a source (or target) photon, has to be retrieved again after the gate operation. This demand can be realized utilizing the stopped light technique of EIT to first store a photon inside the atomic cloud and subsequently retrieve the photon again [121]. According to eq. (4.26) the group velocity of a light pulse inside the medium can be controlled by Ω_c. As a consequence, adiabatically decreasing Ω_c when a probe pulse is inside the atomic cloud increases the atomic character of the polariton such that a photon is finally stored as a Rydberg excitation when $\Omega_c = 0$. Because of the indistinguishability of the atoms in the cloud, this Rydberg excitation is shared between all atoms, forming a coherent collective spin-wave[10]. When turning Ω_c on again after a storage time τ_{Storage}, the coherence of the spin-wave results in a enhanced emission of the probe photon in forward direction such that the photon can be eventually detected [121]. For most efficient readout it is important, that the coherence of the spin-wave does not change in time. However, already

[10] Apart from the terminology, the treatment of such a spin-wave is in total analogy to the superatom introduced in sec. (7.1.1). In this section also dephasing mechanisms of the superatom are discussed, which naturally reduce the readout efficiency of a stored photon.

movement of the atoms results in spatially varying phases of the spin-wave, as extensively discussed in sec. (7.4). This sets a limit to the time-scale after which a photon can be retrieved from the medium.

The blue curve in Fig. 5.9 (a) shows an example time trace of such a storage and retrieval experiment. At $t = 0$, a photon pulse with a mean photon number of $\overline{N}_{\text{gate}} = 0.65$ is stored inside the atomic cloud (in the $|68S_{1/2}\rangle$ state) by slowly switching off Ω_c. As the optical depth of $OD = 16$ does not allow fit the total pulse into the medium, photons are already leaving the medium before Ω_c is switched off, resulting in the detection of photons at $t = 0$. At a time $t = 3.5$ µs the control field Ω_c is turned on again, allowing to retrieve $\approx 10\%$ of the initially stored photons. Experiments performed at different atomic densities and temperatures revealed the dependence of the storage efficiency on these parameters [120].

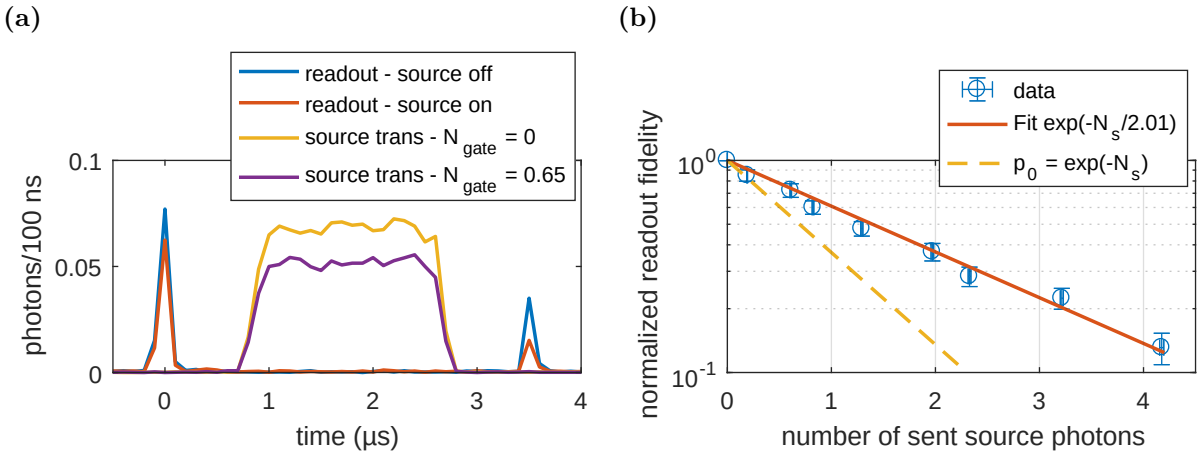

Figure 5.9: **Transistor Operation with readout** (**a**) EIT based storage allows to covert gate photons into Rydberg spin-waves inside the atomic cloud and efficient retrieval in forward direction after a certain storage time. When no source field is applied, the gate photons can be red out after $t = 3.5$ µs with an efficiency of $\approx 10\%$. At a mean input number of $\overline{N}_{\text{gate}}$ the transmission of source photons gets attenuated by $\approx 25\%$. At the same time, scattering of source photons lowers the readout efficiency of gate photons. (**b**) The readout efficiency of gate photons decreases exponentially with the number of scattered source photons. At a value of $\overline{N}_{\text{s}} = 2.01$ incident source photons, the readout efficiency drops to $1/e$.

Having a gate operation in mind, in between storage and retrieval of the gate photon, a source photon has to be transmitted through the medium and e.g. its transmission monitored. This is facilitated by the second pair of probe and control lasers in the experiment. It allows to apply a second EIT scheme addressing a different Rydberg state, therefore crosstalk of the control fields is avoided (this would lead to undesired readout of the gate photon). To achieve yet strong interactions between the different

Rydberg excitations, in this specific experiment the source EIT utilizes the Rydberg state $|66S_{1/2}\rangle$ which is close to a Förster resonance with $|68S_{1/2}\rangle$ [54, 48]. Fig. 5.9 (a) shows the transmission of the source field both with storing a gate photon before (purple) and without (yellow trace). As a consequence of the strong photon-photon interactions, the $\overline{N}_{\mathrm{gate}} = 0.65$ stored gate photons result in a reduction of the source transmission by $\approx 25\%$.

At the same time, when source photons are transmitted through the cloud, the readout efficiency drops (red line). A more quantitative analysis of this observation is shown in Fig. 5.9 (b), where the dependence of the readout efficiency on the number of source photon is measured. The readout efficiency decreases exponentially with the number of incident source photons, with a fitted $1/e$ value of $\overline{N}_{\mathrm{s}} = 2.01$. In comparison, the dashed yellow line indicates the probability that a source photon pulse with an average value of $\overline{N}_{\mathrm{s}}$ contains no photon, stemming from the Poissonian statistics of the light. The fact that this line is lower than the measured data suggests that a single incident gate photon does not completely destroy the readout efficiency.

The vanishing readout efficiency hints at a dephasing of the spin-wave when source photons are scattered. An evident explanation of the effect is the localization of the spin-wave (which is initially distributed over all atoms) onto the size of the Rydberg blockade, as source photons can only be scattered from this region. This results in a decreased overlap of initial and final spin-wave and thus reduction of the readout efficiency [122]. As the observed effect imposes a limit on overall fidelities for Rydberg based all-optical quantum gates, it is investigated in current theoretical work, predicting parameter ranges for a better operation [123, 124]

6 Dipolar Dephasing of Rydberg *D*-state polaritons

Changing the angular momentum of the Rydberg state coupled in the EIT scheme from $L = 0$ (S-state) to $L = 2$ (D-state) allows discovering new interesting phenomena. From the technical point of view, employing the D-states allows increasing the Rabi frequencies of the coupling light due to the larger dipole-matrix elements for transitions to the $|5P_{3/2}\rangle$ level. From the interaction point of view, there is another advantage of D- over S-states. Due to the nature of the quantum defects and the different electric polarizabilities of different angular momentum sates, *single color* Förster resonances can be addressed in small electric fields [33, 125, 55]. This enables to tune the character of the Rydberg interaction from van-der-Waals type to resonant dipole-dipole interaction or even turn the interaction completely off. Especially studying the effect of dipole-dipole interaction on the polariton propagation inside an atomic medium is of high interest.

Furthermore, the anisotropic character of the Rydberg interaction experienced by Rydberg D-states in combination with *EIT* adds another approach to investigating systems with such interactions. With the goal to under strongly correlated quantum systems such as high temperature superconductivity or the crystallisation of electrons in solid state matter, long-range and spatially anisotropic dipole-dipole interactions (DDI) are studied in a large number of approaches [126]. For example, magnetic dipole-dipole interaction is used to couple individual nuclear spins to nitrogen-vacancy centers in diamond [127, 128]. More recently, magnetic DDI in dipolar ultra cold atomic gases [129, 130] enabled the investigation stable self-bound droplets of a magnetic quantum liquid, a new state of matter [131, 132]. On the other hand, electric DDI is investigated in systems of homo- and heteronuclear polar molecules [133] or Rydberg atoms [134, 135]. There are proposals how phenomena like quantum magnetism [136, 137, 57] or topological phases [138] might be investigated in such kind of systems.

The rapid progress in the field of cold atomic physics over the last years provides nowadays full control on the level of single atoms. Due to the availability of such techniques, only very recently the angular DDI between single Rydberg atoms has been fully mapped [88].

In this chapter, results obtained during the scope of this thesis and published in [49] are discussed. Here, for the first time, the effects of the anisotropic Rydberg interaction of Rydberg D-states on slowly propagating polaritons in a cold atomic medium is experimentally studied. These experiments reveal an interaction-induced dephasing of Rydberg polaritons already at very low input photon rates into the medium. By developing a model combining the numerical propagation of the two-photon wave function

through the system with calculated Rydberg-Rydberg potentials, the experimentally observed time-dependent decay of transmission of the probe field is simulated.

In detail this chapter is structured as follows: The first section of this chapter presents the results obtained in the experiment when applying the *EIT* scheme to *D*-states. In a series of measurements, the dependence of the loss in transmission on photon rate, Rabi frequency and main principal quantum number is investigated. To gain a understanding of the observed effect, the second section presents calculated Rydberg-Rydberg potentials based on the discussions in chapter 3 and highlights the differences of *D*- and *S*-state potentials and their relevance for the experiments. Subsequently, from the time evolution of the eigenstates in the presence of interaction, an effective dephasing model is derived. The core idea of this model is that strong dephasing in the presence of interaction, occurring already outside the blockade region, causes decoupling of polaritons from the control light. These decoupled polaritons lead to stationary Rydberg excitations which block the transmission of further polaritons. Finally, results obtained by numerical propagation of the two-polariton wave function through a $3D$ medium including the dephasing model are presented.

6.1 EXPERIMENTAL RESULTS

The experiments described in this section were carried out in the first generation setup described in chapter 5, without the electric field control and the ability to detect Rydberg atoms via field ionization. For all experiments presented here, the experiment scheme presented in Fig. (6.1) was applied.

For fast data acquisition the ODT is modulated in these experiments such that several measurements in a single MOT cycle can be taken. For all experiments presented within this chapter, the ODT is switched off 30 times after each MOT loading phase for 32 µs during which data is taken. Subsequently, the atoms are recaptured during 230 µs. After recording the photons transmitted through the atomic ensemble by this method (this gives the signal counts), the ODT is turned off for 10 ms. During this switch off time the atoms can escape from the trapping region allowing to measure the number of photons sent into the chamber as a reference.

To efficiently recapture the atoms in the ODT after each measurement, the atoms loaded from the MOT are evaporatively cooled to a temperature of 30 µK. At this temperature, the resulting cloud size is $\sigma_z = 80$ µm in the longitudinal direction and $\sigma_r = 25$ µm in the transversal direction with respect to the probe beam, resulting in a constant OD of 45 over the full range of the 30 pulses. Due to the dependence of the delay time τ_{delay} (eq. (4.27)) on OD, this stability is very important to investigate propagation effects.

By choosing the polarization of the control field Ω_c to be σ^+-polarized with respect to the quantization axis, only the $m_J = 5/2$ component of a $nD_{5/2}$ Rydberg state is addressed, resulting in a isolated three-level system consisting of the states $|g\rangle = |5S_{1/2}, F = 2, m_F = 2\rangle$, $|e\rangle = |5P_{3/2}, F = 3, m_F = 3\rangle$ and $|r\rangle = |nD_{5/2}, m_J = 5/2\rangle$.

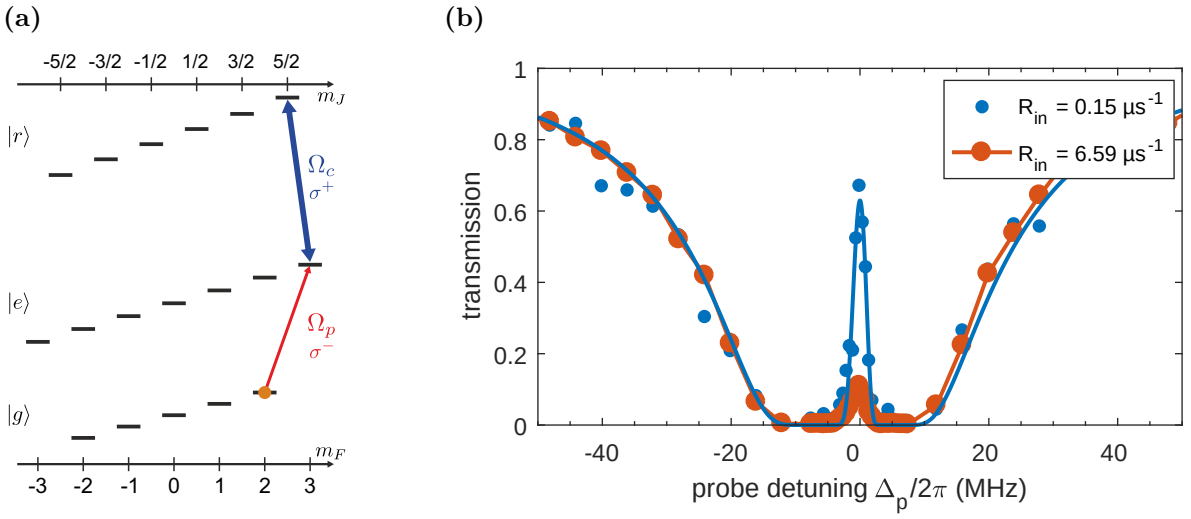

Figure 6.1: **Rydberg EIT with *D*-states** (**a**) Level scheme applied for the measurements. To measure the EIT transmission, both laser fields Ω_p and Ω_c drive the corresponding transitions on resonance ($\Delta_p = \Delta_c = 0$). To achieve a clean three-level system, the polarization of Ω_c is chosen to be σ^+, coupling the intermediate state $|e\rangle$ to a $|nD_{5/2}, m_j = 5/2\rangle$ state. (**b**) EIT spectrum involving the state $|r\rangle = |80D_{5/2}\rangle$.

Fig. (6.1) (b) shows a transmission spectrum in which the frequency of the probe field is scanned across the resonance, while the frequency of the control field with $\Omega_c = 2\pi \cdot 10.5$ MHz is kept constant and couples the intermediate state resonantly with the $|80D_{5/2}\rangle$ state. At a low input photon rate of $R_{in} = 0.15$ µs^{-1} this results in a narrow EIT peak with a high transmission of 70% around two-photon resonance. From a fit to the spectrum a dephasing rate $\gamma_r = 2\pi \cdot 200$ kHz can be determined, resulting from thermal movement of the atoms at the finite temperature and stray electric fields over the atomic cloud. This is a typical value also measured with *S*- instead of *D*-states.

Increasing the input photon rate to $R_{in} = 6.59$ µs^{-1} results in a decrease of the transmission of the EIT feature, while neither the position of the line shifts nor its width increases. The effect is therefore purely caused by the self-blockade of propagating Rydberg polaritons, already observed before [37, 38, 39] for *S*-states. Both the narrow spectrum and the strong nonlinear transmission through the medium do not reveal any difference compared to the same experiment carried out with a high lying Rydberg *S*-state. A qualitatively new effect, when applying the *EIT* scheme to *D*-states, occurs when the temporal dependence of the transmission is investigated, as shown in Fig. 6.2 for $|88D_{5/2}\rangle$ (a) and $|90S_{1/2}\rangle$ (b).

Focusing on the measurements for the state $|88D_{5/2}\rangle$ first, the transmission remains constant over the full time range of the pulses when working at very low input photon rate $R_{in} = 0.15$ µs^{-1}, where the chance to find two polaritons inside the medium is very small. The finite transmission at this rate is only determined by the control Rabi

frequency Ω_c, which in this measurement is $\Omega_c = 8.3$ MHz, and the decoherence rate γ_r.

If the rate of input photons is increased to $R_{in} = 1.74\ \mu s^{-1}$, besides the drop in initial transmission resulting from the self-blockade of polaritons, there is already a visible decay of transmission over the time of the pulse. The decay of transmission gets even faster, when R_{in} is increased further (blue line, $R_{in} = 5.84\ \mu s^{-1}$).

In contrast, Fig. 6.2 (b) shows the experimental results when the EIT scheme is applied to the Rydberg state $|r\rangle = |90S_{1/2}\rangle$. For better comparison, the control Rabi frequency $\Omega_c = 2\pi \cdot 10.2$ MHz and the input photon rates R_{in} are chosen similar to the values for the experiments presented for the measurement with $|88D_{5/2}\rangle$. For input rates of $R_{in} = 0.43\ \mu s^{-1}$ and $R_{in} = 2.1\ \mu s^{-1}$ the data reveals no change of transmission over the full range of the pulse. Only for the largest input rate of $R_{in} = 5.4\ \mu s^{-1}$ a small drop in transmission occurs in this dataset. However, the observed change in transmission is much smaller than the one measured with $|88D_{5/2}\rangle$. At the same time, the initial transmission for similar photon rates is almost identical for the measurements with S- and D-states.

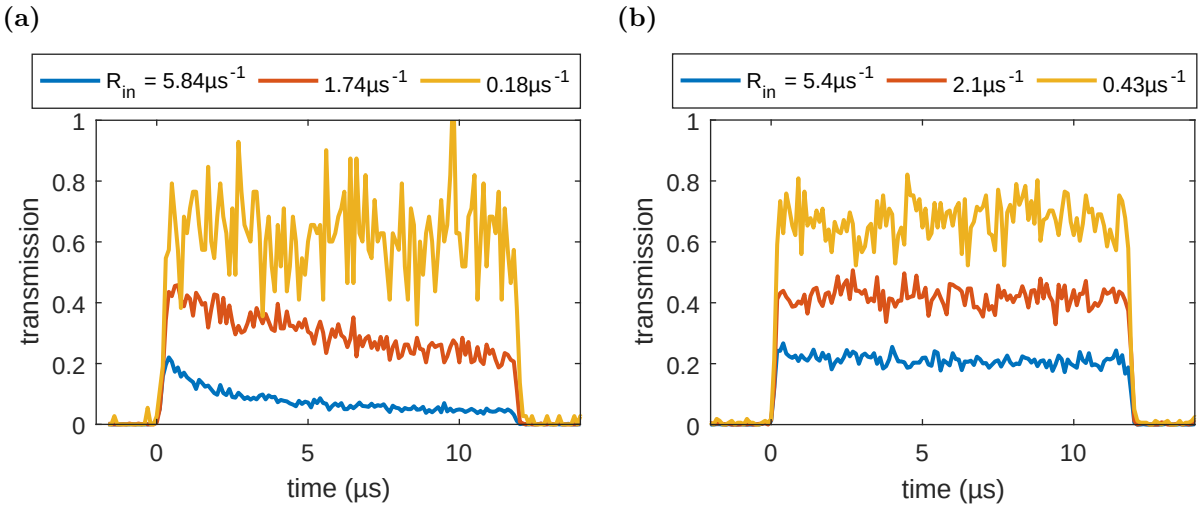

Figure 6.2: **Time dependent transmission on EIT resonance** (**a**) Measured time traces of probe photons transmitted through the medium on EIT resonance. For this measurement, the control field couples resonantly to the Rydberg state $|r\rangle = |88D_{5/2}, m_J = 5/2\rangle$ with a Rabi frequency $\Omega_c = 2\pi \cdot 8.3$ MHz. When the input photon rate R_{in} is increased to values at which two polaritons are in the medium at the same time, the transmission decreases over time. (**b**) Measurement as in (a) but applying the EIT scheme to the Rydberg state $|r\rangle = |90S_{1/2}, m_J = 1/2\rangle$. For this Rydberg state only a weak change in transmission is observable at the highest input photon rate.

A feasible explanation is that interaction-induced coupling of degenerate Zeeman sublevels results in a conversion of polaritons into stationary Rydberg excitations inside the

cloud, see sec. (6.3.2). Due to the Rydberg interactions, these impurities shift the Rydberg levels of surrounding atoms and thus prevent further polaritons from propagating through the cloud [120, 47, 54].

To find scaling laws of the observed effect with input photon rate R_{in}, Rabi frequency Ω_c and principal quantum number n it is reasonable to express the transmission properties by the means of an effective optical density OD_{eff} on EIT resonance ($\Delta_p = \Delta_c = 0$). According to the definition of the optical density, OD_{eff} is calculated from the transmission T_{EIT} of the time traces by

$$OD_{eff} = -\log_{10}(T_{EIT}). \tag{6.1}$$

In this form the different effects influencing the transmission show up in the sum

$$OD_{eff} = OD_{dec} + OD_{nl}(R_{in}) + OD_{dph}(R_{in}, t) \tag{6.2}$$

and can be treated in a more thorough way. The single terms OD_{dec}, OD_{nl} and OD_{dph} represent the contributions stemming from decoherence caused by finite γ_r, self-blockade of propagating polaritons and finally the newly observed effect due to interaction induced dephasing of degenerate Zeeman spin states. In the following the discussions are restricted to the latter, as the two other effects have already been treated precisely before [37, 38, 39].

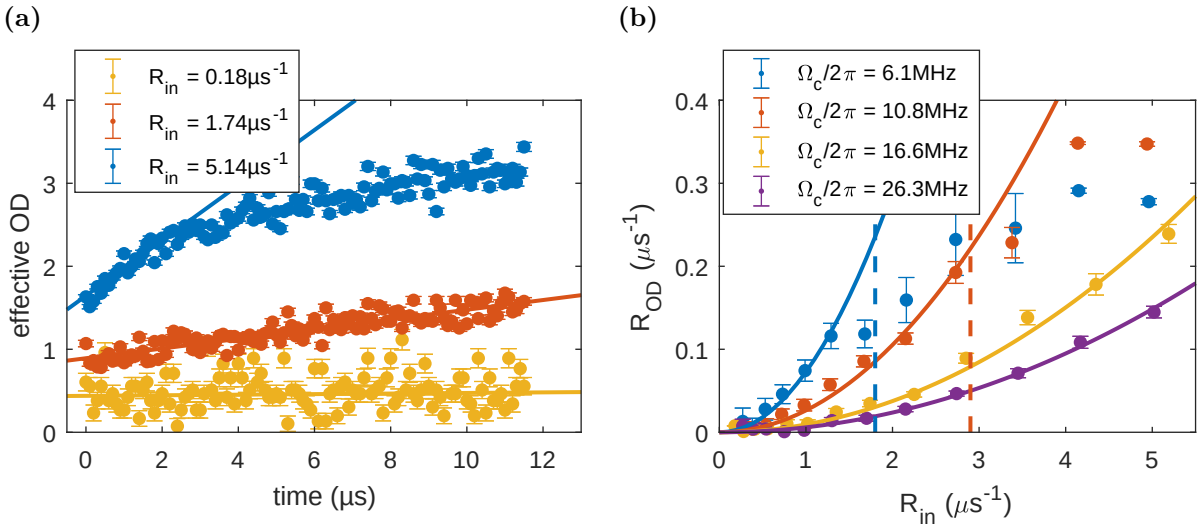

Figure 6.3: **Creation rates of optical density** (**a**) From the transmission of the pulses on EIT resonance a effective optical density OD_{EIT} is calculated. Except for the highest photon rates which show saturation effects the pollution leads to a linear increase in OD over time. (**b**) Dependence of creation rate R_{OD} of additional OD on the input photon rate for different Rabi frequencies Ω_c. The rates R_{OD} are extracted from the time traces shown in (a) by fitting eq. (6.3) in the linear regime.

In Fig. 6.3 (a) the transmission of the previously shown time traces is transformed to OD_{eff} according to eq. (6.1). Except for the highest input photon rates R_{in}, for which the slope of the increase in OD changes after a certain time, the additional term $OD_{dph}(R_{in}, t)$ accumulates linearly with time. Neglecting these saturation effects for the highest values of R_{in} the increase in OD due to dephasing can be approximated to be linear in time and written as

$$OD_{dph} = R_{OD} \cdot t, \tag{6.3}$$

where R_{OD} is introduced as a creation rate of additional optical density by decoupled impurities. For all available data sets, these creation rates are determined by a fit to the experimental data.

The dependence of R_{OD} on R_{in} for a set of Rabi frequencies Ω_c measured by applying the EIT scheme to $|r\rangle = |88D_{5/2}, m_J = 5/2\rangle$ is presented in Fig. 6.3 (b). The data sets with $\Omega_c = 2\pi \cdot 16.6$ MHz and $\Omega_c = 2\pi \cdot 26.3$ MHz show a clear quadratic scaling of R_{OD} with R_{in} over the full experimentally studied input range. This quadratic dependence suggests that the observed dephasing is a two-body effect, supporting the assumption that the observed effect is related to the Rydberg interaction. In particular, this experimental observation justifies the treatment later on in sec. 6.3, where finally the dephasing is related to the probability

$$|\psi_{dd}|^2 = \frac{R_{in}^2}{v_g^2}. \tag{6.4}$$

to find two polaritons in the Rydberg state at the same time at distances larger than the blockade radius r_b.

For the smaller Rabi frequencies $\Omega_c = 2\pi \cdot 6.1$ MHz and $\Omega_c = 2\pi \cdot 10.8$ MHz deviations from the quadratic dependence occur for R_{in} exceeding 1.5 μs^{-1} and 2.7 μs^{-1}, respectively. The vertical dashed lines indicate the rates at which the mean number of polaritons inside the medium exceeds 2, calculated from the delay time of a pulse inside the medium given by $\tau_{\text{delay}} = \frac{OD \cdot \Gamma_e}{\Omega_c^2}$ and taking into account the finite initial EIT transmission at time $t = 0$. This change from the quadratic behaviour might be influenced by three-body interaction of Rydberg polaritons [44], yet there is no further indication and the treatment of three-body effects is challenging.

On account of this dependence it is sensible to introduce a rate constant $\mathcal{C}(\Omega_c)$ which relates R_{OD} to R_{in} in the quadratic regime via

$$R_{OD} = \mathcal{C}(\Omega_c) \cdot R_{in}^2. \tag{6.5}$$

For all available datasets, these rate constants are determined by a fitting eq. (6.5) to the observed creation rates of additional OD (R_{OD}). The resulting rate constants are plotted versus Rabi frequency Ω_c for different measurements with main principal quantum numbers of $n = 80$, $n = 88$, and $n = 100$ in Fig. 6.4. The presented errorbars are calculated from the accuracy of the involved fitting by error propagation. It is striking,

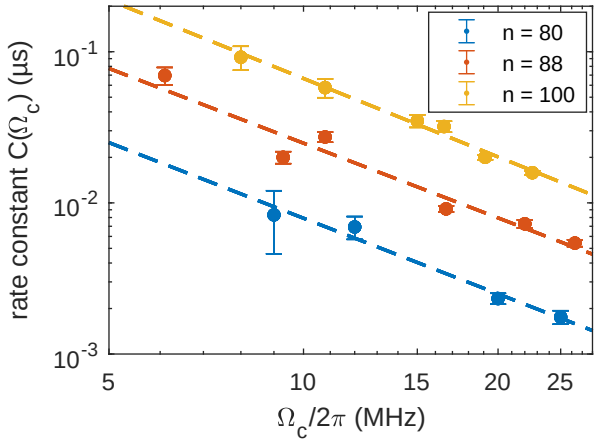

Figure 6.4: **Scaling of rate constants with Rabi frequency Ω_c and principal quantum number n** The rate constants $\mathcal{C}(\Omega)$ are determined by fitting eq. (6.5) to the extracted creation rates of additional optical density R_{OD}. For the measurements with different principal quantum numbers, the rate constants $\mathcal{C}(\Omega)$ show a power-law dependence with the exponent $k = 1.67(4)$.

that the measurements for the different principal quantum numbers obey the same power law dependence on the control Rabi frequency Ω_c. A fit of the form

$$\mathcal{C}(\Omega) = a \cdot \Omega_c^{-k} \tag{6.6}$$

yields $k = 1.67(4)$ for all different principal quantum numbers presented here. On the other hand, the pre-factor a scales strongly with main principal quantum number n indicating significantly larger dephasing for larger n.

6.2 RYDBERG-RYDBERG POTENTIALS

The reason for the scaling of the measured effects is not explainable with the well-known scaling laws of Rydberg interaction (chapter 3). As mentioned already before, one possible explanation is the interaction induced dephasing of Rydberg polaritons caused by the state mixing of Zeeman sublevels, leading to stationary Rydberg impurities inside the cloud. In contrast to S-states, this effect is much stronger for D-states due to the larger number of degenerate levels.

The consequences of such degeneracy is discussed in great detail for perturbative calculations by T. Walker and M. Saffman in [80]. In this article, the authors show that coupling of different angular momentum states leads to state mixing of the degenerate Zeeman levels resulting in anisotropic Rydberg interactions for any angular momentum states except for S-states.

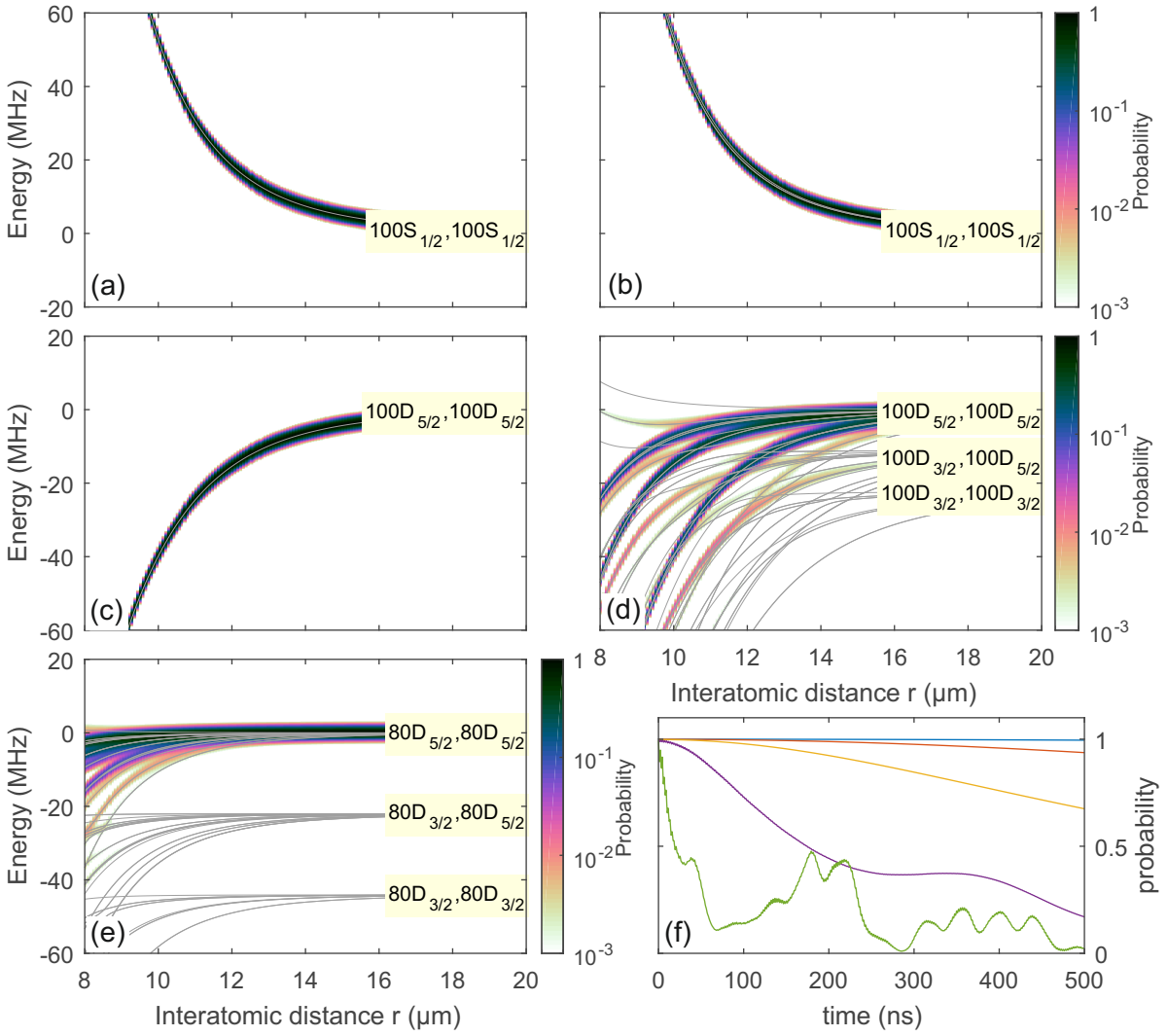

Figure 6.5: **Calculated Rydberg pair state potentials** (**a**)+(**b**) show Rydberg pair potentials of $|100S_{1/2}, 100S_{1/2}\rangle$ calculated for angles of $\vartheta = 0°$ (a) and $\vartheta = 40°$ (b) inclosed between interatomic axis and the quantization axis defined by the laser fields. Potentials for the same angles ϑ for the pairstate $|100D_{5/2}, 100D_{5/2}\rangle$ are shown in (**c**)-(**d**). The color shading on the gray potential lines represents the projection of the $|m_{J1,J2} = 1/2, 1/2\rangle$ ($|m_{J1,J2} = 5/2, 5/2\rangle$) in the uncoupled basis onto the new eigenstates in the presence of interaction according to eq. (6.10). In comparison to S-states, the state mixing of degenerate Zeeman spin states results in several coupled lines for D-states interacting under an finite angle ϑ. (**e**) Calculated potential for $|80D_{5/2}, 80D_{5/2}\rangle$ at an angle $\vartheta = 40°$. The time evolution of the new eigenstates in the presence of interaction results in the time evolution of the overlap with the unperturbed state according to eq. (6.13), shown in (**f**). The selected distances are 20 μm (blue line), 15.5 μm (red line),13 μm (yellow line), 10.5 μm (purple line) and 8 μm (green line).

6.2.1 *Anisotropic Rydberg Blockade*

For qualitative analysis, Fig. 6.5 shows full numerical calculations of the angular dependent Rydberg-Rydberg potentials according to chapter 3. Following the discussion there, the angle ϑ is drawn by the interatomic axis and the quantization axis pointing along the direction of light propagation. Technically, to save computation time, the interaction Hamiltonian H_{int} is diagonalized in the interatomic coordinate system where the total magnetic moment $M = m_{J1} + m_{J2}$ is conserved. Subsequently, the states are rotated by Wigner-d-matrices back into the lab coordinate frame [80].

To calculate how strong the individual potential lines are coupled by a laser field, one has to keep in mind that the interaction admixes the basis states of the uncoupled basis. To each potential line k with eigenenergy $E_k(z)$ an eigenstate $|\psi_k(z)\rangle$ is assigned. Transformation from the uncoupled eigenstates to the new ones (and back) is provided by the unitary operator $\mathcal{A}$ ($\mathcal{A}^\dagger$). The relation between new and old eigenstates $|n_j\rangle$ is then given by

$$\begin{aligned} |\psi_k\rangle &= \sum_j a_{jk}|n_j\rangle \\ |n_j\rangle &= \sum_g a^*_{jk}|\psi_g\rangle. \end{aligned} \tag{6.7}$$

It should be stressed at this point that both eigenstates $|n_j\rangle$ and $|\psi_k\rangle$ are product states consisting of two Rydberg states. As the interaction is spatially varying the coefficients a_{jk} mixing the uncoupled states strongly depend on the interatomic position. Especially at close interatomic distances the manifold is crossing the interaction is not a small perturbation anymore.

To draw conclusions from the potential landscape onto the Rydberg blockade the optical coupling strength of individual lines has to be calculated [139]. While the explanation of the Rydberg blockade in sec. (4.5) only holds when the potential shows a single line, for more complicated potentials as in Fig. 6.5 the probability to excite at doubly-excited state has to be calculated in a two-step approach. Since the coupling from ground state $|g\rangle$ to intermediate state $|e\rangle$ is not influenced by the Rydberg interaction it is sufficient to consider transitions driven by the control light. The Rabi frequency of the first excitation step from the intermediate state $|e\rangle = |5P_{3/2}, F = 3, m_F = 3\rangle$ to the addressed Rydberg state $|r\rangle$ (single-atom state) is simply given as product of the dipole matrix element and the intensity of the control field

$$\Omega_{c,1} = -\frac{e\mathcal{E}}{\hbar}\langle e|\boldsymbol{\epsilon}\boldsymbol{r}|r\rangle. \tag{6.8}$$

The newly introduced parameter $\boldsymbol{\epsilon}$ represents the polarization of the coupling field, only addressing certain magnetic spin states due to selection rules. Once the first excitation has been created, the calculated Rydberg-Rydberg potential has to be included to determine the coupling strength to the k-th potential line. Further, as the first atom is

already excited to $|r\rangle$, the excitation can only occur to any pair state with one of the atoms in this state and the other one in a state dipole coupled to the intermediate state. To take this into account, the dipole operator in the pair state basis takes the form $\boldsymbol{r'} = \boldsymbol{r} \oplus \mathbb{1} + \mathbb{1} \oplus \boldsymbol{r}$. In addition, the single excited state $|i\angle$ has to be written in the pair state basis $|i\rangle = \frac{1}{\sqrt{2}}(|e\rangle|r\rangle + |r\rangle|e\rangle)$ as well. With this preparatory work, the strength of the second excitation step can be written as Rabi frequency

$$\begin{aligned} \Omega_{c,2} &= -\frac{d\mathcal{E}}{\hbar} = -\frac{e\mathcal{E}}{\hbar}\langle i|\boldsymbol{\epsilon r'}|\psi_k\rangle \\ &= -\frac{e\mathcal{E}}{\hbar}\sum_j \langle i|\boldsymbol{\epsilon r'} a_{jk}|n_j\rangle. \end{aligned} \tag{6.9}$$

By the appearance of the sum over the uncoupled states the admixing of states due to the interaction is taken into account.

In general the coefficients a_{jk} can be complex and the sum has to be evaluated over all j. However, in the following the admixture of other states compared to the initially addressed state $|r\rangle$ is very small. Thus, to better visualize the strength of the coupling, the potentials plotted in the following show the overlap

$$p_k = |\langle r| \otimes \langle r||\psi_k\rangle|^2 \tag{6.10}$$

of the new eigenstate $|\psi_k\rangle$ with the doubly excited pair state $|r\rangle \otimes |r\rangle$ of the state $|r\rangle$ addressed by the EIT scheme.

Fig. 6.5 (a) and (b) show the calculated pair state potentials for $|100S_{1/2}, m_J = 1/2; 100S_{1/2}, m_J = 1/2\rangle$ at angles $\vartheta = 0°$ and $\vartheta = 90°$, respectively[1]. At $\vartheta = 0°$, the calculations result in a single potential line following a typical van-der-Waals behaviour with $C_6 = 5.65 \cdot 10^4$ GHzμm^6 which is in very good agreement with the value given of $C_{6,\mathrm{Singer}} = 5.61 \cdot 10^4$ GHzμm^6 calculated perturbatively without fine structure coupling in [31]. This nice van-der-Waals type of interaction changes only slightly when calculating the potential for an angle $\vartheta = 40°$. The state mixing results in a splitting into two-potential lines with $C_{6,1} = 5.65 \cdot 10^4$ GHzμm^6 and $C_{6,2} = 5.88 \cdot 10^4$ GHzμm^6. At a position of 10 μm, which for a typical *EIT* linewidth of 5 MHz is already inside the blockade region, this results in a splitting approximately 1 MHz.

In comparison, pair potentials for $|100D_{5/2}, m_J = 5/2; 100D_{5/2}, m_J = 5/2\rangle$ (with the same constraints on H_{int}) are presented for the same angles ϑ as before in Fig. 6.5 (c),(d). As for the S-state at $\vartheta = 0°$ the constraint $\Delta M = 0$ allows only a single coupled channel which results in a single potential line. A fit to the calculated potential yields $C_6(100D_{5/2}) = -4.97 \cdot 10^4$ GHzμm^6 which is differs from the value of $C_{6,\mathrm{Singer}}(100D_{5/2}) = -4.12 \cdot 10^4$ GHz(μm)^6 by about 17%. Reason for this discrepancy is mainly the neglect of the fine structure coupling in the perturbative calculation.

[1]For the calculations the constraints for H_{int} are: $\varrho = 5$, $\Delta E_{\mathrm{pair}} = 4$ GHz, $\Delta n = 5$, $\Delta L = 3$, no restrictions on ΔJ and Δm.

A totally different potential landscape occurs in the calculation for $\vartheta = 40°$. The 36 different realizations of the total magnetic moment $M = m_{J1} + m_{J2} = 1..5$ which are all coupled with different strength result in a large number of potential lines. In contrast to the S-state discussed before the splitting of the lines is much larger in this example, even leading to strong deviations from the typical C_6 potential of the different lines at interatomic distances shorter than 15 µm.

A direct consequence of several lines coupled by the excitation line is the anisotropy of the Rydberg blockade [55]. As discussed in sec. (4.5) the blockade radius is defined as the distance where the lineshift due to the interaction exceeds the linewidth of the excitation. In the presence of several coupled lines this definition has to be slightly modified. The most strict ansatz is to define r_b as the position where even the weakest coupled potential is shifted out of the excitation linewidth. A less crude definition is to permit a small fraction of the overlap inside the excitation linewidth.

6.2.2 *Time evolution*

Another consequence of the state mixing of the degenerate Zeeman spin states is its impact on the time evolution of the states. In the presence of interaction the time evolution of the new basis states is determined in the Schrödinger picture by

$$|\psi_k(t)\rangle = \exp\left(-i\frac{E_k}{\hbar}t\right)|\psi_k(t=0)\rangle. \tag{6.11}$$

Transformation according to eq. (6.7) directly yields the time evolution

$$\begin{aligned} |n_j(t)\rangle &= \sum_g a_{jg}^* |\psi_g\rangle \\ &= \sum_g \exp\left(-i\frac{E_g}{\hbar}t\right) a_{jg}^* |\psi_g(t=0)\rangle \end{aligned} \tag{6.12}$$

for an old eigenstate $|n_j\rangle$. Taking into account the overlap of potential line $|\psi_g\rangle$ defined in eq. (6.10) yields the time dependent overlap

$$\begin{aligned} p(t) &= |\langle r| \otimes \langle r| \sum_g \exp\left(-i\frac{E_g}{\hbar}t\right) a_{jg}^* |\psi_g(t=0)\rangle|^2 \\ &= |\sum_g \exp\left(-i\frac{E_g}{\hbar}t\right) \underbrace{a_{jg}^* a_{jg}}_{p_{jg}}|^2 \end{aligned} \tag{6.13}$$

with the addressed pair state $|r\rangle \otimes |r\rangle$.

This result can be interpreted as a Fourier-transformation of the probabilities p_{jg} oscillating with a individual frequency $E_g/\hbar$. For a single coupled state the time evolution yields a single global phase which is averages out when the absolute value is evaluated. However, when several states are coupled simultaneously, even small differences E_g result in a strong time evolution $p(t)$ since all probabilities p_{jg} evolve differently in time.

To visualize this result, Fig. 6.5 (f) shows the time evolution of $p(t)$ in the presence of the interaction calculated for $|80D_{5/2}, 5/2, 80D_{5/2}, 5/2\rangle$ (subfigure (e) shows the corresponding potential) at $\vartheta = 40°$. At a large distance of 20 µm, the interaction is still such weak that the energy-levels are hardly perturbed. Consequently, $p(t)$ is still constant over the calculated range of 500 ns. With decreasing interatomic distance and thus increased splitting of the potential lines, the time evolution gets faster. In principle this dynamic is completely coherent. On long enough timescales one should thus expect revivals in the time evolution. The relevant time scale for the experiment is however determined by the delay time τ_{delay} of a polariton in the medium which is on the order of a few hundred nano-seconds for which the simulations do not show total revival. The graph shown here is just one example, actually the time evolution has to be evaluated individually for each principal quantum number and angle ϑ as it strongly depends on the overlaps p_k and energies E_k. It should be pointed out here, that for a S-state such time evolutions cannot be observed for any angle as the splitting of the lines is too small.

The consequence of this time evolution is that the coupling strength of two Rydberg atoms placed at a certain distance becomes time dependent and can even vanish. This supports the interpretation of the decay in transmission proposed before and will be further evaluated in the following section.

6.3 SIMULATION OF THE EXPERIMENT

The aim of this final section is to bring together the observed effect of a time dependent transmission when working with Rydberg D-states and the time evolution caused by the strong mixing of degenerate Zeeman spin states.

6.3.1 *Relevant distances*

The conclusion of sec. (4.5) was that in order to observe strong optical nonlinearities and antibunching in the intensity correlation function of transmitted probe light a one dimensional system in the direction of light propagation is required. For this reason the beam waist of the probe beam in the experiment is chosen to be only 6.2 µm. Section (6.2) revealed however, that a time evolution of the pair state does only occur for finite angles ϑ drawn between the quantization axis and the interatomic axis. The relevant distances for the experiment are illustrated in Fig. 6.6. Inside the medium two polaritons (Rydberg atoms) are separated by a distance $d_\parallel$ in the direction of propagation. The finite width of the beam waist allows for a distribution in the x-y-plane resulting in a vertical distance $r_\perp$. This results in an angle ϑ of the interatomic axis with respect to the quantization axis and a interatomic distance given by $d = \sqrt{d_\parallel^2 + r_\perp^2}$.

To get an impression which angles ϑ and interatomic distances d play a role in the experiments their probability densities were numerically simulated for different distances $d_\parallel$ in the range of 4 µm to 30 µm, shown in Fig. 6.6 (b). In the simulation, two disks at a distance $d_\parallel$ are selected and subsequently on each disk the a position is randomly picked with a probability given by a normal distribution with a width of 6.2 µm and its

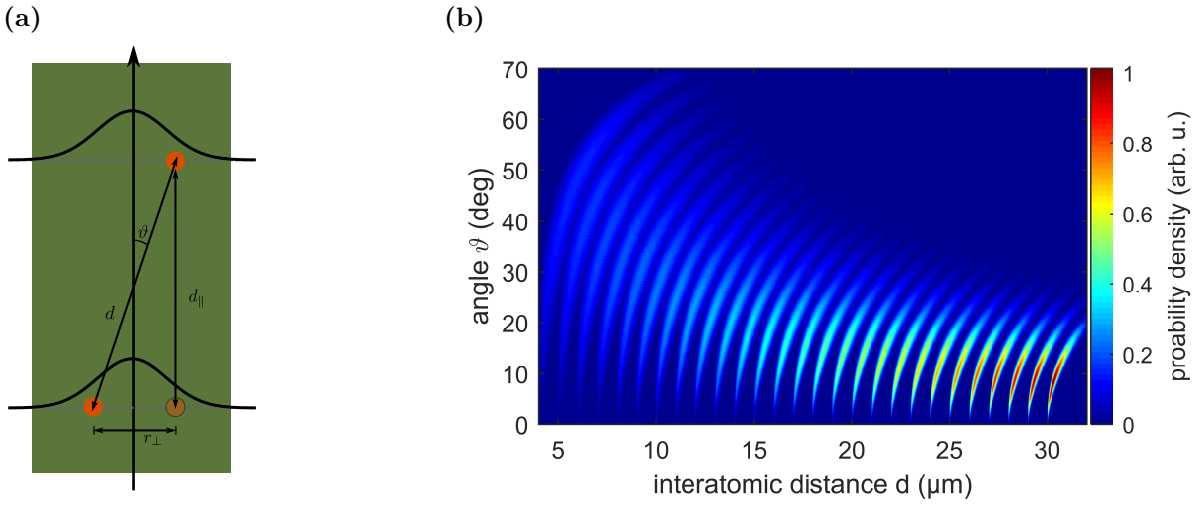

Figure 6.6: **Angle distribution of two polaritons in a medium** (**a**) Sketch of distances involved for the interaction of two polaritons inside a medium. Along the direction of propagation the two polaritons are separated by a distance $d_\parallel$. The finite width of the probe field beam with waist $w_0 = 6$ μm allows for a distribution of atoms in the $x-y$-plane resulting in a vertical distance $r_\perp$. For the interaction thus the angle ϑ and the interatomic distance $d = \sqrt{d_\parallel^2 + r_\perp^2}$ are important. (**b**) Numerical simulation of the probability distribution of angles ϑ and interatomic distances d for different distances $d_\parallel$ ranging from 4 μm to 30 μm in steps of 1 μm.

origin in the center of the disk. By this procedure a single transverse distance $r_\perp$ can be found which in turn allows calculating the angle ϑ and the interatomic distance d as the distance $d_\parallel$ of the disks is known. Repeating this procedure many time allows finding distributions for ϑ and d for a given $d_\parallel$.

The result points out what one would naively expect. For large distances d the probability to find two polaritons is restricted to relatively small angles θ and a small spread in d. On the other hand, for small d a broad probability density can be expected. The range of interest for the experiment is at $d \approx 10$ μm which is a typical value for the Rydberg blockade at sates with principal quantum number n around *100*. At such distances expected angles are almost uniformly distributed up to $\vartheta = 70°$.

6.3.2 *Effective dephasing model*

The occurrence of relatively large angles ϑ motivates the inclusion of the anisotropic Rydberg interaction and time evolution into the wave equations describing the polariton propagation through a medium [38, 41]. Most accurately, this should be done by including all degenerate Zeeman levels and the coupling between these levels into the propagation. In principle such treatment is doable up to four or five levels [140, 48], but gets very challenging with the large amount of levels one has to deal with in this case. A commonly used approach for the treatment of multi-level problems is thus to reduce the full system

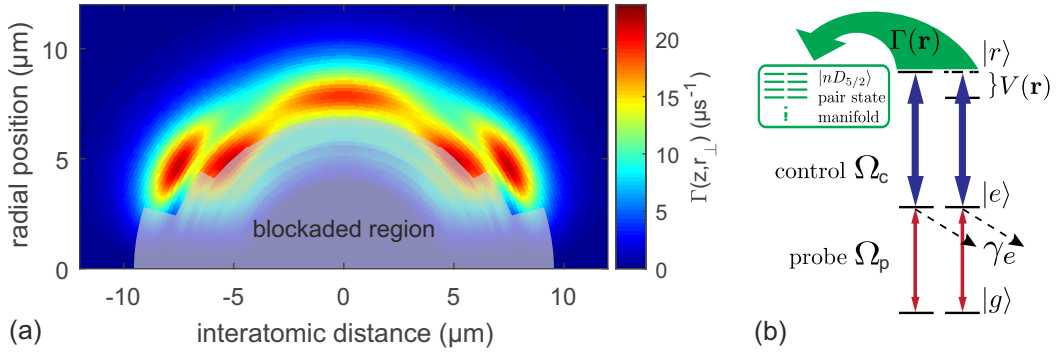

Figure 6.7: **Effective dephasing model for Rydberg polaritons** (**a**) Anisotropic blockade volume and dephasing rate $\Gamma(z, r_\perp)$ calculated for the $|80D_5/2, mJ = 5/2; 80D_5/2, mJ = 5/2\rangle$ state. (**b**) Illustration of the effective dephasing model. Inside the Rydberg-blockade the Rydberg interaction leads to a decay of the polariton amplitude due to Rydberg-Rydberg interactions leading to the self-blockade of Rydberg polaritons. Outside the blockade radius coupling between degenerate Zeeman levels leads to a time evolution which leads to a dephasing out of the state coupled by the control light.

to an effective model describing both the interaction and dephasing. The effective level structure incorporated in the calculations of this chapter is shown in Fig. 6.7 (b). From the shifts of the levels and the coupling strength an anisotropic blockade radius $r_b(\vartheta)$ is calculated, yielding an effective interaction potential $V(z, r_\perp)$. This term by itself results in the nonlinearity caused by the self-blockade of Rydberg polaritons already observed for S-states [37, 38]. On the other hand outside the blockade region, i.e. when the overall shift and the splitting of the lines is smaller then the excitation linewidth, the evolution of the coupled pair-state is described by an effective dephasing rate $\Gamma(z, r_\perp)$ (indicated by the green arrow) out of the coupled pair state into the Zeeman-manifold. As a consequence of the σ^+-polarization of the control light the levels in the Zeeman manifold are not coupled. Thus dephasing into this level leads to stationary Rydberg excitations in a different magnetic spin state. Once such an event has happened, subsequent polaritons are attenuated due to the Rydberg blockade.

To obtain $\Gamma(z, r_\perp)$ the time evolution of a stationary Rydberg pair is calculated according to sec. (6.2.2) for a given distance d and an angle ϑ. As discussed before revivals will occur only on timescales long compared to the ones relevant for the experiment. For this reason the time evolution can be well described by a dephasing rate which is varying in space.

Both the effective dephasing rate $\Gamma(z, r_\perp)$ and the interaction potential of course depend on principal quantum number and excitation linewidth and thus have to be calculated for all experimental parameter sets individually. As an example, Fig. 6.7 (b) presents the calculation obtained for $|80D_{5/2}, m_j = 5/2\rangle$ for a bandwidth $\Omega_c = 2\pi \cdot 6.2\,\mathrm{MHz}$. This calculation clearly shows the anisotropic character of the Rydberg blockade, differing almost by a factor of two for the semi axis. More importantly, the figure shows that the dephasing rate $\Gamma(z, r_\perp)$ is not negligible outside the blockade radius.

6.3.3 *Numerical propagation of the wave function*

To simulate the transmission through the medium the effective dephasing model is incorporated in the equations describing the polariton propagation [12]. The results in this section are based on simulations by Przemyslaw Bienias. More detailed discussions can be found in his PhD thesis [141].

The simulations assume that the photon rate is so weak that only two polaritons are in the medium at the same time. These polaritons are described by a two-body wave function $\psi_{dd}(\boldsymbol{r}_1, \boldsymbol{r}_2)$ containing on polariton at position $\boldsymbol{r}_1$ and the other one at position $\boldsymbol{r}_2$. The propagation of this wave function through the medium is described by a full set of equations [38, 41], which are extended here by the dephasing rate $\Gamma(z, r_\perp)$ resulting in a decay of $\psi_{dd}(\boldsymbol{r}_1, \boldsymbol{r}_2)$. To simplify the calculations, the density distribution is assumed to be homogeneously distributed over a length $L = 4\sigma_z$. Adapting the length of the medium compensates for neglecting the wings of the Gaussian density distribution. On top, the calculations assume an effective beam waist $w_{\text{eff}} = 7$ µm to take into account the change of the waist over the length L of the medium. With these parameters the polariton dynamic is solved for different transverse distances $r_\perp$ including a one dimensional interaction potential $V_{1D}(z) = V(z, r_\perp)$. Subsequently the three-dimensional character of the system is obtained by averaging $r_\perp$ over the transverse beam profile.

The result of the simulation is shown in Fig. 6.8 (a) for $n = 80$, $\Omega_c = 2\pi \cdot 12$ MHz and $r_\perp = 4.2$ µm. The right hand side of this graph ($z > 0$) shows the probability $|\psi_{dd}|^2$ to find two polaritons in the medium. Here $R = (z_1 + z_2)/2$ is the center of mass coordinate while z is separation of the polaritons inside the medium. The simulation nicely reveals the decay of $|\psi_{dd}|^2$ for distances smaller 10 µm where the Rydberg blockade occurs. On top the simulation shows a slight broadening of the region where $\psi_{dd}|^2$ vanishes with increasing center of mass coordinate R. This feature is missing in the simple simulations in sec. (4.5) and has been discussed before as a diffusive behaviour [38]. While at the entrance the probability to find two Rydberg excitations is only determined by the Rydberg blockade, the dip broadens during the propagation due to the corrections to the linear polariton dispersion [96].

On the left hand side ($z < 0$) Fig. 6.8 shows the product of $|\psi_{dd}|^2$ and $\Gamma(z, r_\perp)$ for the parameters mentioned before. The calculation results in a peaked dephasing around $z \approx 10$ µm. Reason is that for shorter distances the probability amplitude ψ_{dd} decays due to the Rydberg blockade while for larger distances the rates $\Gamma(z, r_\perp)$ vanish.

Having found the amplitude of the two-photon wave function ψ_{dd} by the simulation, the rate of events $\mathcal{N}$ that at least one photon is converted into stationary Rydberg excitation is given by

$$\mathcal{N} = \int_V d\boldsymbol{r}_1 d\boldsymbol{r}_2 \Gamma(\boldsymbol{r}_1 - \boldsymbol{r}_2) |\psi_{dd}\boldsymbol{r}_1, \boldsymbol{r}_2)|^2, \tag{6.14}$$

where the Rydberg wave function is normalized to the incoming photon flux according to eq. (6.4). One such dephasing event leads to an average increase of optical depth OD_{im} for subsequent incoming photons. The resulting reduction in transmission caused by a

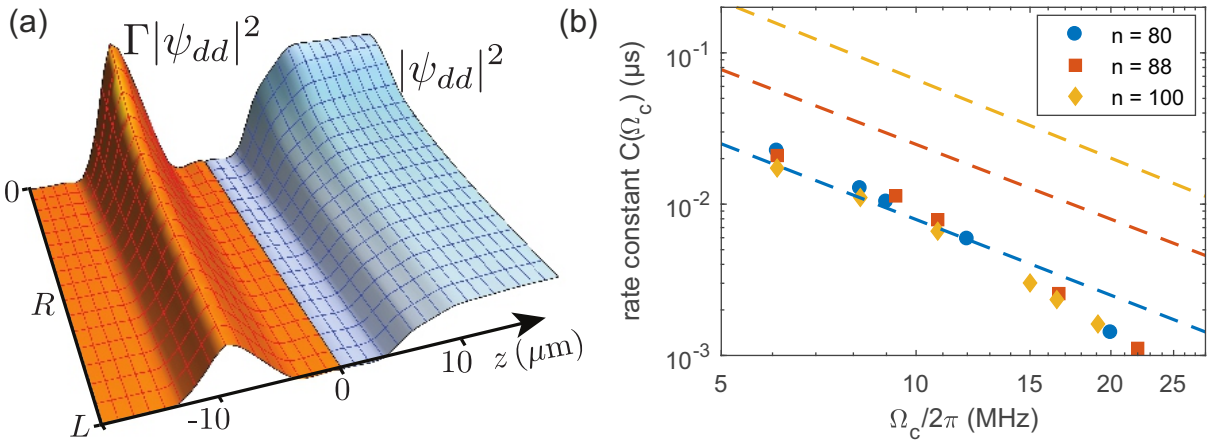

Figure 6.8: **Numerical simulation of the polariton propagation** (**a**) Right hand side (z>0): Numerical simulation of the probability amplitude $|\psi_{dd}|^2$ to find two polaritons propagating (center of mass coordinate $R = (z_1 + z_2)/2$ through the cloud at a distance z. Left hand side (z<0): Product of probability amplitude and dephasing rate $\Gamma(z, r_\perp)$ (**b**) Comparison of numerically calculated rate constants $C(\Omega_c)$ (points) and the fits to the data.

single dephasing event is thus given by $\exp(-OD_{dec} - OD_{sat}(R_{in}))\left(1 - e^{-OD_{im}}\right)$. As this decrease in transmission appears with the rate $\mathcal{N}$ the initial time evolution for the averaged transmission changes by

$$T(t) = e^{-OD_{dec} - OD_{sat}(R_{in})} \exp\left[-\mathcal{N}t\left(1 - e^{-OD_{im}}\right)\right] \tag{6.15}$$

leading to the rate constant $\mathcal{C}(\Omega_c) = \mathcal{N}\left(1 - e^{-OD_{im}}\right)/R_{in}^2$. The simulated rate constants $\mathcal{C}(\Omega_c)$ are presented in Fig. 6.8 (b) for the different experimental parameters. The numerical result show qualitative agreement with the experiment (lines from the fit to the data), but only quantitative agreement for low n and small values of Ω_c. Especially the strong scaling with main principal quantum number is not reproduced at all. A reason for this discrepancy might be the fact that for large Ω_c and n the ac-Stark shift caused by the coupling to the intermediate state $|e\rangle$ becomes comparable to the $nD_{5/2}$ and $nD_{3/2}$ manifold which scales with n^{-3}. In this situation the approach of first calculating the interaction potentials first and then including them into the polariton propagation is not justified anymore.

Even more crucial is that in the experiment an effective saturation of the transmission due to the finite lifetime of Rydberg atoms is observed. Inclusion of a higher number of impurities is however challenging in the simulation, as more than two polaritons have to be taken into account in this case. Yet, the higher number of impurities could play a major role for further dephasing events especially for high principal quantum numbers.

7 Single-Photon absorption from an arbitrary light field

The elementary operation of subtracting exactly one photon from an arbitrary light pulse is of great interest for testing fundamental concepts of quantum optics [142, 143], as well as for the preparation of non-classical states of light for quantum information [144, 145, 146, 147], simulation [148, 149, 150], and metrology protocols [151]. Heralded single-photon subtraction has been realized by monitoring the weak reflection of a highly imbalanced beam splitter, where a single detection event corresponds to subtraction of a photon from the transmitted pulse [152, 142]. For sufficiently low reflectivity such that the subtraction of two or more photons becomes negligible, this procedure implements the photon annihilation operator $\hat{a}$ [142]. This operation is inherently probabilistic, with a success rate depending on the number of incoming photons. In contrast, deterministic single-photon subtraction, where always exactly one photon is removed independent of the input photon state, can be implemented by sending the light through a medium saturable by a single absorption event. One realization of such a single-photon absorber is a single three-level quantum emitter strongly coupled to an optical resonator [153, 154], recently demonstrated by S. Rosenblum *et al.* using a single atom coupled to a microsphere resonator [155].

This chapter discusses the second project carried out during the scope of the thesis, published as an Editor's suggestion in Physical Review Letters [50]. The results demonstrate a deterministic single photon absorber removing a single photon from an input pulse containing up to $\overline{N}_{\text{in}} = 35$ input photons. The experiment is based on a proposal of J. Honer *et. al.* [51] utilizing the Rydberg excitation blockade to saturate an optically thick medium with a single photon. By measuring the amount of Rydberg atoms inside the medium it is shown that a single absorbed photon leaves behind exactly a single Rydberg excitation. This result adds a new component to the growing Rydberg quantum optics toolbox [37, 38, 41], which already contains photonic logic building-blocks such as single-photon sources [39], switches [120], transistors [47, 54, 48], and conditional π-phase shifts [42]. This approach is scalable to multiple cascaded absorbers, essential for preparation of non-classical light states for quantum information and metrology applications [152, 146, 156], and, in combination with the single-photon transistor, high-fidelity number-resolved photon detection [51, 157, 158].

7.1 A SINGLE RYDBERG ATOM IN AN ENSEMBLE OF ATOMS

The most fundamental system to think of in the field of quantum optics is one single photon strongly coupled to a single two-level atom. Unfortunately, the scattering cross section of a single atom with a single photon in free space scales with λ^2. The diffraction limit of light thus imposes an upper limit for the coupling strength [159]. Placement of a single atom in the node of a high quality resonator allows to enter the strong coupling regime due to the amplification of the electric field strength [15]. Yet another approach is the coupling of a single photon to a *Rydberg superatom*, an artificial atom consisting of a single Rydberg excitation and many ground state atoms [29, 30].

7.1.1 *The Rydberg superatom*

The formulae derived for the atom-light coupling in chapter 4 are based on considering a single atom coupled to a light field in the density matrix approach. Subsequently, assuming no interaction between the atoms the back action of the atomic polarizability onto the light field is derived by simple multiplication with the atom number. This approach fails as soon as interactions between atoms start to play a role. In the following the excitation dynamics of a single Rydberg atom in a ensemble of ground state atoms is discussed.

As already mentioned, the excitation blockade between individual Rydberg atoms can occur on distances larger than 10 µm if a high principal quantum number at low excitation bandwidth is chosen. Assuming an atomic density of 10^{12} cm^{-3} typically achieved in cold atomic gases, this results in a number of $N_{\text{blockade}} = 1000$ ground state atoms within one blockade sphere. By driving the system with a single atom Rabi frequency $\Omega = -\frac{e\mathcal{E}}{\hbar}\langle g|\boldsymbol{r}|r\rangle$, out of N ground state atoms only one single atom can be excited to the Rydberg state. Under the assumption of a constant atomic density and a homogeneous distribution of the laser intensity, the probability to be excited to the Rydberg state $|r\rangle$ is the same for all atoms. An intuitive example is to consider two atoms in their ground state located at positions r_1 and r_2, separated by less than the blockade radius. Let this state of the atoms be described by the product state $|g\rangle_{r_1} \otimes |g\rangle_{r_2}$. Rydberg excitation to $|r\rangle$ can thus either result in $|r\rangle_{r_1} \otimes |g\rangle_{r_2}$ where the atom in position r_1 was excited, or in $|g\rangle_{r_1} \otimes |r\rangle_{r_2}$ where the atom at position r_2 was excited. The excitation of a doubly excited state $|r\rangle_{r_1} \otimes |r\rangle_{r_2}$ is excluded a priori due to the Rydberg interaction. This example can easily be extended to more than one atom resulting in a number of $(N+1)$ *single atom states* consisting of one state with all atoms are in the ground state, and N excited states with one Rydberg excitation. In the following the labeling of the positions is for simplicity hidden in the position of the state, for example $|ggg\cdots r_j\cdots g\rangle$ means that all atoms but the one at position r_j are in the ground state. In analogy to the explanation

of superradiant decay [59] the many-body character of the excitation can be treated by introducing an entangled collective state

$$|\mathcal{W}\rangle = \frac{1}{\sqrt{N}} \sum_{j=1}^{N} \exp\left(-i\boldsymbol{k}\boldsymbol{r}_j\right) |g_1, g_2, g_3, \cdots, r_j, \cdots, g_N\rangle. \tag{7.1}$$

The phase factor $\exp(-i\boldsymbol{k}\boldsymbol{r})$ originates from the phase of the excitation laser at the position of the j-th atom excited to the Rydberg state. In accordance, the many-body ground state is defined as

$$|\mathcal{G}\rangle = |ggg\cdots gg\rangle. \tag{7.2}$$

Consequently, the collective Rabi frequency coupling the many body states $|G\rangle$ and $|\mathcal{W}\rangle$ becomes

$$\begin{aligned} \Omega_{\text{coll}} &= -\frac{e\mathcal{E}}{\hbar}\langle\mathcal{G}|\boldsymbol{r}|\mathcal{W}\rangle \\ &= -\frac{e\mathcal{E}}{\hbar}\frac{1}{\sqrt{N}}\sum_{j=1}^{N}\langle ggg\cdots gg|\boldsymbol{r}|g_1, g_2, g_3, \cdots, r_j, \cdots, g_N\rangle \\ &= \frac{1}{\sqrt{N}}\sum_{j=1}^{N}\Omega = \sqrt{N}\Omega. \end{aligned} \tag{7.3}$$

I.e. in comparison to the single atom Rabi frequency Ω the collective Rabi frequency Ω_{coll} is enhanced by a factor $\sqrt{N}$. This enhancement is shown in Fig. 7.1. A single atom driven with a Rabi frequency Ω oscillates with this frequency between the ground state $|g\rangle$ and the Rydberg state $|r\rangle$. Trivially, the maximum number of Rydberg atoms is one. An ensemble of N ($N = 9$ in Fig. 7.1) independent atoms shows oscillations with the same Rabi frequency, but the maximum number of Rydberg atoms changes to N as no blockade occurs. On the other hand N Rydberg atoms oscillate with $\Omega_{\text{coll}} = \sqrt{N}\Omega$.

Indeed, the two many-body states $|\mathcal{G}\rangle$ and $|\mathcal{W}\rangle$ introduced so far are not sufficient to span the same Hilbert space as the $N + 1$ single atom states. For completeness of the basis, another $N - 1$ states $|\mathcal{D}_j\rangle$ are required. However, it turns out that out of all states $|\mathcal{W}\rangle$ and $|\mathcal{D}_j\rangle$, the former one is the only one which is dipole coupled to the ground state $|\mathcal{G}\rangle$ via the light field [51].

As an example, for $N = 3$, one representation of the collective states calculated by means of the Gram-Schmidt process is

$$\begin{aligned} |\mathcal{W}\rangle &= \frac{1}{\sqrt{3}}\left(|rgg\rangle + |grg\rangle + |ggr\rangle\right) \\ |\mathcal{D}_1\rangle &= \frac{1}{\sqrt{6}}\left(-|rgg\rangle + 2|grg\rangle - |ggr\rangle\right) \\ |\mathcal{D}_2\rangle &= \frac{1}{2}\left(-|rgg\rangle + |ggr\rangle\right). \end{aligned} \tag{7.4}$$

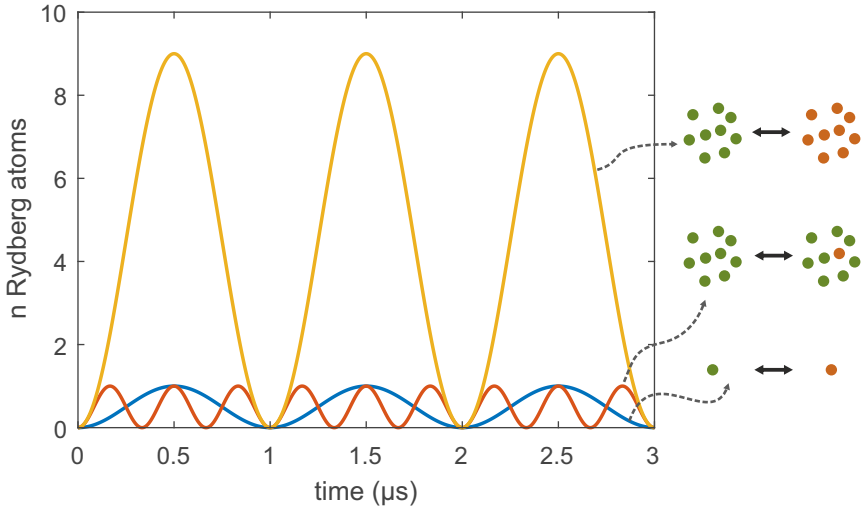

Figure 7.1: **Undamped collective Rabi oscillations** A single atom driven with a Rabi frequency Ω oscillates between its ground state $|g\rangle$ and its Rydberg state $|r\rangle$. The Rabi frequency does not change if the same driving field is applied to a number of $N = 9$ independent atoms. However, when the Rydberg blockade is strong enough to allow only the excitation of a single Rydberg atom out of an ensemble of atoms, the many body character results in a collective Rabi frequency $\Omega_{\text{coll}} = \sqrt{N}\Omega$.

Evaluating eg. (7.3) for $|\mathcal{D}_1\rangle$ and $|\mathcal{D}_2\rangle$ yields $\Omega_{\text{Dark}} = 0$ and thus no coupling by the light field. For this reason $|\mathcal{W}\rangle$ is referred to as bright state, while the $|\mathcal{D}_j\rangle$ are called dark states. To describe the coherent atom light coupling it is thus sufficient to take into account only two collective states. This reduction in the presence of strong interaction has triggered the terminology *superatom*. An atom which acts like a conventional two-level emitter but with collectively enhanced Rabi frequency.

Experimentally, the enhancement of the Rabi frequency by a factor of $\sqrt{N}$ has been observed for the first time by confining single atoms in two tightly focused optical tweezers separated by less than a blockade radius [29, 30]. More recently, it was also investigated in mesoscopic ensembles trapped in an optical lattice [160] and brought to the Mott-insulator phase [53]. Observation in larger ensembles with dimensions extending the blockade radius is quite challenging. Inhomogeneous density distributions lead to a spatially varying enhancement of the Rabi frequency, which results in strong dephasing of the oscillations [161].

In these experiments (except of [160]) the $\sqrt{N}$ enhancement was observed by measuring the oscillating Rydberg fraction. For the implementation of the single-photon absorber however, yet another modification of the superatom in comparison to a normal atom is relevant. According to eq. (4.30) the optical density the probe light experiences on a two photon Raman transition is solely dependent on tunable parameters Ω_c, Δ_c and the resonant optical density OD of the $|g\rangle \leftrightarrow |r\rangle$ transition. The therefore achievable strong coupling in combination with the reduction to effectively one single two-level atom makes the superatom coupled to a quantized light field a promising candidate for a multitude of quantum optics applications.

7.1.2 *Collective Rydberg excitation with damping*

For the realization of a single photon absorber the strong coupling of the light field to the atomic levels is not sufficient. After the absorption of the first photon the medium has to be saturated to not allow the absorption of a second photon. Indeed, the excitation blockade guarantees the absorption of only a single photon at a time, but the superatom can still undergo Rabi oscillations with the enhanced Rabi frequency. As the Rabi oscillations result in a series of photon emission and absorption events, absorption of a single photon can only be achieved by fulfilling stringent demands on the timing of the pulse. This is incompatible with a deterministic absorber providing a high fidelity, independent on the shape of the light pulse. In fact, it demands a mechanism damping the Rabi-oscillations and freezing the Rydberg excitation which is created by the absorption of the first photon. Such a scheme is proposed by J. Honer *et. al.* in [51].

In sec. (7.1.1) the transformation into the many-body basis composed of the collective state $|\mathcal{G}\rangle$, $|\mathcal{W}\rangle$ and $|\mathcal{D}_j\rangle$ was introduced. The fact, that on the one hand an applied light field does not couple the many-body ground state with the $N-1$ dark states, but on the other hand the dark states carry a Rydberg fraction, suggests following scheme: First, a light field couples ground state $|\mathcal{G}\rangle$ and bright state $|\mathcal{W}\rangle$ yielding both a Rydberg excitation in the medium and the loss of a photon. Subsequently, coupling of the bright state to the dark state $|\mathcal{D}_j\rangle$ decouples the Rydberg excitation from the light field.

The proposal of Honer *et al.* demonstrates that such a controlled coupling of dark and bright states can be introduced into the system by adding a spatially and temporally varying detuning $\Delta(t)$ for each atom. Without going further into detail [162], these detunings act like an effective dephasing with a rate Γ_n of the bright state into the dark states. Fig. 7.2 shows results obtained by solving the Master-equation derived in the proposal for different dephasing rates Γ_n, $N = 16$ atoms and a single atom Rabi frequency $\Omega = 2\pi \cdot 1\,\mathrm{MHz}$. When Γ_n is chosen to be zero (blue line), no dephasing occurs, the system oscillates with the collective Rabi frequency $\Omega_\mathrm{coll} = 4\Omega$ between state $|\mathcal{G}\rangle$ and $|\mathcal{W}\rangle$ as discussed before. As soon as the coupling to the dark states is added, depending on the strength of Γ_n three different regimes can occur in direct analogy to a classical damped harmonic oscillator. All of these have a steady state with a high Rydberg fraction f_R in common. The amount of f_R is solely determined by the number N of atoms contributing to the superatom scaling with $f_R = \frac{N}{N+1}$ [51], thus converging against unity for $N \gg 1$. This result is in strong contrast to the damping of Rabi oscillations originating from a single-atom decay, providing only $f_R = 0.5$ for strong coupling.

For $\Gamma_n < \Omega_\mathrm{coll}$ (red line) the underdamped regime is entered. The superatom still shows a few oscillations with decreasing amplitude before the bright state eventually completely dephases into the dark states, such that the Rydberg excitation is decoupled from the light field with an effective decay rate $\Gamma_\mathrm{eff} = \Gamma_n/2$. On the other hand, $\Gamma_n \gg \Omega_\mathrm{coll}$ (purple line) corresponds to the overdamped regime occurring in the harmonic oscillator. In this parameter range no oscillations show up, but the superatom only slowly evolves into the dark states. The timescale of this evolution increases linearly with the damping

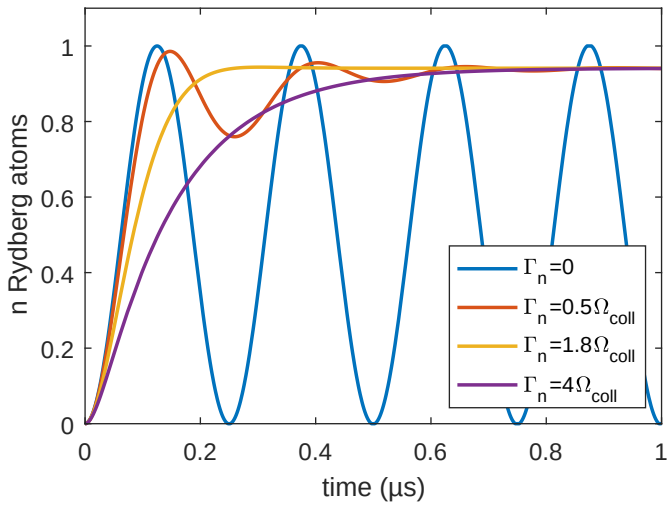

Figure 7.2: **Dephasing of collective Rabi oscillation by coupling to Dark states** A dephasing rate Γ_n coupling the collective bright state $|\mathcal{W}\rangle$ with the dark states $|\mathcal{D}_j\rangle$ results in a damping of the collective Rabi oscillations showing up in a superatom containing $N = 16$ atoms. Independent on strength of Γ_n the Rydberg fraction converges to $f_R = N/(N+1)$ on long timescales. Optimum dephasing is reached in the critically damped regime with $\Gamma_n \approx 2\Omega_{\text{coll}}$.

rate for given Ω_c. Both afore mentioned regimes are not an ideal candidate for the implementation of the single photon absorber as the reciprocal of the dephasing rate sets a lower boundary on the required pulse duration.

$\Gamma_n \approx 2\Omega_{\text{coll}}$ (yellow line) yields the optimum dephasing rate to realizing an efficient single-photon absorber. When entering this critically damped regime dephasing into the dark states occurs approximately on the timescale of a Rabi cycle with Ω_{coll}.

7.2 INFLUENCE OF ABSORPTION ON THE PHOTON STATISTICS

The trivial effect of a deterministic single-photon absorber onto an incident light field is the removal of exactly one photon. This results in an impact on two other quantities, the shape and the photon statistics of the transmitted photon pulse. While the former is intuitive as photons are predominantly absorbed from the beginning of the pulse, the latter requires further discussions.

For the experiments discussed in this chapter it is important to note again that the weak probe beam is realized by strongly attenuating a laser beam. As a laser generates coherent light, the number of photons contained in a probe pulse is underlying Poissonian photon statistics

$$p_k(\lambda) = \frac{\lambda^k}{k!} e^{-\lambda}, \tag{7.5}$$

i.e. a single pulse contains an amount of k photons with a probability p_k. Averaging over all pulses results in the mean photon number λ, which can be adjusted in the experiment by applying a rf-field with a certain power to the AOM. At the same time the variance of the Poissonian probability distribution is equal to the mean photon number λ, independent of any other parameters and if no drifts occur in the experiment. Any purely probabilistic removal of photons from a light pulse does not change this relation of mean photon number and variance. A suitable measure of the deviation of a counting statistic from Poissonian statistics is the Mandel-Q parameter

$$\mathcal{Q} = \frac{Var(n)}{\overline{n}} - 1, \tag{7.6}$$

introduced by Mandel [163]. Resulting from the equality of mean value and variance this value yields zero for a Poissonian distribution. For a more narrow distribution (sub-Poissonian) $\mathcal{Q}$ becomes negative with the lower bound $\mathcal{Q} = -1$ when the distribution n consists of a single value. On the other, distributions broader than the Poissonian distribution can reach arbitrarily large values of $\mathcal{Q}$.

The fundamental property of a single-photon absorber is removal of exactly one photon from a pulse, independent on the number of input photons. Using pulses with Poissonian statistics as input, this property results in a redistribution of the probabilities p_k. Zero events occur with a probability $p_{0,\text{trans}} = p_{0,\text{input}} + p_{1,\text{input}}$, the probability for transmitting $k > 1$ photons is given by $p_{k,\text{trans}} = p_{k+1,\text{input}}$. Consequently, the mean photon number after applying single photon subtraction is reduced by one. At the same time the width of the distribution remains the same, resulting in super-Poissonian statistics with $\mathcal{Q} > 0$. Fig. 7.3 (a) visualizes this broadening for a mean input number $\lambda = 5$. The strength of the broadening, expressed in Fig. 7.3 (b) as $\mathcal{Q}$ parameter, strongly depends on the mean input photon number λ. For large λ subtraction of a single photon has only a small impact on both width and mean value of the distribution. For very small λ the zero photon component of the pulse which remains unchanged by the single photon absorber is not negligible in the distribution. As a consequence the strongest change of the photon statistics occurs around $\lambda \approx 1.7$.

Experimentally the photon statistics can be in principle measured by evaluating the transmitted photons in histograms and determining the width and mean number of the distributions. However, finite detection efficiency of only 30% realized in the experiment strongly smears out both the histograms of input and output photon number. Better contrast can be obtained by measuring temporal correlation functions in a Hanbury-Brown-Twiss setup, where super-Poissonian photon statistics shows up as photon bunching.

7.3 REALIZATION OF A MEDIUM BLOCKADED BY A SINGLE EXCITATION

Stringent demand for the Rydberg-based realization of a single-photon absorber is, beside besides the required dephasing mechanism described in sec. (7.1), an atomic cloud with a length smaller than the blockade radius. To realize this constraint, the additional dimple

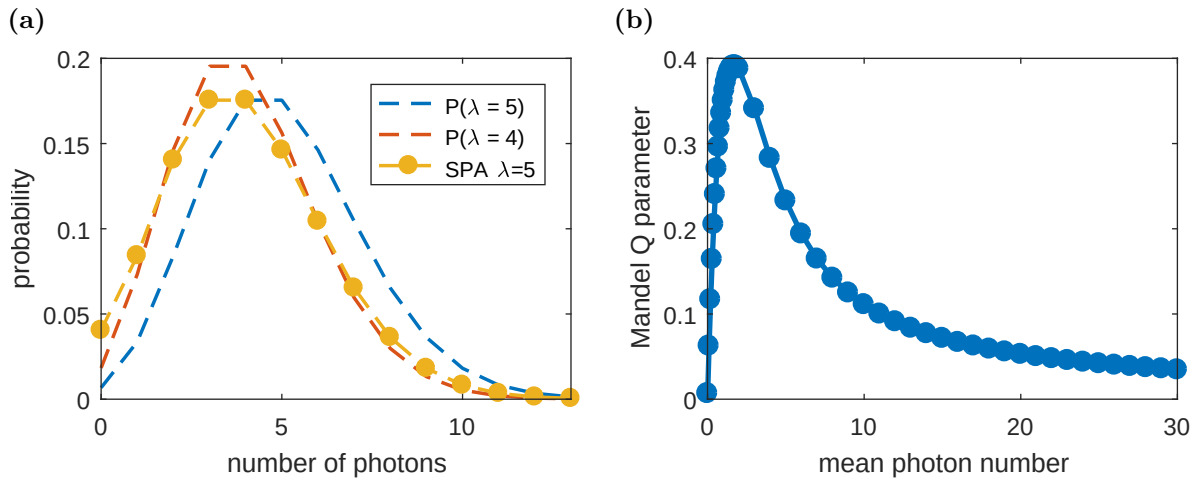

Figure 7.3: **Influence of the single photon absorber on the photon statistics** (**a**) Single Photon absorption (SPA) from a Poissonian input pulse reduces the mean photon number by one. At the same time the width of the distribution remains unchanged resulting in a super-Poissonian photon statistic. (**b**) Mandel Q parameter for different mean input photon numbers. The peak value of $\mathcal{Q}$ appears at a mean photon number $\lambda \approx 1.7$

laser was added to the experimental setup (c.f. sec. (5.2.1)), allowing to reduce the length of the cold atomic cloud in the direction of the probe light propagation. In combination with Rydberg states with high principal quantum number $n > 100$ this allows to fulfill the constraint. It turned however out that saturating the medium with a single Rydberg excitation requires some tweaking of the parameters.

Experimental evidence that Rydberg blockade exceeds the size of the medium such that only a single Rydberg atom can be excited, can be either found by measuring the loss of exactly a single photon from the input pulse, or by directly measuring the amount of Rydberg atoms via field ionization at large input photon numbers $\overline{N}_{in}$. To find the ideal experimental parameters the latter one is more suited, as measuring a small number of Rydberg atoms on a tiny background requires statistic than measuring the lack of exactly a single photon on a large signal photon background. Fig. 7.4 the number of field ionized Rydberg atoms for both a low input photon number $\overline{N}_{\text{in}} = 3.2$ (a) and a high input photon number $\overline{N}_{\text{in}} = 12.3$ (b), measured by scanning the probe detuning Δ_p over the two-photon resonance $\Delta_p = \Delta_c + \frac{\Omega_c^2}{4\Delta_c}$.

In each subplot, the spectrum is measured in two-different configurations. For the spectra shown in blue, both the crossed ODT and the dimple are switched off during the measurement, i.e. the atoms expand in free space. The spectra shown in red on the other hand, are measured by only switching off the crossed ODT during the measurement, but keeping the dimple laser turned on. As a consequence, atoms which are trapped inside the dimple beam experience a ac-Stark shift caused by the laser field. The resulting shift can be clearly seen in the measurement at low photon number, for which the amount of Rydberg atoms in the cloud does not saturate. While the signal with both traps

switched off shows a maximum at $\Delta_p = 2\pi \cdot 46.6$ MHz, the maximum shifts to $\Delta_p = 2\pi \cdot 47.8$ MHz when the dimple is kept on. This observed value is in agreement with the depth of the dimple calculated in sec. (5.2.1). Besides the frequency shift, the Rydberg line measured when the dimple is kept on broadens as a result of the spatially varying potential imposed onto the 8 μK cold atomic cloud. Therefore atoms located at different positions experience different ac-Stark shifts.

Increasing the number of photons contained in the pulse to $\overline{N}_{\text{in}} = 12.3$ results in the saturation of the number of Rydberg atoms. This causes a clear broadening of the measured Rydberg excitation line. On top, in the spectrum measured with the dimple turned clearly two maxima appear, one of them at the frequency corresponding to the resonance in free space. The interpretation of this double structure is following: Loading the dimple trap does not evaporate all atoms into the global minimum of the trap, some atoms remain outside the dimple beam. When now large number of input photons are sent into the medium, absorption saturates in the center of the trap, but atoms can still be excited to the Rydberg state at positions further outside. However, since the ac-Stark shift in the dimple is still strong enough to shift the different contributions apart from each other, it can be used to selectively address the atoms inside the dimple only.

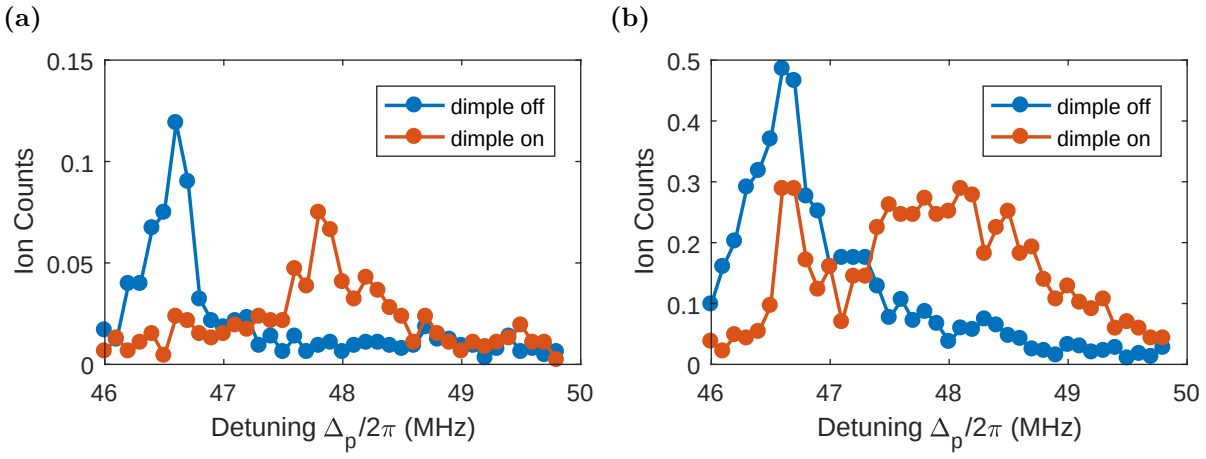

Figure 7.4: **Rydberg excitation inside the dimple beam** Rydberg excitation spectra measured for mean photon numbers per pulse of $\overline{N}_{\text{in}} = 3.2$ (**a**) and $\overline{N}_{\text{in}} = 12.3$ (**b**). Keeping on the dimple laser during the measurement results in an ac-Stark shift of the Rydberg line and broadening due to the spatially varying intensity of the dimple light. At large input photon number the spectrum broadens due to saturation of the number of Rydberg atoms. The measurement with the dimple turned on shows two maxima, suggesting that not all atoms are located inside the dimple.

The saturation of the spectrum measured in the dimple laser suggests that the medium is blockaded by a single Rydberg excitation. Stronger evidence is provided by measuring the number distribution of ionized Rydberg atoms in a single experiment shot. The histograms resulting from measurements resonantly addressing the respective center of the excitation line are shown in Fig. 7.5 for a measurements with both traps switched

off (a) and with the dimple still kept on (b). For the presented measurements a photon number of $\overline{N}_{\mathrm{in}} = 17.1$ was chosen, which is far above saturation.

When both traps are switched off the measurements reveal a mean number of field ionized Rydberg atoms of $\lambda = 1.2$. Taking into account the detection efficiency of only 28%, this yields a mean number 4.29 Rydberg atoms excited per experiment shot. This value is of course clearly differing from 1. At the same time, the Mandel-Q parameter calculated from the histogram according to eq. (7.6) is $\mathcal{Q} = -0.13$. As a consequence, the measured distribution of counts differs only slightly from a Poissonian distribution with the same mean value (compare red line).

When the same measurement is performed by selecting only the atoms in the dimple by means of the ac-Stark shift, the mean count of ionized Rydberg atoms reduces to 0.28 which corresponds to one Rydberg excitation when including the detection efficiency of the ion detector. At the same time the Mandel-Q parameter of this measurement reduces to $\mathcal{Q} = -0.253$ and the number of two clicks on the detector at the same time become negligible. As the Mandel-Q parameter is reduced by a finite detection efficiency to $\mathcal{Q} = -\eta$ this measurement reveals the full saturation of the atomic cloud by a single Rydberg atom.

As a consequence of this result, all experiments for the single photon absorber presented in the following are carried out with the dimple trap kept on, such that a single Rydberg atom leads to the full blockade. As a side effect, this contributes to the dephasing required for the damping of the Rabi oscillations, as the ac-Stark effect spatially varies the resonance condition.

7.4 MEASUREMENT OF THE PHOTON NONLINEARITY

Having found evidence that only a single Rydberg atom can be excited with high fidelity due to the Rydberg blockade in the atomic medium, the medium allows to study the absorption of a single photon. A optimization of the optical density on strong absorption, results in a cloud containing 25000 atoms with a longitudinal radius of $\sigma_z = 6$ µm and a transversal radius of $\sigma_r = 10$ µm. The temperature limited by the heating rate of the dimple trap is 8 µK. Measuring the optical depth of this geometry by scanning the probe frequency over the transition form the initial state $|g\rangle = |5S_{1/2}, F = 2, m_F = 2\rangle$ to the intermediate state $|e\rangle = |5P_{3/2}, F = 3, m_F = 3\rangle$ yields $OD_b = 12.5$. The selected Rydberg state $|r\rangle = |121S_{1/2}, m_J = 1/2\rangle$ yields a Rydberg blockade radius $r_B \approx 17$ µm significantly exceeding the size of the atomic cloud. For efficient Rydberg excitation, both probe and control laser are detuned from the intermediate state by a detuning $\Delta_c = 2\pi \cdot 100$ MHz. The calculated, spatially averaged probe Rabi frequency is $\Omega_p = 2\pi \cdot 33\sqrt{\frac{\text{photons}}{\mu\text{s}}}$ kHz, while the control Rabi frequency is measured by an EIT scan to be $\Omega_c = 2\pi \cdot 10$ MHz. The resulting ac-Stark shift of the Rydberg line is $\Omega_c^2/4\Delta_c = 2\pi \cdot 250$ kHz, which has to be taken into account for the probe detuning.

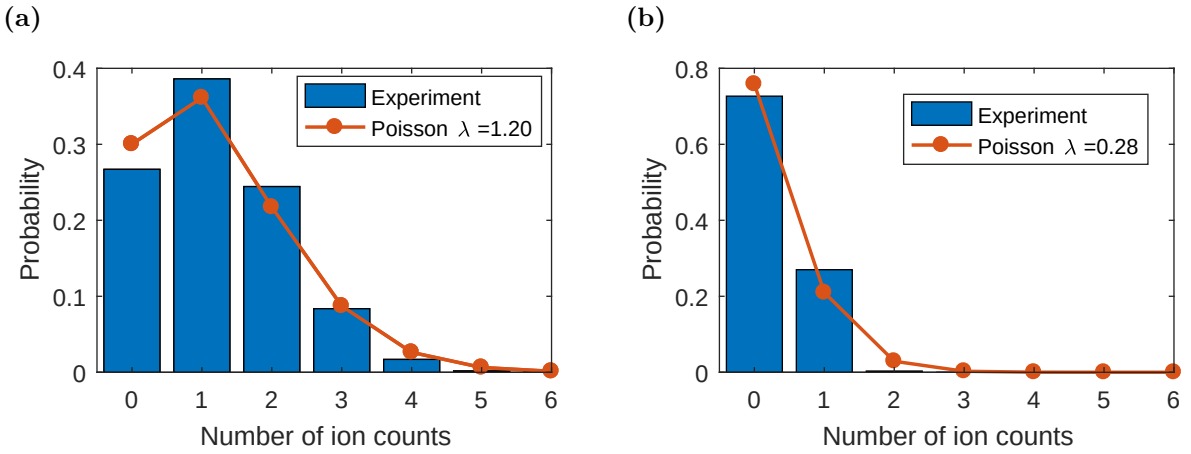

Figure 7.5: **Counting statistics of ionized Rydberg atoms** (**a**) Histogram of the ion counting statistic at a input photon number $\overline{N}_{\text{in}} = 17$ when both crossed ODT and dimple are switched off during the experiment time. The histogram reveals a mean count number of $\overline{N}_{\text{counts}} = 1.2$, corresponding to a corrected mean ion number of $\overline{N}_{\text{ions}} = 4.29$, and a Mandel-Q parameter $\mathcal{Q} = -0.13$. The medium is clearly not blockaded by a single excitation. (**b**) Measurement for the same parameters, but with the dimple beam switched on. The mean number of $\overline{N}_{\text{ions}} = 0.28$ corresponds to exactly the excitation of exactly one Rydberg atom (within the errorbars of the detection efficiency). At the same time the Mandel-Q parameter reduces to $\mathcal{Q} = -0.25$, close to the minimum value the parameter can have at the finite detection efficiency in the experiment.

To study the saturation of the medium, Tukey-shaped input probe pulses with mean photon number $\overline{N}_{in}$ and a duration $\tau \approx 2$ µs are sent through the medium. The mean number of transmitted photons $\overline{N}_{out}$ is measured using four avalanche single-photon detectors (SPCM) in two Hanbury-Brown-Twiss setups (HBT). The choice of Tukey-shaped pulses offers a tradeoff between Gaussian shaped pulses and rectangular pulses, providing both constant Rabi frequency over almost the total duration of the pulse and still narrow width in frequency space due to the smoothed edges. To guarantee constant coupling to $|r\rangle$ the intensity of the control light is kept constant over the whole duration of the probe pulses. After each pulse the presence of a Rydberg atom is probed by applying a field ionization pulse converting any Rydberg atoms into Rb^+ ions which are subsequently detected on the micro-channel plate. Additionally, this removal of Rydberg atoms from the sample allows a fast repetition rate of the experiment. A number of 1000 individual measurements in a single MOT cycle provides fast data acquisition with the required statistics.

Experimentally first a spectrum of the probe laser at a very small input photon number $\overline{N}_{in} = 0.2$ is taken with both control laser turned on and off. At such a small photon number the probability to find two photons in a single pulse is negligible. When the control laser is turned on, this measurement allows to determine the probability $p_{\text{Ryd}} =$

0.35 to convert a single incident probe photon into a Rydberg excitation. On the other hand turning the control field off yields the residual probability $p_{\text{scatt}} = 0.01$ to scatter a probe photon from the intermediate state at $\Delta_p = 2\pi \cdot 100$ MHz. This value is in very good agreement to the model derived for a two-level system in sec. (4.2.1) for $OD = 12.5$.

For the implementation of a deterministic single photon absorber, a single photon should be absorbed with a probability $p_{\text{Ryd,deterministic}} = 1$. According to eq. (4.30) the effective optical density of the probe field on the Raman transition OD_{Raman} can be tuned by the experimental accessible parameters Ω_c, Δ_c and OD (although increasing OD more in this trap configuration is not possible in this apparatus). However, since the Raman induced decay rate shows the same dependence on Ω_c and Δ_c, the ratio of these values has to be constant. Thus, OD_{Raman} can only be increased by OD and subsequently adapting to control Rabi frequency and detuning to end up with the same value for p_{scatt}. As an example, $OD = 70$ with $\Omega_c = 2\pi \cdot 25$ MHz and $\Omega_c = 2\pi \cdot 25$ MHz results in $p_{\text{Ryd}} = 0.87$.

Since for $\overline{N}_{in} \ll 1$ no saturation occurs, the effective dephasing rate $\gamma_r = 2\pi \cdot 500$ kHz can be extracted by fitting the observed Rydberg absorption line with the solution of the Master-equation for the tree-level system including the lifetime of the Rydberg state $\tau_{\text{Ryd}} = 530$ µs (sec. (4.3)). In fact, the Rydberg state lifetime for the experiments is mainly determined by the spontaneous Raman decay rate $\gamma_{\text{Raman}} = \left(\frac{\Omega_c}{2\Delta_c}\right)^2 \Gamma_e = 2\pi \cdot 15$ kHz, corresponding to a Rydberg lifetime of $\tau_{\text{Ryd,Raman}} = 10$ µs. This value is experimentally determined to be $\tau_{\text{Ryd,Raman}} = 15$ µs.

The measured dephasing rate γ_r can be assigned to three main effects occurring in the experiment without applying additional external noise. First, thermal motion of the atoms results in intrinsic dephasing of the bright state $|\mathcal{W}\rangle$ [122, 164]. For fully coherent evolution including the $\sqrt{N}$ enhancement, the bright state $|\mathcal{W}\rangle$ can pick up a global phase, but the relation of the individual phases in eq. (7.1) has to remain constant. However, at finite temperature thermal movement results in a random redistribution of atoms. Consequently, the position of the j-th atom changes from $\boldsymbol{r}_j$ to $\boldsymbol{r}'_j = \boldsymbol{r}_j + \boldsymbol{v}_j t$, where $\boldsymbol{v}$ is the Boltzmann distributed velocity of the atom. Thus, the overlap with the initially excited bright state diminishes over time and introduces decoherence in the atom light coupling. By defining the thermal decoherence time τ_{thermal} as point in the time evolution where the overlap with the initial bright state has degraded to $1/e$, the thermal decoherence rate becomes [122]

$$\gamma_{\text{thermal}} = \frac{1}{\tau_{\text{thermal}}} = \frac{2\pi v_s}{\lambda}. \tag{7.7}$$

Here $v_s = \sqrt{k_B T / m_{\text{Rb}}}$ is the average velocity of the atoms at a temperature T of the ensemble and $\lambda = \left[1/\lambda_p + 1/\lambda_c\right]^{-1}$ is the wavelength corresponding to the transition from $|g\rangle$ to $|r\rangle$. For the experimental parameters $T = 8$ µK and $\lambda = 297$ nm the expected thermal decoherence rate is $\gamma_{\text{thermal}} = 2\pi \cdot 93.1$ kHz.

Second, as all experiments are performed in-trap, the two-photon resonance becomes spatially dependent due to the trap induced ac-Stark shift. This is equivalent to inhomogeneous dephasing [51]. The strength of the broadening is determined by the temperature of the sample, defining how far the atoms are distributed apart from the trap center where the trapping potential is less deep. A simple estimation yields a contribution $\gamma_{\text{trap}} = \frac{k_B T}{\hbar} = 2\pi \cdot 167$ kHz.

Finally, elastic collisions of the Rydberg electron with ground state atoms lead to the formation of cold atomic molecules [165]. In spectra taken at low quantum number, such weakly bound molecules result in a series of red shifted lines corresponding to different numbers of ground state atoms bound in the orbit of a single Rydberg atom. At large principal quantum numbers, with $n > 80$, these individual molecular lines cannot be resolved any more. The position of the Rydberg line rather experiences a red shift linear to the atomic density [166]. As a consequence, the inhomogeneous density distribution of the experiment causes a position dependent shift of the Rydberg line. This effect has been explored as main dephasing effect in storage and readout experiments before [120]. For the atomic densities on the order of 10^{12} cm^{-3} in the experiment, the resulting dephasing rate is $\gamma_{\text{density}} \approx 2\pi \cdot 100$ kHz.

In combination with line broadening caused by inhomogeneities of the electric field on the length scale of the atomic sample, the dephasing rates estimated above agree well with the measured effective dephasing $\gamma_r = 2\pi \cdot 500$ kHz.

The observed dephasing rate and Rydberg lifetime determine the optimal probe pulse duration and collective Rabi frequency Ω_{coll}. The pulse should be longer than $1/\gamma_r$, while $\Omega_{\text{coll}} \approx \gamma_r$, to ensure that the collective excitation reliably dephases into a stationary Rydberg excitation during the probe pulse duration [51]. At the same time, the pulse must be short compared to the Rydberg atom lifetime, such that the initial excitation blocks the medium for the full pulse duration. In this specific experiment, the Rydberg lifetime is set by the spontaneous Raman decay rate γ_{Raman} due to admixture of the intermediate state by the detuned control field. Spontaneous or black-body radiation induced transitions as well as inelastic collisions with ground state atoms result in much smaller decay rates for $|r\rangle = |121S_{1/2}\rangle$ and the atomic density in the experiment [167, 168].

Fig. 7.6 shows the mean number of probe photons transmitted through the atomic medium $\overline{N}_{out}$ as a function of the mean input photon numbers $\overline{N}_{in}$ per probe photon pulse. When the control field is turned off, the probe transmission $t = 1 - p_{\text{scatt}} = 0.99$ is independent of the input photon number (solid line). In contrast, when the control field is turned on (circles), a strongly nonlinear transmission occurs. In case of weak probe input $\overline{N}_{in} < 10$, the number of absorbed photons is determined by the Poissonian statistics of the coherent probe field and the finite Rydberg absorption probability $p_{\text{Ryd}} = 0.35$ determined before. On the other hand for $\overline{N}_{in} > 10$, the mean number of transmitted photons is reduced by one, independent of the input photon number. Averaged over all data with $\overline{N}_{in} > 10$ the number of extracted photons per pulse is $\Delta\overline{N} = 0.98(13)$.

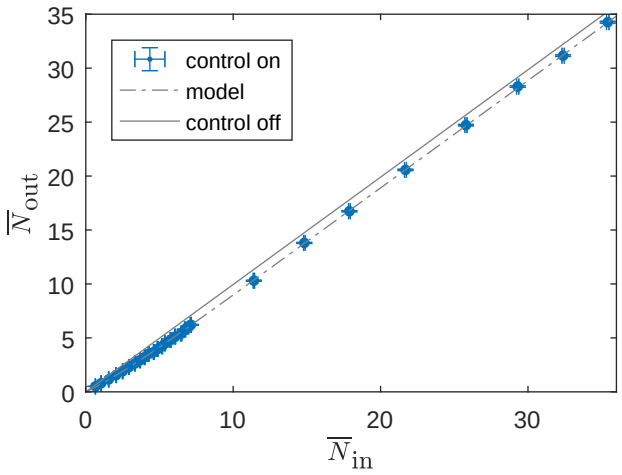

Figure 7.6: **Measured photon nonlinearity** The number of photons transmitted through the medium $\overline{N}_{out}$ is plotted against the number of input photons $\overline{N}_{in}$ (circles). Each datapoint is the average of 250000 experiment repetitions. The solid line shows the measured linear transmission when the control field is off, limited by the finite transmission $t = 0.99$ of the probe field at a detuning of $\Delta = 2\pi \cdot 100$ MHz. The dash-dotted line shows the calculated output photon number according to eq. (7.8) with the measured absorption probability $p_{\mathrm{Ryd}} = 0.35$. The number of transmitted photons is reduced exactly by one over a large range of input photon numbers.

A simple derivation based on the Poissonian probability distribution of photons in a single pulse yields the expression

$$\overline{N}_{out} \;=\; t \cdot \overline{N}_{in} + \exp\left(-t \cdot \overline{N}_{in} \cdot p_{\mathrm{Ryd}}\right) - 1, \tag{7.8}$$

which models the behaviour of a single-photon absorber with $p_{\mathrm{Ryd}} = 0.35$ and $t = 0.99$ but otherwise ideal performance. The dash dotted line representing this expression agrees very well with the experimental data, suggesting that the medium is indeed saturated by a single absorption event.

To make this claim even stronger Fig. 7.7 (a)-(c) shows the corresponding statistics of field ionized Rydberg atoms recorded with the MCP. The mean ion number $\overline{N}_{\mathrm{ions}}$ shown in subplot (a) saturates at 0.28 ions per pulse at mean input photon numbers $\overline{N}_{\mathrm{in}} > 10$. This number is solely limited by the finite detection efficiency η of the MCP in the experiment. As discussed in sec. (7.3) evaluation of the Mandel-Q parameter according to eq. (7.6) sheds light on the quality of the blockade. The values of $\mathcal{Q}$ in Fig. 7.7 (b), obtained from the number distribution of the experimental data at a given photon number $\overline{N}_{\mathrm{in}}$, saturate as well for $\overline{N}_{\mathrm{in}} > 10$, but in contrast to the mean ion number at $-\eta$, which is the lower bound for a finite detection efficiency. Both the observed mean ion counts and the Mandel-Q parameters agree very well with the results expected according to eq. (7.8) based on the assumption that each Rydberg excitation resulting from the absorption of a photon is subsequently converted into an ion and detected with $\eta = 0.28$.

Finally, Fig. 7.7 (c) presents the calculated ratio of Mandel-Q parameter to mean number of detected ions. For perfect Rydberg blockade this value should be constant at -1 for all input photon numbers $\overline{N}_{in}$. Instead, the experimental data reveals a slight increase from -0.98 at $\overline{N}_{in} = 3$ to -0.91 at $\overline{N}_{in} = 35$. This effect cannot be explained with the simple model of eq. (7.8) permitting only the excitation of a single Rydberg atom by absorption of a single photon.

Inclusion of a second excitation into the analytic expression of eq. (7.8) is mathematically challenging. In lieu thereof, the dashed yellow lines in Fig. 7.7 show the results of a numerical Monte-Carlo simulation of the absorption process including the possibility to absorb a second photon even if the medium is already blockaded. For this simulation each pulse is assembled by an array of bins with a duration of $\mathrm{t_{bin}} = 50$ ns duration. To each of the bins an intensity amplitude is assigned according to the envelope function of the pulse and normalized to the mean number $\overline{N}_{in}$ of photons contained in the pulse. Subsequently for each bin a random Poissonian number with a mean value corresponding to the intensity amplitude is drawn to determine the number of photons contained in a bin. By repeating this procedure 10^7-times the input pulses are generated for each input photon number.

After the generation of the pulses, the absorption is simulated by going through each time bin of each pulse and determining for each photon individually if it is absorbed or not by comparison of a random number against the absorption probability p_{Ryd}. With this procedure the analytic model of eq. (7.8) can be verified. If one photon has already been absorbed, the absorption of a second photon can now be allowed by comparing another random number to a much smaller probability $p_t extRyd2$. This simulation yields the fill statistics of both the transmitted photons and the created Rydberg atoms. In particular, the simulation reproduces the observed ratio of Mandel-Q parameter and mean ion number for a chosen value of $p_{\mathrm{Ryd2}} = 0.001$ (orange dashed line in Fig. 7.7). This suggests that the Rydberg blockade prevents excitation of a second Rydberg atom with very high, but not unit, fidelity. One reasonable suspicion is that this is due to the more complex nature of the Rydberg-Rydberg interaction than the usually assumed single van-der-Waals potential as shown in chapter 3, resulting in resonances for two-atom excitation within the conventional blockade volume [169, 170]. Note that the numerics including $p_{\mathrm{Ryd2}} = 0.001$ result in negligible difference compared to eq. (7.8) for the number of absorbed photons and excited Rydberg atoms over the shown input photon range. This effect only becomes visible by analyzing the full ion statistics.

7.4.1 *Pulse shape and Correlation*

Any process which deterministically removes the first photon from a light pulse will result in distortion of the pulse, reducing the purity of the output photon state [171]. While this is unproblematic for applications such as number-resolved photon detection, it imposes limits on the fidelity of photonic quantum state preparation based on photon subtraction

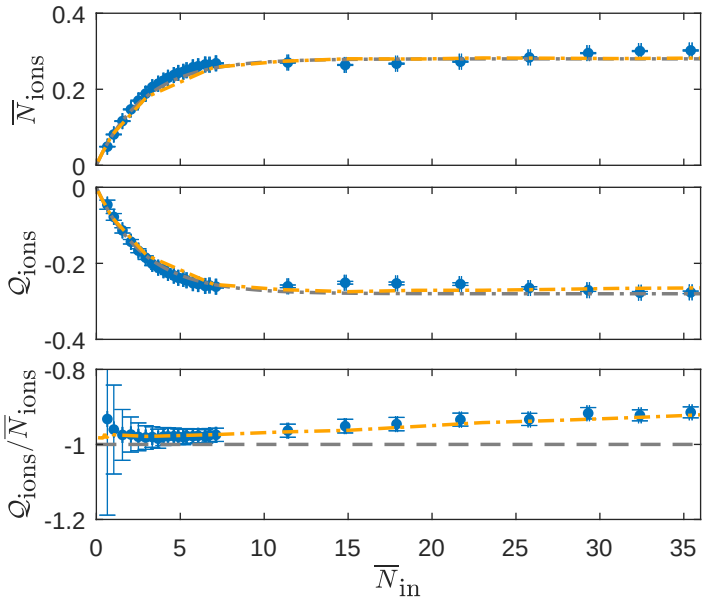

Figure 7.7: **Saturation of excited Rydberg atoms** Full statistics of Rydberg atom detection by field-ionization. Saturation of both the mean ion number at $\overline{N}_{\mathrm{ion}} = 0.28$ and the Mandel-Q parameter at $\mathcal{Q} = -0.28 = -\eta$ for input photon numbers $\overline{N}_{in} > 10$ reveal full blockade of the atomic medium by a single Rydberg excitation. Fitting numerically simulated data (yellow line) to the ratio of Q-parameter and mean ion number allows to determine an the probability $p_{\mathrm{Ryd2}} = 0.001$ to absorb a second photon when the medium is already blockaded.

[152, 146, 156]. In this section the effect of the single-photon absorber is investigated by analyzing the pulse shape and the photon-photon correlations of the output pulse.

Fig. 7.8 shows the shape of input (blue dots) and output pulses (red dots) for $\overline{N}_{in} = 5.65$ (a) and $\overline{N}_{in} = 15.76$ (b), respectively. The pulse shapes of the transmitted probe pulses show a visible distortion as photons are predominantly absorbed in the beginning of the pulse. In particular, for the pulses containing 15.76 photons, the transmission increases to unity in the last third of the pulse, since at these times the probability that one photon has already been absorbed converges to unity. For $\overline{N}_{in} = 5.65$ photons this effect is less dramatic as the probability of all photons being transmitted is still finite ($\sim 14\%$) at this mean input photon number. The numerical simulation (red lines) reproduce the observed pulse shapes quite well. To show that the pulse distortion becomes more severe for higher absorption probabilities, in addition the simulated pulse shapes for the perfect single-photon absorber with $p_{\mathrm{Ryd}} = 1$ and $p_{\mathrm{Ryd2}} = 0$ (black dashed lines) are shown. For these parameters, it is always the first photon in the pulse which is absorbed, resulting in the stronger pulse distortion at the beginning of the pulse. This observation has important consequences for different applications of the single-photon absorption scheme. For efficient number-resolved photon detection by an array of single-photon absorbers, high absorption and strong dephasing are essential [51]. In this case, one has to keep in mind that each photon subtraction results in Fourier-broadening of the pulse, which can reduce the efficiency of subsequent absorbers. In turn, for high-

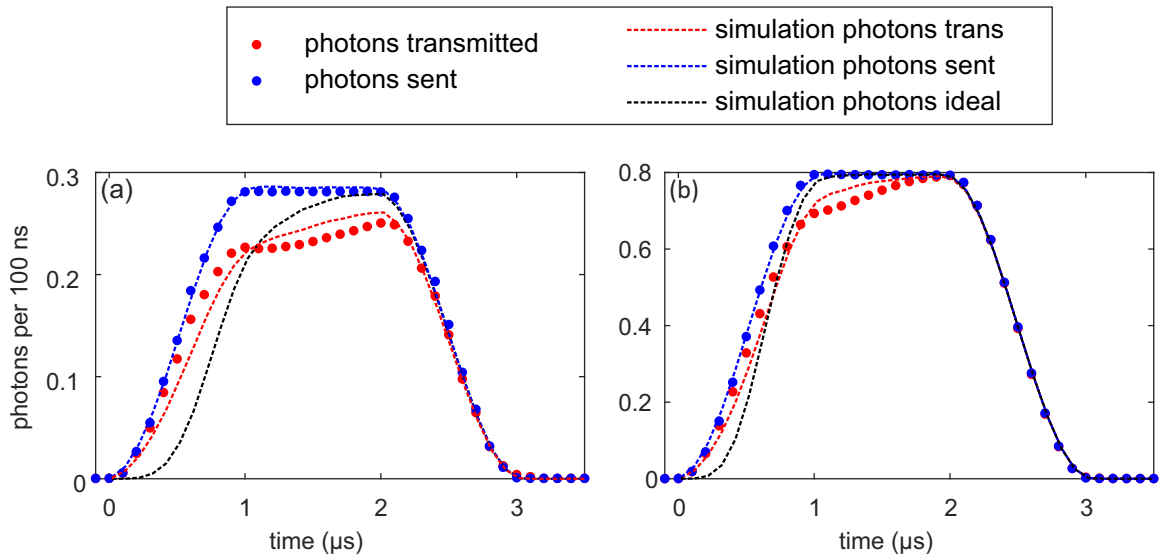

Figure 7.8: **Influence of the absorption on the pulse shape** Measured (points) and simulated (dashed lines) pulse shapes for 5.65 (**a**) and 15.76 (**b**) input photons. The change of the medium from opaque to transparent after the absorption of the first photon leads to a change in the transmitted pulse shape (red points) compared to the pulse sent into the medium (blue points). This effect is captured by our numerical simulation including single- and two-photon absorption probabilities $p_{\mathrm{Ryd}} = 0.35$ and $p_{\mathrm{Ryd2}} = 0.001$ (red line). The pulse distortion is strongest for an ideal deterministic single-photon absorber ($p_{\mathrm{Ryd}} = 1$ and $p_{\mathrm{Ryd2}} = 0$, black line).

fidelity quantum state preparation, the pulse distortion should be minimal. In principle, the absorption in this system is tunable by OD, Δ_c and Ω_c, enabling adapting the single-photon absorption probability such that the total absorption for a given photon number reaches unity, while the information gained about which photon is absorbed is minimal.

Finally, to investigate the photon statistics of the transmitted light, the time dependent intensity correlation function

$$g_2(t_1, t_2) = \frac{\langle n_1(t_1) \cdot n_2(t_2)\rangle}{\langle n_1(t_1)\rangle\langle n_2(t_2)\rangle} \tag{7.9}$$

is calculated for the transmitted probe light. Here, $n_1(t), n_2(t)$ are the numbers of detection on two different detectors at time t. In practice, this intensity correlation is calculated for each possible combination of the four counters used to detect the transmitted photons individually and then the individual results are averaged. The measured intensity correlation for a mean input photon number $\overline{N}_{in} = 15.76$ is shown in Fig. 7.9 (a).

The measurement shows photon bunching, i.e. $g_2(t_1, t_2) > 1$, in the time range where the single-photon absorption happens. As discussed in sec. (7.2) this super-Poissonian statistics results from the fact that the single-photon absorber reduces the mean of the transmitted light by one, but keeps the width of the photon distribution constant. This effect vanishes for the later part of the pulse, where we observe $g_2(t_1, t_2) = 1$, because the saturated medium no longer absorbs photons, resulting in no more modification of

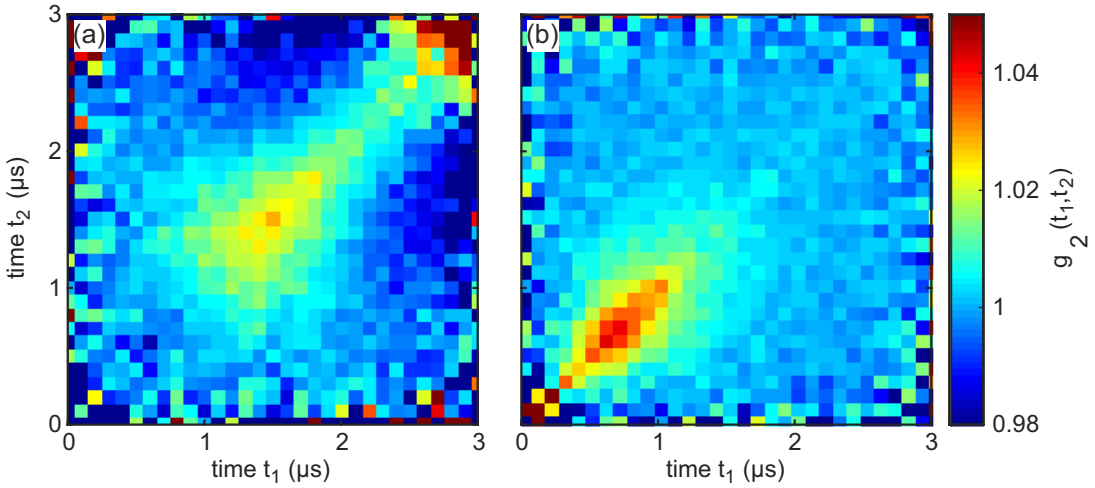

Figure 7.9: **Influence of the absorption on the photon statistics** (**a**) Measured intensity correlation function $g_2(t_1, t_2)$ for mean probe photon input $\overline{N}_{in} = 15.76$. The absorption of a single photon results in photon bunching at the front of the pulse, while the photon statistics during the latter part, where the medium is transparent, are unchanged. (**b**) Simulated correlation functions from the numerical model qualitatively reproduce the features observed in the experimental data, but do not capture the full dynamics of the excitation and dephasing process.

the photon statistics of the coherent input pulse. In Fig. 7.9 (b) the simulated correlation function obtained from the numerical simulation is shown, including the finite single- and two-photon absorption probabilities. The simulation qualitatively reproduces the bunching feature and the change of the correlations over the pulse duration. The most visible difference is the time when the bunching feature appears, which stems from the fact that the numerical simulation neglects any timescale of the initial excitation and dephasing dynamics. A more sophisticated approach, that still yields probe photon statistics, will require calculating the dynamics of the atoms in the presence of a propagating, quantized probe field.

8 Summary and Outlook

Summary

In the scope of this thesis, new experiments investigating the photon-photon interaction in a Rydberg gas have been conducted. To this end, an apparatus has been built facilitating the achievement of huge optical nonlinearities on the level of single photons. The experiment is based on established laser cooling techniques for neutral atoms, enabling the creation of temperatures in the low micro-kelvin regime. Utilization of optical dipole traps offers tunability of size and shape of the atomic medium. Combination of such a dense atomic cloud with coherent excitation techniques like EIT and two-photon Raman transitions, which enable the coupling of highly excited Rydberg states, allows mapping the strong interactions of Rydberg interactions onto naturally non-interacting photons [36, 43, 38, 51].

The first part of the thesis gave a brief introduction to the two mechanisms the experiments are based on: Interactions between pairs of Rydberg atoms and transmission properties of an atomic three-level system driven with two laser fields. Summarizing well-established approaches a detail description of Rydberg-Rydberg interactions including electric fields and angular dependencies has been given. By calculations based on the gathered understanding the importance for nowadays Rydberg experiments was demonstrated. Subsequently, the technique of electromagnetically induced transparency rendering an optically dense sample from opaque to transparent and resulting in extreme reduction of the speed of light was exemplified. The combination of these topics allowed to develop an understanding of the Rydberg excitation blockade and its effect on the photon propagation on EIT resonance.

In the second part, the new experimental results observed during this thesis have been presented. A short description of the apparatus which has been built, including the description of the applied preparation and manipulation techniques for cold atoms, introduced the reader to the measurement techniques. Measurements of the extremely nonlinear transmission through the atomic medium and anti-bunching in the photon statistics of transmitted probe light proved the capability to conduct experiments at the forefront of research investigating strong optical nonlinearities.
The investigation of photons coupled to Rydberg D-states in an EIT scheme allowed to develop new insights on the topic of polariton propagation with angular dependent interactions [49]. Measurements of the time dependent transmissions of probe photons on EIT resonance revealed on the one hand the Rydberg interaction mediated nonlinearity known from Rydberg S-states [41, 37], but on top a decay of transmission over

time occurred. In a series of measurements the dependence of this effect on parameters as probe photon rate, Rabi frequency of the control field and principal quantum number was investigated, pointing out that the decay of transmission is caused by the presence of two-polaritons in the medium. This finding motivated the explanation of the observed effect by interaction induced mixing of degenerate Zeeman spin states, resulting in a decoupling of propagating polaritons from the light field and transforming the polaritons to stationary Rydberg atoms. To model the system in a two-step approach, first dephasing rates depending on both interatomic distance and angle were calculated. Comparing them with the anisotropic Rydberg blockade radius pointed out that in contrast for Rydberg S-states the dephasing for D-states is not negligible outside the Rydberg blockade. Adding the calculated dephasing rates to numerical simulations of the polariton propagation in an three-dimensional medium yielded qualitative agreement with the experiment. These new insights to the polariton propagation in the presence of anisotropic Rydberg interaction are of great importance for all experiments carried out with non-S states [40] or at Förster resonances where multiple levels are coupled. For a more profound understanding it might be interesting to perform storage and retrieval experiments in the future [160, 120]. Especially in a configuration of two traps side by side, this might bring further insights to understand the dynamics of the dephasing and maybe allow to observe revivals on a longer time scale. In such a scenario, it might become interesting to employ echo techniques known from NMR [172] to probe the coherent spin evolution of interacting Rydberg-polaritons.

Reduction of the cloud size by an additional dimple laser allowed to enter a new parameter regime, where the Rydberg interaction only allows for a single Rydberg atom at the time [50]. In this situation, the indistinguishability of the atoms has to be taken into account, as the Rydberg excitation is shared among all N atoms in the medium. This collectivity can by accounted for by a basis transformation to a many-body basis consisting of a collective ground state $|\mathcal{G}\rangle$, one bright state $|\mathcal{W}\rangle$ and $N-1$ dark states $|\mathcal{D}_j\rangle$. Further treatment reveals, that only the $|\mathcal{W}\rangle$ is coupled to the ground state in the presence of a resonant light field, while the dark state are uncoupled. The time coherent time evolution of the many-body system can thus be described by only two states, for this reason such a system is referred to as "superatom". In principle, the driven superatom can undergo coherent dynamics showing Rabi oscillations enhanced by a factor $\sqrt{N}$ due to the collectivity of the excitation. With fast engineered dephasing the Rydberg excitation can however be decoupled from the light field by coupling the bright state to the dark states.
Such decoupling from the light field was achieved in the experiment without introducing further noise to the system. Dephasing rates stemming from motional dephasing due to finite temperature of the atoms, trap induced ac-Stark shifts and molecular broadening turned out to be strong enough for the applied Rabi frequencies. A measurement of the transmitted photon number yielded the absorption of $\Delta\overline{N} = 0.98(13)$ photons averaged over input photon numbers with $\overline{N}_{in} > 10$. This measurement is a clear indication that an absorber saturating after the absorption of a single photon was realized. For input

photon numbers $\overline{N}_{in} < 10$ the absorption is limited by the Poissonian statistics of the light field and the independently determined absorption probability $p_{\mathrm{Ryd}} = 0.35$ for the absorption of a single photon. Measurements of the full Rydberg excitation statistics after each photon pulse by means of Rydberg ionization and ion detection supported this claim. By a numerical Monte-Carlo simulation it was shown, that a weak dependence of the Mandel-Q parameter of the measured Rydberg statistics can be attributed to the probability $p_{\mathrm{Ryd2}} = 0.001$ to subtract excite a second Rydberg atom, when the medium should already be blockaded. From measurements of changes in the pulse shape and in the photon statistics of the transmitted light conclusions on the applicability for high-fidelity number-resolved photon-detection schemes or the preparation of non-classical states of light for applications in quantum information [152, 146, 142, 156, 143] and metrology [147, 151] were drawn.

Outlook

Apart from extensions of the reported experiments, like a cascaded single-photon absorber for the demonstration of a number resolved detector, the apparatus which has been built allows investigate new rich physics based on interacting single photons.

Further optimization of the experimental apparatus resulting in lower temperatures of

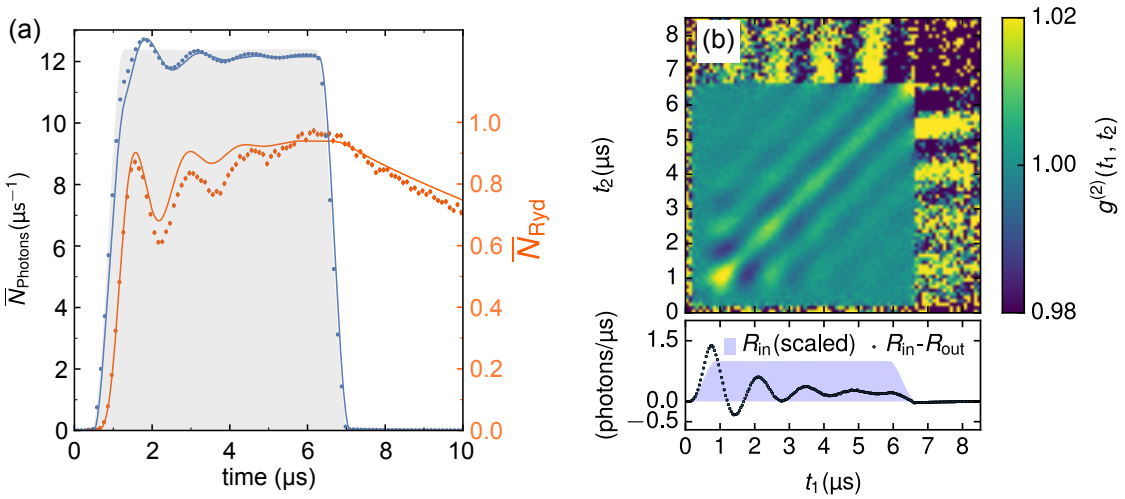

Figure 8.1: **Observation of few photon Rabi oscillations** (**a**) Measurement of the pulse shape of the transmitted photon pulse and the time dependent number of Rydberg atoms inside the medium. Both quantities oscillate with the collective Rabi frequency Ω_{coll}. After the photon pulse has passed the medium, the Rydberg population decays with γ_{Raman}. (**b**) Measured time dependent correlation function of the transmitted probe light (top) and difference of input photon signal and transmitted photon.

the atoms and the usage of a Rydberg state with lower principal quantum number has already allowed to perform new measurements in the small cloud. As a consequence of less motional dephasing of the superatom and lower sensitivity to stray electric fields, the coupling of the bright to the dark states got reduced. Fig. 8.1 (a) shows both the

transmitted photon signal and a time evolution of the number of Rydberg atoms N_{Ryd} inside the atomic cloud. In contrast to the measurements of the single photon absorber presented in chapter 7, both quantities show Rabi-oscillations with the collective Rabi frequency Ω_{coll}. The occurrence of the Rabi oscillations at such low photon number (for the measurements presented here the total photon number was $\overline{N}_{in} = 72.6$) has not been observed up to my knowledge in free-space before. As it can be seen in the lower inset of Fig. 8.1 (b) where the difference of input and output photon number is shown, the Rabi oscillations can even lead to an overshoot of the transmitted photon number. Evaluating the time-dependent intensity correlation function of the transmitted light (top panel of Fig. 8.1 (b)) shows that the rearrangement of photons in the probe pulse also leads to oscillations in the photon statistics of the light. As this measurements are not taken in the EIT regime, where the light is slowed down, the correlations occur among photons which are separated in space by tens to hundreds of meters. This emphasizes the extreme strength of the nonlinearities achievable by mapping Rydberg interactions onto photons.

In the future it might be interesting to investigate complex many-body dynamics by arranging several superatoms on a chain overlapping with the probe beam, such that a coupling of all superatoms occurs.

Another future research direction is rather motivated by the discoveries found by investigating the polariton propagation with D-states. In these experiments already small deviations from the one-dimensional character of the system led to new effects. As a consequence enlarging the probe waist in the experiment to study the propagation of polaritons side by side to each other might open new interesting phenomena. In particular, the impact of strong photon-photon interaction, for both isotropic and anisotropic, on the shape of the transmitted probe beam might allow to discover new phenomena [173]. For such measurements a single-photon sensitive EMCCD camera has already been bought and tested. As illustrated in Fig. 8.2 (a), this camera could replace avalanche single photon counters to measure both spatial and temporal correlation functions (Fig. 8.2 (b)+(c)). Latter one might be especially of interest for investigating many-body phenomena by drastically increasing the number of polaritons in the medium. So far, a bound state consisting of two-photons was already measured [41], in theory also three- and many-photon bound states should exist. Verification of these however requires the measurement of many-photon correlation functions, which in principle requires elaborate optics and expensive photo-detectors. Yet, this camera could be used to measure the demanded temporal correlation functions by illuminating only one row of pixels and subsequently exploiting the frame transfer feature of the camera to reach a high time resolution.

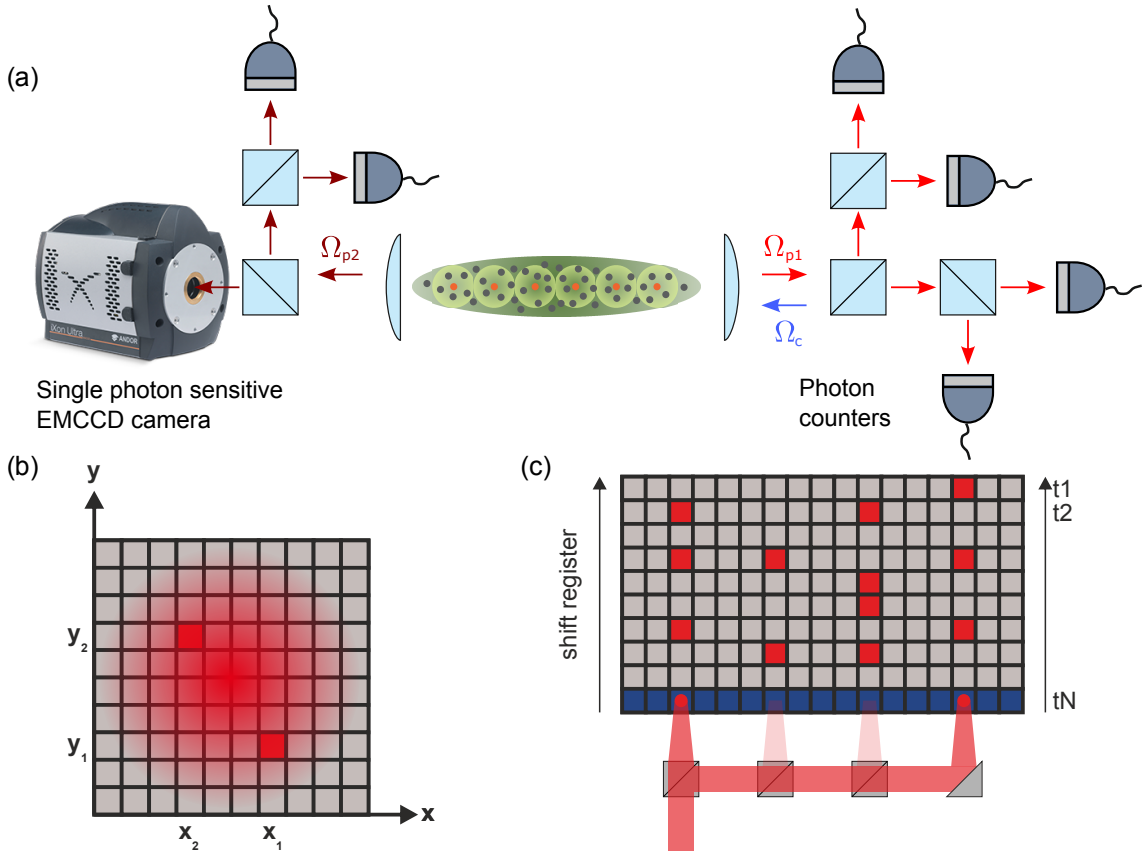

Figure 8.2: **Investigation of spatial and temporal photon correlations** (**a**) Replacement of avalanche single photon counting modules by a single-photon sensitive camera with both spatial and temporal resolution paves the way for future experiments. (**b**) The spatial resolution of the camera allows to measure the beam profile of the transmitted probe beam which can be altered by strong interactions. Additionally it allows to measure spatial correlation functions. (**c**) By exploiting the frame transfer feature of the camera, it could be used instead of multiple single photon counters for fast photon counting and measurements of many-photon correlation functions.

A Apparatus for quantum optics experiments in cold atomic gases

A.1 VACUUM CHAMBER AND LASER BEAMS

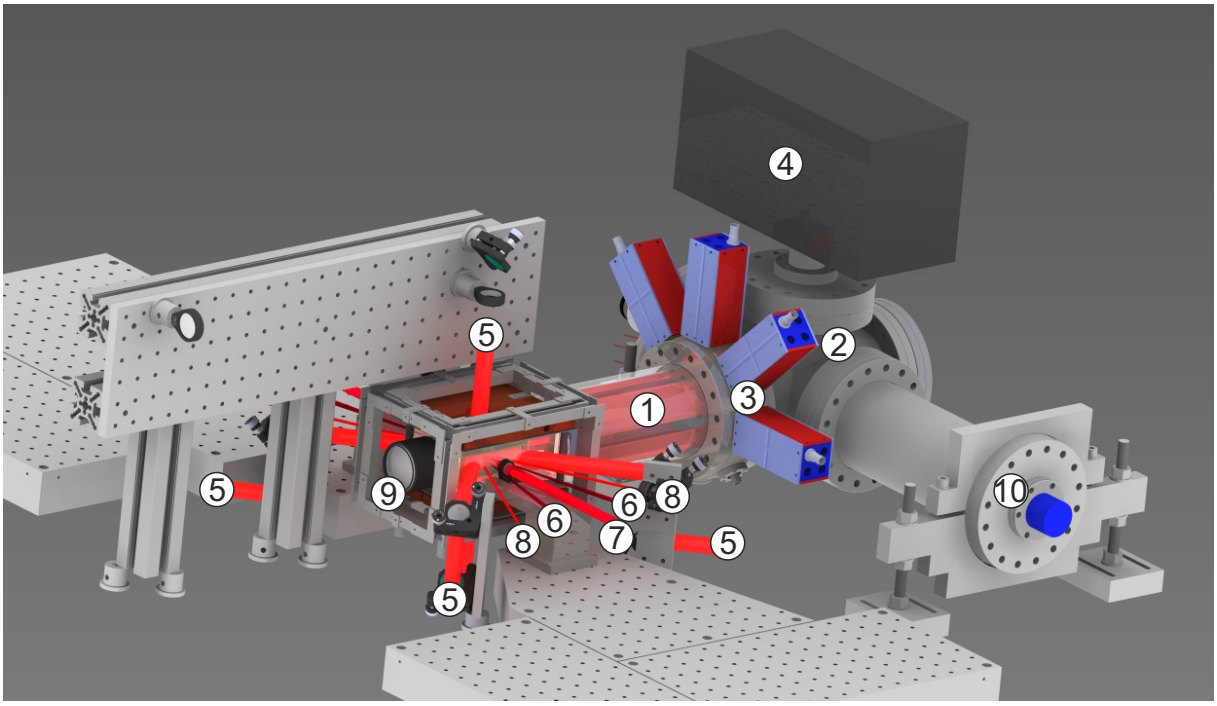

① Glass cell

② Steel chamber

③ Octagon with electrical feedthroughs

④ Ion pump

⑤ Optics for magneto-optical trap

⑥ Crossed optical dipole trap

⑦ Probe/Control beams

⑧ Raman Sideband Cooling Beams

⑨ High resolution imaging lense

⑩ Titanium sublimation pump

Figure A.1: **Apparatus constructed for the experiments** This drawing gives an overview of the setup described in chapter 5

A.2 ELECTRIC FIELD CONTROL AND ION DETECTION

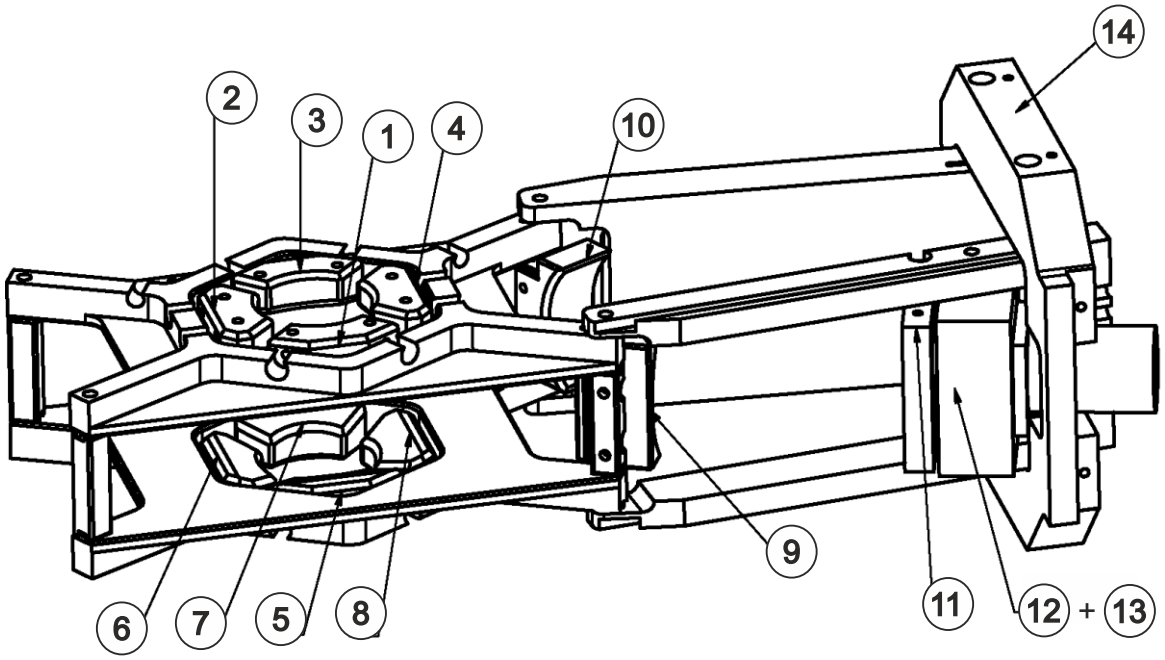

Figure A.2: **Assembly of electric field control and ion detection** This stainless steel construction is used in the experiment to control the electric field at the position of the atomic cloud. The field plates labeled by the numbers 1 to 8 are individually addressable, such that arbitrary electric fields can be generated in the center. For high temporal stability the voltages are provided by a stable voltage source (*Measurement computing MC-USB3100 series*). Additionally, the field plates 2 and 6 can be pulsed to a high voltage of up to 500 V to ionize Rydberg atoms. Fast pulsing is provided by a *CGC NIM-AMX500-3* switch in combination with a *AppliedKilovolts HP0.5PAA025* power supply. After ionization with a positive voltage pulse, ions are flying towards the multichannel (*Hamamatsu F4655-13 MCP*) plate 12+13. For maximum detection efficiency the ions can be guided by applying a steering voltage to the field plates 9+10.

B Rydberg potential calculations

This appendix briefly discusses the steps required to construct the matrix elements the Hamiltonian (3.2) in the interaction potential calculation. To this end, both the energies of the Rydberg levels according to eq. (3.1) and the matrix elements of the single-atom electric multipole operators $\hat{p}_{\kappa q}$ in eq. (3.8) have to be calculated.

B.1 Rydberg energy levels and wave functions

When considering Rydberg atoms with one of their electrons excited to a large principal quantum number $n \gg 1$, the atoms behave very similar to a hydrogen atom, as the $Z-1$ inner electrons screen the charge Z of the nucleus such that the Rydberg electron effectively moves in a slightly modified Coulomb potential. Reduction of the problem to the single Rydberg electron is in particular valid for Alkali atoms, where the inner electrons form closed shells, but also justified for other atomic species, such as the noble gases [174], the alkaline earth metals [175], and even the lanthanides [176] if the principal quantum number n is large enough.

B.1.1 *Rydberg energies*

This treatment results in the expression

$$E_{nLJ} = -\frac{hcR^*}{n^{*2}}, \tag{B.1}$$

for the binding energy of the Rydberg series, in total analogy to the hydrogen atom. The term

$$R^* = \frac{1}{1 + m_e/M_{\text{atom}}} R_\infty \tag{B.2}$$

is a modified Rydberg constant, taking into account the species dependent mass M_{atom} of the atomic core. On top, species-dependent deviations from the hydrogen atom are taken into account by the effective, non-integer principal quantum number n^*. The corresponding values can be obtained from the main principal quantum number n by introducing the species-dependent quantum defects δ_{nLJ}, which are written in a series expansion of the form

$$\delta_{nlj} = \delta_0 + \frac{\delta_2}{(n-\delta_0)^2} + \frac{\delta_4}{(n-\delta_0)^4} + \frac{\delta_6}{(n-\delta_0)^6} + \cdots . \tag{B.3}$$

The coefficients in this polynomial expression are obtained from fits to experimentally measured transition energies for specific species. The fine-structure splitting is usually included in the quantum defects, resulting in the dependence on the quantum number J. The quantum defects decrease rapidly with increasing orbital angular momentum L, since for high-L states the electron is localized further out such that the influence of the non-hydrogenic core becomes less relevant. As a consequence, for $L > 3$ the energies of the levels follows the analytic expression known form Hydrogen

$$E_{nLJ} = -\frac{hcR^*}{n^2}\left(1 + \frac{\alpha^2}{n(J+1/2)} + \frac{\alpha^2}{n^2}\right) - \frac{e^2}{(4\pi\varepsilon_0)^2 a_0^4}\frac{3\alpha_d}{4n^3L^5}, \tag{B.4}$$

including a correction term proportional to the core species-dependent polarizability α_d [106].

B.1.2 *Rydberg electron wave function*

Having found the energies required for the Hamiltonian (3.2), the missing quantities are the matrix elements of the single-atom electric multipole operators $\hat{p}_{\kappa q}$ in eq. (3.8). Their calculation requires the wave functions of the single electron orbiting around the screened nucleus. Even though the core potential becomes more complicated for non-hydrogenic atom, the spherical symmetry of the problem is conserved, such that the separation of the wave function

$$\psi(r, \vartheta, \varphi) = R_{nLJ}(r) \cdot Y_{LSJm_J}(\vartheta, \varphi), \tag{B.5}$$

into a radial part $R_{nLJ}(r)$ and an angular part $Y_{LSJm_J}(\vartheta, \varphi)$ justified. Including the fine-structure, the analytic expression of the spin spherical harmonics is [77]

$$Y_{J\pm\frac{1}{2},\frac{1}{2},j,m_J} = \frac{1}{\sqrt{2\left(J \pm \frac{1}{2}\right)+1}} \begin{pmatrix} \mp\sqrt{J \pm \frac{1}{2} \mp m_J + \frac{1}{2}}\, Y_{J\pm\frac{1}{2},m_J-\frac{1}{2}} \\ \sqrt{J \pm \frac{1}{2} \pm m_J + \frac{1}{2}}\, Y_{J\pm\frac{1}{2},m_J+\frac{1}{2}} \end{pmatrix}. \tag{B.6}$$

Based on this expression, the angular part of the electric multipole moments can be calculated analytically, including the usual multipole selection rules, discussed in detail in B.3.

For the radial part R_{nLJ} non-relativistic quantum defect theory provides analytical solutions, known as *Coulomb functions* [177, 61]. The basic idea is to consider large distances r from the nucleus, where the screening of the inner electrons results in an effective core charge $Z = 1$. There, the radial Schrödinger equation reduces to the well-known hydrogen case, except that the energy eigenvalues of the bound states are fixed

via the experimentally determined quantum defects. As a consequence, the resulting solutions depend on the (non-integer) effective principal quantum number n^*:

$$R_{n^*LJ}(r) = \left(\frac{1}{a_0}\right)^{3/2} \frac{1}{\sqrt{(n^*)^2\Gamma(n^*+L+1)\Gamma(n^*-L)}} W_{n^*,L+1/2}\left(\frac{2r}{n^* a_0}\right). \tag{B.7}$$

Here, $\Gamma(z)$ is the Gamma function, and $W_{k,m}(z)$ the Whittaker function. The Coulomb functions are obtained by solving the hydrogen Coulomb radial equation where the energies corresponding to non-integer principal quantum numbers have already been inserted. These are approximate wave functions with the correct behavior for large r and the right binding energy. For the calculation of transition matrix elements between Rydberg states, these are the important criteria. A relativistic generalization of the quantum-defect theory exists [178], but for the high-n Rydberg states of interest here, the modification of the radial wave function due to the fine-structure correction turns out to be negligible.

An alternative approach to obtaining single-electron wave functions is numerically solving the radial Schrödinger equation including a species-dependent *model potential* [179]. Compared to quantum-defect theory this approach enables calculation of wave functions in the inner region, if the model potentials were correctly determined. Typically, the model potential contains three contributions:

$$V_{\mathrm{mod}}(r) = V_{\mathrm{C}}(r) + V_{\mathrm{P}}(r) + V_{\mathrm{s.o.}}(r). \tag{B.8}$$

Here,

$$V_{\mathrm{C}}(r) = -\frac{e^2}{4\pi\varepsilon_0}\frac{1+(Z-1)\mathrm{e}^{-\alpha_1 r} - r(\alpha_3+\alpha_4 r)\mathrm{e}^{-\alpha_2 r}}{r}, \tag{B.9}$$

is a modified Coulomb potential describing the distance dependent screening of the nucleus charge by the inner electrons [180]. The coefficients $\alpha_{1,2,3,4}$ depend on the atomic species and the orbital angular momentum L [180].

$$V_{\mathrm{P}}(r) = -\frac{e^2}{(4\pi\varepsilon_0)^2}\frac{\alpha_d}{2r^4}\left[1-\mathrm{e}^{-(r/r_c)^6}\right] \tag{B.10}$$

describes the core polarizability as a consequence of the deformation of the core charge distribution by the Rydberg electron. Here, α_d is the core dipole polarizability (higher terms can also be included [179]) and r_c is the effective core size, obtained by comparing the numerical solutions with the experimentally observed energy levels. Finally,

$$V_{\mathrm{s.o.}}(r > r_c) = \frac{1}{2}\left(\frac{e^2}{4\pi\varepsilon_0}\right)\left(\frac{g_s}{2m_e^2c^2}\right)\frac{\boldsymbol{L}\cdot\boldsymbol{S}}{r^3}. \tag{B.11}$$

adds the spin-orbit coupling [181]. This expression is only valid for large r and for smaller distances from the core the full expression derived from the Dirac equation has to be taken into account [179].

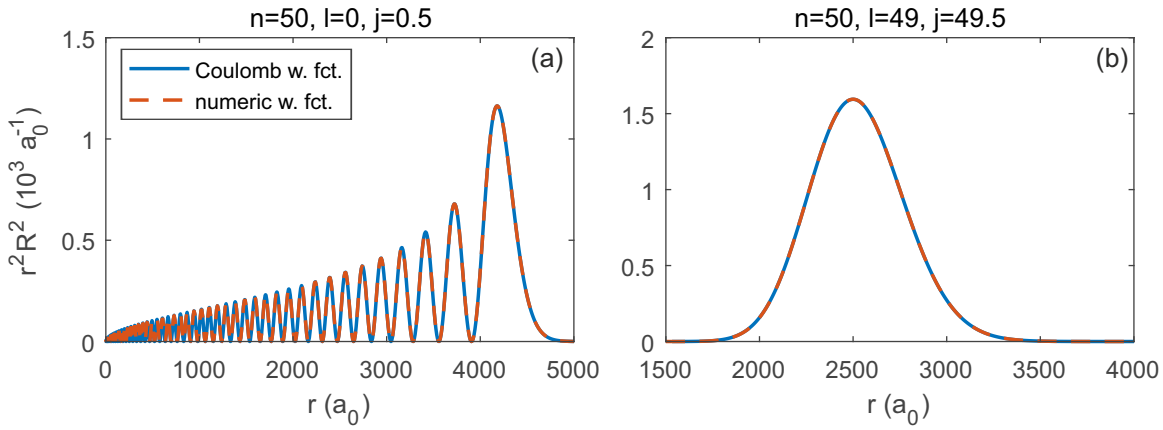

Figure B.1: Comparison of radial Rydberg wave functions obtained via numerical integration of the Schrödinger equation including the model potential (B.8) (dashed red line) and the corresponding Coulomb wave functions (B.7) (blue line). The different results agree very well, however the calculation of the numerical wave functions requires much less computation time.

The spin-orbit interaction V_{so} depends on the radial coordinate r, thus the numerical radial wave function depends on the total angular momentum j. In practice, one usually does not solve the radial Schrödinger equation as eigenvalue problem, but instead inserts the level energies determined from experimental quantum defects (B.4). Here, care must be taken when combining model potentials (e.g. from [180]) with independently measured quantum defects, since the inserted energies most likely are not eigenenergies of the model potential. Improvements to the model potentials including the fine structure term have recently been discussed by Sanayei *et al.* [182].

Fig. B.1 compares wave functions derived via numerical integration and the corresponding Coulomb wave functions. The analytic Coulomb wave functions only indirectly include spin-orbit coupling and the modifications of the Coulomb potential from the simple hydrogen case via the quantum defects, while the model potential explicitly includes these effects in the Hamiltonian. For large n, and even more for large L, the overlap of the Rydberg electron with the core region is vanishingly small, making the Coulomb functions very accurate solutions. However, the numerical integration has the advantage, that state of the art numerical methods provide fast solving routines for the differential equation. On the other hand, the Whittaker functions are usually expressed in terms of hypergeometric functions and thus have to be evaluated by converging a power series, which is computationally intense.

B.2 RADIAL MATRIX ELEMENTS

Calculating the radial parts of the electric multipole matrix elements appearing in the interaction Hamiltonian ((3.7) in sec. (3.2)) amounts to solving integrals of the form

$$\langle nLJ|\hat{p}_\kappa^{\mathrm{rad}}|n'L'J'\rangle = \int R_{nLJ}(r)R_{n'L'J'}(r)r^{2+\kappa}\,dr, \tag{B.12}$$

where $R_{nLJ}(r)$ are the radial wave functions discussed in B.1, obtained either numerically or in the form of Coulomb functions (B.7), and κ is the order of the multipole operator (3.8) in sec. (3.2). Note, that the radial wave functions obtained by either approach are real, so that the complex conjugation in the matrix element can be omitted. The matrix elements can be straightforwardly calculated by numerical integration [177, 183]. To optimize the numerics, it is useful to rescale the radial coordinate and the wave functions according to

$$x = \sqrt{r}\ , \quad X^{\mathrm{rad}}_{nLJ}(x) = x^{3/2} R_{nLJ}(r). \tag{B.13}$$

This scaling keeps the number of grid points between nodes of the wave function constant [184]. As an alternative to numerical integration, various analytical expressions for electric dipole matrix elements exist [184, 185, 186]. In Fig. B.2, electric dipole matrix elements obtained from numerical integration either using Coulomb functions or model potential wave functions and evaluation of the analytical expression in [186] are compared. For transitions between low-L states the three approaches produce remarkable agreement for $n > 40$. For high-L transitions there are systematic deviations between the results of the model potential and the other two approaches, but the relative difference remains smaller than 1%.

It is important to note that the rather simple methods of calculating single-electron wave functions only yield accurate results for $n > 30$. Significantly more advanced methods for calculating energy levels and matrix elements than the ones presented here have been developed for low-n states, see e.g. [187, 188].

B.3 ANGULAR MATRIX ELEMENTS

In addition to the radial part discussed in B.2, the angular part of the electric multipole matrix elements is needed to construct the Hamiltonian (3.2). This appendix reviews the general formalism to calculating matrix elements of spherical tensor operators, which can be applied to determining the angular parts appearing when the multipole operators are expressed in the spherical basis [189]. The formalism relies on the Wigner-Eckart theorem [81], which states that matrix elements of spherical tensor operators $\hat{T}_{\kappa q}$ can be expressed as products of Wigner 3-j symbols and a reduced matrix element, which is independent of the angular momentum orientation. When the calculations are preformed in the fine-structure basis, the Wigner-Eckart theorem for the total angular momentum $J = L + S$ reads

$$\langle LSJm_J|\hat{T}_{\kappa q}|L'S'J'm'_J\rangle = (-1)^{J-m_J}(LSJ||\hat{T}_{\kappa 0}||L'S'J') \begin{pmatrix} J & \kappa & J' \\ -m_J & q & m'_J \end{pmatrix}\ , \tag{B.14}$$

where $(LSJ||\hat{T}_{\kappa 0}||L'S'J')$ is the reduced matrix element for the total angular momentum. In particular, the spherical tensor operators required for the matrix elements of the $\hat{p}_{\kappa q}$ (eq. (3.8)) are the spin-spherical harmonics $\hat{Y}_{\kappa q}(\hat{\vartheta}, \hat{\varphi})$, commuting with the electron spin

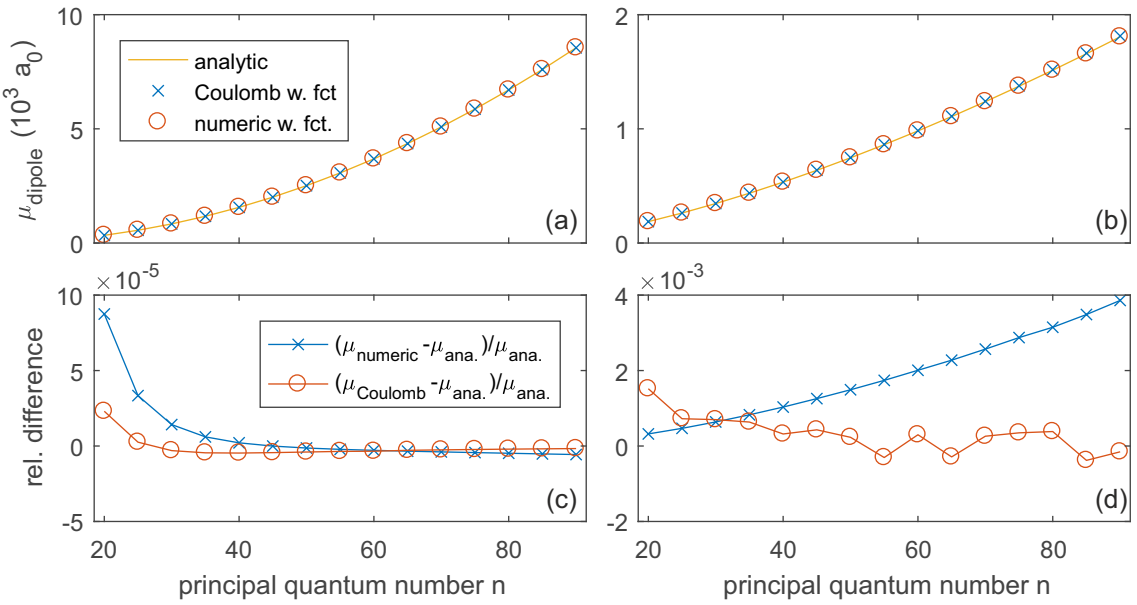

Figure B.2: Comparison of dipole matrix elements calculated by numeric integration using either Coulomb functions or model potential wave functions with the analytic expression from [186]. (**a**)+(**c**) show dipole matrix elements for the $n, L = 0, J = 1/2 \leftrightarrow n' = n, L' = 1, J' = 3/2$ transition and the relative difference between the three different approaches. All three methods are in very good agreement for the Rydberg states of interest here. (**b**)+(**d**) show dipole matrix elements for transitions from $n, L = n-1, J = L+1/2 \leftrightarrow n' = n, L' = n-2, J' = L'+1/2$ calculated for different principle quantum numbers and their relative difference. For transitions between high-L states a more significant systematic deviation between the result based on model potential wave functions and the other two approaches can be observed.

S. In this case, different reduced matrix elements can than be related via the expression

$$(LSJ||\hat{Y}_{\kappa 0}||L'SJ') = (-1)^{L+S+J'+\kappa}(L||\hat{Y}_{\kappa 0}||L')\sqrt{(2J+1)(2J'+1)}\begin{Bmatrix} L & J & S \\ J' & L' & \kappa \end{Bmatrix}, \tag{B.15}$$

where the last term is the Wigner 6-j symbol. The value of the relevant reduced matrix element is

$$(L||\hat{Y}_{\kappa 0}||L') = (-1)^{L}\sqrt{\frac{(2L+1)(2\kappa+1)(2L'+1)}{4\pi}}\begin{pmatrix} L & \kappa & L' \\ 0 & 0 & 0 \end{pmatrix}. \tag{B.16}$$

Bibliography

[1] H. J. Caulfield and Shlomi Dolev. "Why future supercomputing requires optics." In: *Nature Photonics* 4.5 (2010), pp. 261–263. DOI: 10.1038/nphoton.2010.94 (cit. on pp. 1, 5).

[2] Alain Aspect, Jean Dalibard, and Gérard Roger. "Experimental Test of Bell's Inequalities Using Time- Varying Analyzers." In: *Phys. Rev. Lett.* 49 (25 Dec. 1982), pp. 1804–1807. DOI: 10.1103/PhysRevLett.49.1804 (cit. on pp. 1, 5).

[3] Z. Y. Ou and L. Mandel. "Violation of Bell's Inequality and Classical Probability in a Two-Photon Correlation Experiment." In: *Phys. Rev. Lett.* 61 (1 July 1988), pp. 50–53. DOI: 10.1103/PhysRevLett.61.50 (cit. on pp. 1, 5).

[4] Michael A. Nielsen and Isaac L. Chuang. *Quantum Computation and Quantum Information: 10th Anniversary Edition*. Cambridge: Cambridge University Press, Dec. 2010. ISBN: 9780511976667. DOI: 10.1017/CBO9780511976667 (cit. on pp. 1, 5).

[5] Richard P. Feynman. "Simulating physics with computers." In: *International Journal of Theoretical Physics* 21.6 (1982), pp. 467–488. ISSN: 1572-9575. DOI: 10.1007/BF02650179 (cit. on pp. 1, 5).

[6] P. A. Franken, A. E. Hill, C. W. Peters, and G. Weinreich. "Generation of Optical Harmonics." In: *Phys. Rev. Lett.* 7 (4 Aug. 1961), pp. 118–119. DOI: 10.1103/PhysRevLett.7.118 (cit. on pp. 1, 5).

[7] Quan Sheng et al. "A continuous-wave tunable orange-red source based on sum-frequency generation in an intra-cavity periodically poled LiNbO 3 singly resonant optical parametric oscillator cavity." In: *Journal of Optics* 13.9 (2011), p. 095201 (cit. on pp. 1, 5).

[8] G. Zumofen, N. M. Mojarad, V. Sandoghdar, and M. Agio. "Perfect Reflection of Light by an Oscillating Dipole." In: *Phys. Rev. Lett.* 101 (18 Oct. 2008), p. 180404. DOI: 10.1103/PhysRevLett.101.180404 (cit. on pp. 1, 5).

[9] Syed Abdullah Aljunid et al. "Excitation of a Single Atom with Exponentially Rising Light Pulses." In: *Phys. Rev. Lett.* 111 (10 Sept. 2013), p. 103001. DOI: 10.1103/PhysRevLett.111.103001 (cit. on pp. 1, 5).

[10] L. Hau, S.E. Harris, Z. Dutton, and C. H. Behroozi. "Light speed reduction to 17 metres per second in an ultracold atomic gas." In: *Nature* 397 (6720 1999), pp. 594–598. DOI: 10.1038/17561 (cit. on pp. 1, 5, 39).

[11] K.-J. Boller, A. Imamo ğlu, and S. E. Harris. "Observation of electromagnetically induced transparency." In: *Phys. Rev. Lett.* 66 (20 May 1991), pp. 2593–2596. DOI: 10.1103/PhysRevLett.66.2593 (cit. on pp. 1, 5, 38).

[12] M. Fleischhauer and M. D. Lukin. "Dark-State Polaritons in Electromagnetically Induced Transparency." In: *Phys. Rev. Lett.* 84 (2000), pp. 5094–5097 (cit. on pp. 1, 3, 5, 6, 8, 40, 81).

[13] S. E. Harris and Lene Vestergaard Hau. "Nonlinear Optics at Low Light Levels." In: *Phys. Rev. Lett.* 82 (23 June 1999), pp. 4611–4614. DOI: 10.1103/PhysRevLett.82.4611 (cit. on pp. 1, 5).

[14] Zi-Yu Liu et al. "Large Cross-Phase Modulations at the Few-Photon Level." In: *Phys. Rev. Lett.* 117 (20 Nov. 2016), p. 203601. DOI: 10.1103/PhysRevLett.117.203601 (cit. on pp. 2, 5).

[15] R. J. Thompson, G. Rempe, and H. J. Kimble. "Observation of normal-mode splitting for an atom in an optical cavity." In: *Phys. Rev. Lett.* 68 (8 Feb. 1992), pp. 1132–1135. DOI: 10.1103/PhysRevLett.68.1132 (cit. on pp. 2, 5, 84).

[16] B. Weber et al. "Photon-Photon Entanglement with a Single Trapped Atom." In: *Phys. Rev. Lett.* 102 (3 Jan. 2009), p. 030501. DOI: 10.1103/PhysRevLett.102.030501 (cit. on pp. 2, 5).

[17] Wenlan Chen et al. "All-Optical Switch and Transistor Gated by One Stored Photon." In: *Science* (2013). ISSN: 0036-8075. DOI: 10.1126/science.1238169. eprint: http://science.sciencemag.org/content/early/2013/07/03/science.1238169.full.pdf (cit. on pp. 2, 5).

[18] Kristin M. Beck, Mahdi Hosseini, Yiheng Duan, and Vladan Vuletić. "Large conditional single-photon cross-phase modulation." In: *Proceedings of the National Academy of Sciences* 113.35 (2016), pp. 9740–9744. DOI: 10.1073/pnas.1524117113. eprint: http://www.pnas.org/content/113/35/9740.full.pdf (cit. on pp. 2, 5).

[19] J. Balewski et al. "Coupling a single electron to a Bose-Einstein condensate." In: *Nature* 502 (2013), pp. 664–667. DOI: doi:10.1038/nature12592 (cit. on pp. 2, 6, 49).

[20] Jia Wang, Marko Gacesa, and R. Côté. "Rydberg Electrons in a Bose-Einstein Condensate." In: *Phys. Rev. Lett.* 114 (24 June 2015), p. 243003. DOI: 10.1103/PhysRevLett.114.243003 (cit. on pp. 2, 6).

[21] D. Jaksch et al. "Fast Quantum Gates for Neutral Atoms." In: *Phys. Rev. Lett.* 85 (10 Sept. 2000), pp. 2208–2211. DOI: 10.1103/PhysRevLett.85.2208 (cit. on pp. 2, 6, 43).

[22] L. Isenhower et al. "Demonstration of a Neutral Atom Controlled-NOT Quantum Gate." In: *Phys. Rev. Lett.* 104 (1 Jan. 2010), p. 010503. DOI: 10.1103/PhysRevLett.104.010503 (cit. on pp. 2, 6, 43).

[23] Hendrik Weimer, Robert Löw, Tilman Pfau, and Hans Peter Büchler. "Quantum Critical Behavior in Strongly Interacting Rydberg Gases." In: *Phys. Rev. Lett.* 101 (25 Dec. 2008), p. 250601. DOI: 10.1103/PhysRevLett.101.250601 (cit. on pp. 2, 6).

[24] P. Schauß et al. "Crystallization in Ising quantum magnets." In: *Science* 347.6229 (2015), pp. 1455–1458. ISSN: 0036-8075. DOI: 10.1126/science.1258351. eprint: http://science.sciencemag.org/content/347/6229/1455.full.pdf (cit. on pp. 2, 6).

[25] M. D. Lukin et al. "Dipole Blockade and Quantum Information Processing in Mesoscopic Atomic Ensembles." In: *Phys. Rev. Lett.* 87 (2001), p. 037901. DOI: 10.1103/PhysRevLett.87.037901 (cit. on pp. 2, 6, 42).

[26] J M Raimond, G Vitrant, and S Haroche. "Spectral line broadening due to the interaction between very excited atoms: 'the dense Rydberg gas'." In: *Journal of Physics B: Atomic and Molecular Physics* 14.21 (1981), p. L655 (cit. on pp. 2, 6).

[27] E. L. Raab, M. Prentiss, Alex Cable, Steven Chu, and D. E. Pritchard. "Trapping of Neutral Sodium Atoms with Radiation Pressure." In: *Phys. Rev. Lett.* 59 (23 Dec. 1987), pp. 2631–2634. DOI: 10.1103/PhysRevLett.59.2631 (cit. on pp. 2, 6).

[28] M. H. Anderson, J. R. Ensher, M. R. Matthews, C. E. Wieman, and E. A. Cornell. "Observation of Bose-Einstein Condensation in a Dilute Atomic Vapor." In: *Science* 269.5221 (1995), pp. 198–201. ISSN: 0036-8075. DOI: 10.1126/science.269.5221.198. eprint: http://science.sciencemag.org/content/269/5221/198.full.pdf (cit. on pp. 2, 6, 55).

[29] E. Urban et al. "Observation of Rydberg blockade between two atoms." In: *Nature Phys.* 5 (2009), pp. 110–114. DOI: doi:10.1038/nphys1178 (cit. on pp. 2, 6, 8, 84, 86).

[30] A. Gaëtan et al. "Observation of collective excitation of two individual atoms in the Rydberg blockade regime." In: *Nature Phys.* 5 (2009), pp. 115–118. DOI: doi:10.1038/nphys1183 (cit. on pp. 2, 6, 8, 84, 86).

[31] Kilian Singer, Jovica Stanojevic, Matthias Weidemüller, and Robin Côté. "Long-range interactions between alkali Rydberg atom pairs correlated to the n s– n s, n p– n p and n d– n d asymptotes." In: *Journal of Physics B: Atomic, Molecular and Optical Physics* 38.2 (2005), S295 (cit. on pp. 2, 6, 15, 17, 76).

[32] I. I. Ryabtsev, D. B. Tretyakov, I. I. Beterov, and V. M. Entin. "Observation of the Stark-Tuned Förster Resonance between Two Rydberg Atoms." In: *Phys. Rev. Lett.* 104 (2010), p. 073003. DOI: 10.1103/PhysRevLett.104.073003 (cit. on pp. 2, 6).

[33] J. Nipper et al. "Highly Resolved Measurements of Stark-Tuned Förster Resonances between Rydberg Atoms." In: *Phys. Rev. Lett.* 108 (11 Mar. 2012), p. 113001. DOI: 10.1103/PhysRevLett.108.113001 (cit. on pp. 2, 6, 67).

[34] P. Schauss et al. “Observation of spatially ordered structures in a two-dimensional Rydberg gas.” In: *Nature* 491 (2012), p. 87. DOI: doi:10.1038/nature11596 (cit. on pp. 2, 6).

[35] Hendrik Weimer, Markus Mueller, Igor Lesanovsky, Peter Zoller, and Hans Peter Büchler. “A Rydberg quantum simulator.” In: *Nature Phys.* 6 (2010), pp. 382–388. DOI: doi:10.1038/nphys1614 (cit. on pp. 2, 6).

[36] I. Friedler, D. Petrosyan, M. Fleischhauer, and G. Kurizki. “Long-range interactions and entanglement of slow single-photon pulses.” In: *Phys. Rev. A* 72 (2005), p. 043803. DOI: 10.1103/PhysRevA.72.043803 (cit. on pp. 3, 6, 44, 101).

[37] J. D. Pritchard et al. “Cooperative Atom-Light Interaction in a Blockaded Rydberg Ensemble.” In: *Phys. Rev. Lett.* 105 (2010), p. 193603. DOI: 10.1103/PhysRevLett.105.193603 (cit. on pp. 3, 4, 6, 63, 69, 71, 80, 83, 101).

[38] T. Peyronel et al. “Quantum nonlinear optics with single photons enabled by strongly interacting atoms.” In: *Nature* 488 (2012), pp. 57–60. DOI: 10.1038/nature11361 (cit. on pp. 3, 6, 44, 69, 71, 79–81, 83, 101).

[39] Y. O. Dudin and A. Kuzmich. “Strongly Interacting Rydberg Excitations of a Cold Atomic Gas.” In: *Science* 336 (2012), pp. 887–889. DOI: 10.1126/science.1217901 (cit. on pp. 3, 6, 69, 71, 83).

[40] D. Maxwell et al. “Storage and Control of Optical Photons Using Rydberg Polaritons.” In: *Phys. Rev. Lett.* 110 (10 Mar. 2013), p. 103001. DOI: 10.1103/PhysRevLett.110.103001 (cit. on pp. 3, 6, 102).

[41] O. Firstenberg et al. “Attractive photons in a quantum nonlinear medium.” In: *Nature* 502 (2013), pp. 71–75. DOI: doi:10.1038/nature12512 (cit. on pp. 3, 4, 6, 44, 79, 81, 83, 101, 104).

[42] Daniel Tiarks, Steffen Schmidt, Gerhard Rempe, and Stephan Dürr. “Optical π phase shift created with a single-photon pulse.” In: *Science Advances* 2 (2016), e1600036. DOI: http://dx.doi.org/10.1126/sciadv.1600036 (cit. on pp. 3, 6, 44, 83).

[43] Alexey V. Gorshkov, Johannes Otterbach, Michael Fleischhauer, Thomas Pohl, and Mikhail D. Lukin. “Photon-Photon Interactions via Rydberg Blockade.” In: *Phys. Rev. Lett.* 107 (13 Sept. 2011), p. 133602. DOI: 10.1103/PhysRevLett.107.133602 (cit. on pp. 3, 6, 44, 101).

[44] Krzysztof Jachymski, Przemysław Bienias, and Hans Peter Büchler. “Three-Body Interaction of Rydberg Slow-Light Polaritons.” In: *Phys. Rev. Lett.* 117 (5 July 2016), p. 053601. DOI: 10.1103/PhysRevLett.117.053601 (cit. on pp. 3, 6, 72).

[45] M. J. Gullans et al. “Effective Field Theory for Rydberg Polaritons.” In: *Phys. Rev. Lett.* 117 (11 Sept. 2016), p. 113601. DOI: 10.1103/PhysRevLett.117.113601 (cit. on pp. 3, 6).

[46] Johannes Otterbach, Matthias Moos, Dominik Muth, and Michael Fleischhauer. "Wigner Crystallization of Single Photons in Cold Rydberg Ensembles." In: *Phys. Rev. Lett.* 111 (11 Sept. 2013), p. 113001. DOI: 10.1103/PhysRevLett.111.113001 (cit. on pp. 3, 7).

[47] H. Gorniaczyk, C. Tresp, J. Schmidt, H. Fedder, and S. Hofferberth. "Single-Photon Transistor Mediated by Interstate Rydberg Interactions." In: *Phys. Rev. Lett.* 113 (5 July 2014), p. 053601. DOI: 10.1103/PhysRevLett.113.053601 (cit. on pp. 3, 8, 63, 71, 83).

[48] H. Gorniaczyk et al. "Enhancement of Rydberg-mediated single-photon nonlinearities by electrically tuned Förster resonances." In: *Nature Communications* 7 (2016), p. 12480. DOI: doi:10.1038/ncomms12480 (cit. on pp. 3, 8, 63, 66, 79, 83).

[49] C. Tresp et al. "Dipolar Dephasing of Rydberg D-State Polaritons." In: *Phys. Rev. Lett.* 115 (8 Aug. 2015), p. 083602. DOI: 10.1103/PhysRevLett.115.083602 (cit. on pp. 4, 67, 101).

[50] C. Tresp et al. "Single-Photon Absorber Based on Strongly Interacting Rydberg Atoms." In: *Phys. Rev. Lett.* 117 (22 Nov. 2016), p. 223001. DOI: 10.1103/PhysRevLett.117.223001 (cit. on pp. 4, 83, 102).

[51] Jens Honer, Robert Löw, Hendrik Weimer, Tilman Pfau, and Hans Peter Büchler. "Artificial Atoms Can Do More Than Atoms: Deterministic Single Photon Subtraction from Arbitrary Light Fields." In: *Phys. Rev. Lett.* 107 (9 Aug. 2011), p. 093601. DOI: 10.1103/PhysRevLett.107.093601 (cit. on pp. 4, 8, 41, 83, 85, 87, 95, 98, 101).

[52] T. M. Weber et al. "Mesoscopic Rydberg-blockaded ensembles in the superatom regime and beyond." In: *Nature Physics* 11 (2015), pp. 157–161. DOI: doi:10.1038/nphys3214 (cit. on pp. 6, 8).

[53] Johannes Zeiher et al. "Microscopic Characterization of Scalable Coherent Rydberg Superatoms." In: *Phys. Rev. X* 5 (3 Aug. 2015), p. 031015. DOI: 10.1103/PhysRevX.5.031015 (cit. on pp. 6, 8, 86).

[54] Daniel Tiarks, Simon Baur, Katharina Schneider, Stephan Dürr, and Gerhard Rempe. "Single-Photon Transistor Using a Förster Resonance." In: *Phys. Rev. Lett.* 113 (5 July 2014), p. 053602. DOI: 10.1103/PhysRevLett.113.053602 (cit. on pp. 8, 63, 66, 71, 83).

[55] D. Barredo et al. "Demonstration of a Strong Rydberg Blockade in Three-Atom Systems with Anisotropic Interactions." In: *Phys. Rev. Lett.* 112 (18 May 2014), p. 183002. DOI: 10.1103/PhysRevLett.112.183002 (cit. on pp. 8, 67, 77).

[56] Henning Labuhn et al. "Tunable two-dimensional arrays of single Rydberg atoms for realizing quantum Ising models." In: *Nature* 534 (2016), pp. 667–670. DOI: doi:10.1038/nature18274 (cit. on p. 8).

[57] R. M. W. van Bijnen and T. Pohl. "Quantum Magnetism and Topological Ordering via Rydberg Dressing near Förster Resonances." In: *Phys. Rev. Lett.* 114 (24 June 2015), p. 243002. DOI: 10.1103/PhysRevLett.114.243002 (cit. on pp. 8, 67).

[58] B. Vermersch, A. W. Glaetzle, and P. Zoller. "Magic distances in the blockade mechanism of Rydberg p and d states." In: *Phys. Rev. A* 91 (2 Feb. 2015), p. 023411. DOI: 10.1103/PhysRevA.91.023411 (cit. on p. 8).

[59] R. H. Dicke. "Coherence in Spontaneous Radiation Processes." In: *Phys. Rev.* 93 (1 Jan. 1954), pp. 99–110. DOI: 10.1103/PhysRev.93.99 (cit. on pp. 8, 85).

[60] S. Weber et al. "Tutorial: Calculation of Rydberg interaction potentials." In: *arXiv:1612.08053* (2016) (cit. on p. 13).

[61] M. J. Seaton. "Quantum defect theory." In: *Reports on Progress in Physics* 46.2 (1983), p. 167 (cit. on pp. 14, 110).

[62] X. Zhang, F. B. Dunning, S. Yoshida, and J. Burgdörfer. "Rydberg blockade effects at $n \sim 300$ in strontium." In: *Phys. Rev. A* 92 (5 Nov. 2015), p. 051402. DOI: 10.1103/PhysRevA.92.051402 (cit. on p. 14).

[63] A. Osterwalder and F. Merkt. "Using High Rydberg States as Electric Field Sensors." In: *Phys. Rev. Lett.* 82 (9 Mar. 1999), pp. 1831–1834. DOI: 10.1103/PhysRevLett.82.1831 (cit. on p. 14).

[64] Robert Löw et al. "An experimental and theoretical guide to strongly interacting Rydberg gases." In: *Journal of Physics B: Atomic, Molecular and Optical Physics* 45.11 (2012), p. 113001 (cit. on pp. 14, 41, 59).

[65] Max Born and Robert Oppenheimer. "Zur Quantentheorie der Molekeln." In: *Annalen der Physik* 389.20 (1927), pp. 457–484 (cit. on p. 15).

[66] M. R. Flannery, D. Vrinceanu, and V. N. Ostrovsky. "Long-range interaction between polar Rydberg atoms." In: *J. Phys. B: At. Mol. Opt. Phys.* 38 (2005), S279–S293. DOI: doi:10.1088/0953-4075/38/2/020 (cit. on p. 15).

[67] K. R. Overstreet, A. Schwettmann, J. Tallant, D. Booth, and J. P. Shaffer. "Observation of electric-field-induced Cs Rydberg atom macrodimers." In: *Nature Physics* 5 (2009), pp. 581–585. DOI: doi:10.1038/nphys1307 (cit. on pp. 15, 23).

[68] Johannes Deiglmayr. "Long-range interactions between Rydberg atoms." In: *Physica Scripta* 91.10 (2016), p. 104007. DOI: http://dx.doi.org/10.1088/0031-8949/91/10/104007 (cit. on pp. 15, 21, 23, 24).

[69] H. Saßmannshausen, F. Merkt, and J. Deiglmayr. "High-resolution spectroscopy of Rydberg states in an ultracold cesium gas." In: *Phys. Rev. A* 87 (3 Mar. 2013), p. 032519. DOI: 10.1103/PhysRevA.87.032519 (cit. on p. 15).

[70] Wenhui Li, I. Mourachko, M. W. Noel, and T. F. Gallagher. "Millimeter-wave spectroscopy of cold Rb Rydberg atoms in a magneto-optical trap: Quantum defects of the ns , np , and nd series." In: *Phys. Rev. A* 67 (5 May 2003), p. 052502. DOI: 10.1103/PhysRevA.67.052502 (cit. on p. 15).

[71] Atreju Tauschinsky, Richard Newell, H. B. van Linden van den Heuvell, and R. J. C. Spreeuw. "Measurement of ^{87}Rb Rydberg-state hyperfine splitting in a room-temperature vapor cell." In: *Phys. Rev. A* 87 (4 Apr. 2013), p. 042522. DOI: 10.1103/PhysRevA.87.042522 (cit. on p. 15).

[72] "Long-Range Potential Coefficients From RKR Turning Points: C_6 and C_8 for $B(3\Pi_{Ou^+})$-State Cl_2, Br_2, and I_2." In: *Canadian Journal of Physics* 52.3 (1974), pp. 246–259. DOI: 10.1139/p74-035 (cit. on p. 15).

[73] John David Jackson. *Classical electrodynamics*. 3rd ed. New York, NY: Wiley, 1999. ISBN: 9780471309321 (cit. on pp. 16, 32).

[74] M. E. Rose. "The Electrostatic Interaction of Two Arbitrary Charge Distributions." In: *Journal of Mathematics and Physics* 37.1-4 (1958), pp. 215–222. ISSN: 1467-9590. DOI: 10.1002/sapm1958371215 (cit. on p. 16).

[75] Peter R. Fontana. "Theory of Long-Range Interatomic Forces. I. Dispersion Energies between Unexcited Atoms." In: *Phys. Rev.* 123 (5 Sept. 1961), pp. 1865–1870. DOI: 10.1103/PhysRev.123.1865 (cit. on p. 16).

[76] A. Dalgarno and W. D. Davidson. "The Calculation of Van Der Waals Interactions." In: *Advances in Atomic and Molecular Physics* 2 (1966), pp. 1–32. DOI: doi:10.1016/S0065-2199(08)60216-X (cit. on p. 16).

[77] L.C. Biedenharn, J.D. Louck, and P.A. Carruthers. *Angular Momentum in Quantum Physics: Theory and Application*. Encyclopedia of Mathematics and its Applications. Cambridge University Press, 2009. ISBN: 9780521102445 (cit. on pp. 17, 110).

[78] A. Reinhard, T. Cubel Liebisch, B. Knuffman, and G. Raithel. "Level shifts of rubidium Rydberg states due to binary interactions." In: *Phys. Rev. A* 75.3 (Mar. 2007), p. 032712. DOI: 10.1103/PhysRevA.75.032712 (cit. on p. 17).

[79] Franz Schwabl. *Quantenmechanik (QM I)*. Springer Berlin Heidelberg, 2007. DOI: 10.1007/978-3-540-73675-2 (cit. on p. 17).

[80] T. G. Walker and M. Saffman. "Consequences of Zeeman degeneracy for the van der Waals blockade between Rydberg atoms." In: *Phys. Rev. A* 77 (2008), p. 032723. DOI: 10.1103/PhysRevA.77.032723 (cit. on pp. 17, 22, 73, 75).

[81] Eugene Paul Wigner. *Group theory and its application to the quantum mechanics of atomic spectra*. New York: Academic Press, 1959 (cit. on pp. 22, 113).

[82] Arne Schwettmann, Jeff Crawford, K. Richard Overstreet, and James P. Shaffer. "Cold Cs Rydberg-gas interactions." In: *Phys. Rev. A* 74 (2 Aug. 2006), p. 020701. DOI: 10.1103/PhysRevA.74.020701 (cit. on p. 23).

[83] Johannes Deiglmayr, Heiner Saßmannshausen, Pierre Pillet, and Frédéric Merkt. "Observation of Dipole-Quadrupole Interaction in an Ultracold Gas of Rydberg Atoms." In: *Phys. Rev. Lett.* 113 (19 Nov. 2014), p. 193001. DOI: 10.1103/PhysRevLett.113.193001 (cit. on p. 23).

[84] A. Urvoy et al. "Strongly Correlated Growth of Rydberg Aggregates in a Vapor Cell." In: *Phys. Rev. Lett.* 114 (20 May 2015), p. 203002. DOI: 10.1103/PhysRevLett.114.203002 (cit. on pp. 23, 24).

[85] S. M. Farooqi et al. "Long-Range Molecular Resonances in a Cold Rydberg Gas." In: *Phys. Rev. Lett.* 91 (18 Oct. 2003), p. 183002. DOI: 10.1103/PhysRevLett.91.183002 (cit. on p. 23).

[86] J. Stanojevic, R. Côté, D. Tong, E. E. Eyler, and P. L. Gould. "Long-range potentials and $(n-1)d+ns$ molecular resonances in an ultracold Rydberg gas." In: *Phys. Rev. A* 78 (5 Nov. 2008), p. 052709. DOI: 10.1103/PhysRevA.78.052709 (cit. on p. 23).

[87] Heiner Saßmannshausen and Johannes Deiglmayr. "Observation of Rydberg-Atom Macrodimers: Micrometer-Sized Diatomic Molecules." In: *Phys. Rev. Lett.* 117 (8 Aug. 2016), p. 083401. DOI: 10.1103/PhysRevLett.117.083401 (cit. on pp. 23, 24).

[88] Sylvain Ravets, Henning Labuhn, Daniel Barredo, Thierry Lahaye, and Antoine Browaeys. "Measurement of the angular dependence of the dipole-dipole interaction between two individual Rydberg atoms at a Förster resonance." In: *Phys. Rev. A* 92 (2 Aug. 2015), p. 020701. DOI: 10.1103/PhysRevA.92.020701 (cit. on pp. 25, 67).

[89] C. Cohen-Tannoudji, J. Dupont-Roc, and G. Grynberg. *Atom-Photon Interactions: Basic Process and Applications*. Wiley Inc., 2008. ISBN: 9780471293361. DOI: 10.1002/9783527617197 (cit. on p. 31).

[90] Paul Siddons. "Light propagation through atomic vapours." In: *Journal of Physics B: Atomic, Molecular and Optical Physics* 47.9 (2014), p. 093001 (cit. on p. 32).

[91] R. Meppelink, R. A. Rozendaal, S. B. Koller, J. M. Vogels, and P. van der Straten. "Thermodynamics of Bose-Einstein-condensed clouds using phase-contrast imaging." In: *Phys. Rev. A* 81 (5 May 2010), p. 053632. DOI: 10.1103/PhysRevA.81.053632 (cit. on p. 33).

[92] F. T. Arecchi and Bonifacio R. "Theory of Optical Maser Amplifiers." In: *IEEE Jornal of Quamtum Electronics* QE-1.4 (1965), pp. 179–178 (cit. on p. 33).

[93] D. A. Steck. "Rubidium 87 D Line Data." In: *online available* (2015) (cit. on p. 35).

[94] Michael Fleischhauer, Atac Imamoglu, and Jonathan P. Marangos. "Electromagnetically induced transparency: Optics in coherent media." In: *Rev. Mod. Phys.* 77 (2 July 2005), pp. 633–673. DOI: 10.1103/RevModPhys.77.633 (cit. on pp. 37, 39).

[95] S. E. Harris. "Lasers without inversion: Interference of lifetime-broadened resonances." In: *Phys. Rev. Lett.* 62 (9 Feb. 1989), pp. 1033–1036. DOI: 10.1103/PhysRevLett.62.1033 (cit. on p. 38).

[96] P. Bienias et al. "Scattering resonances and bound states for strongly interacting Rydberg polaritons." In: *Phys. Rev. A* 90 (5 Nov. 2014), p. 053804. DOI: 10.1103/PhysRevA.90.053804 (cit. on pp. 44, 81).

[97] Hannes Gorniaczyk. "Single Photon Transistor mediated by electrically tunable Rydberg-Rydberg interactions." Ph.D. Thesis. Universität Stuttgart, 2016 (cit. on pp. 49, 50, 64).

[98] T. Baluktsian, B. Huber, R. Löw, and T. Pfau. "Evidence for Strong van der Waals Type Rydberg-Rydberg Interaction in a Thermal Vapor." In: *Phys. Rev. Lett.* 110 (12 Mar. 2013), p. 123001. DOI: 10.1103/PhysRevLett.110.123001 (cit. on p. 49).

[99] M. M. Müller et al. "Room-temperature Rydberg single-photon source." In: *Phys. Rev. A* 87 (5 May 2013), p. 053412. DOI: 10.1103/PhysRevA.87.053412 (cit. on p. 49).

[100] E. Amaldi and E. Segré. "Effect of Pressure on High Terms of Alkaline Spectra." In: *Nature* (1934), p. 141. DOI: doi:10.1038/133141a0 (cit. on p. 49).

[101] Michael Schlagmueller. "A single Rydberg Atom interacting with a Dense and Ultracold Gas." Ph.D. Thesis. Universität Stuttgart, 2016 (cit. on pp. 51, 53).

[102] Christoph Tresp. "A setup for higly precise excitation and detection of Rydberg atoms." Master Thesis. Universität Stuttgart, 2012 (cit. on p. 53).

[103] Stephan Jennewein. "Building an Apparatus for Cold Rubidium Rydberg Atoms." Diploma Thesis. Universität Stuttgart, 2012 (cit. on p. 53).

[104] J. Appel, A. MacRae, and A. I. Lvovsky. "A versatile digital GHz phase lock for external cavity diode lasers." In: *Measurement Science and Technology* 20.5 (2009), p. 055302 (cit. on p. 54).

[105] Johannes Schmidt. "Generation of non-classical light using ultra-cold Rydberg ensembles." Master Thesis. Universität Stuttgart, 2014 (cit. on p. 54).

[106] T. F. Gallagher. *Rydberg Atoms*. Cambridge U, 1994 (cit. on pp. 55, 110).

[107] David E. Pritchard. "Cooling Neutral Atoms in a Magnetic Trap for Precision Spectroscopy." In: *Phys. Rev. Lett.* 51 (15 Oct. 1983), pp. 1336–1339. DOI: 10.1103/PhysRevLett.51.1336 (cit. on p. 55).

[108] Steven Chu, J. E. Bjorkholm, A. Ashkin, and A. Cable. "Experimental Observation of Optically Trapped Atoms." In: *Phys. Rev. Lett.* 57 (3 July 1986), pp. 314–317. DOI: 10.1103/PhysRevLett.57.314 (cit. on p. 55).

[109] J. D. Miller, R. A. Cline, and D. J. Heinzen. "Far-off-resonance optical trapping of atoms." In: *Phys. Rev. A* 47 (6 June 1993), R4567–R4570. DOI: 10.1103/PhysRevA.47.R4567 (cit. on p. 55).

[110] S. J. M. Kuppens, K. L. Corwin, K. W. Miller, T. E. Chupp, and C. E. Wieman. "Loading an optical dipole trap." In: *Phys. Rev. A* 62 (1 June 2000), p. 013406. DOI: 10.1103/PhysRevA.62.013406 (cit. on p. 55).

[111] S. Zhang, F. Robicheaux, and M. Saffman. "Magic-wavelength optical traps for Rydberg atoms." In: *Phys. Rev. A* 84 (4 Oct. 2011), p. 043408. DOI: 10.1103/PhysRevA.84.043408 (cit. on p. 55).

[112] L. Li, Y. O. Dudin, and A. Kuzmich. "Entanglement between light and an optical atomic excitation." In: *Nature* 498 (2013), pp. 466–469. DOI: 10.1038/nature12227 (cit. on p. 55).

[113] Rudolf Grimm, Matthias Weidemüller, and Yurii B. Ovchinnikov. "Optical Dipole Traps for Neutral Atoms." In: ed. by Benjamin Bederson and Herbert Walther. Vol. 42. Advances In Atomic, Molecular, and Optical Physics. Academic Press, 2000, pp. 95–170. DOI: http://dx.doi.org/10.1016/S1049-250X(08)60186-X (cit. on pp. 56, 57).

[114] M. D. Barrett, J. A. Sauer, and M. S. Chapman. "All-Optical Formation of an Atomic Bose-Einstein Condensate." In: *Phys. Rev. Lett.* 87 (1 June 2001), p. 010404. DOI: 10.1103/PhysRevLett.87.010404 (cit. on p. 60).

[115] S. R. Granade, M. E. Gehm, K. M. O'Hara, and J. E. Thomas. "All-Optical Production of a Degenerate Fermi Gas." In: *Phys. Rev. Lett.* 88 (12 Mar. 2002), p. 120405. DOI: 10.1103/PhysRevLett.88.120405 (cit. on p. 60).

[116] Christoph Braun. "Implementation of Raman Sideband Cooling for ^{87}Rb." Bachelor Thesis. Universität Stuttgart, 2015 (cit. on pp. 60, 61).

[117] Jürgen Eschner, Giovanna Morigi, Ferdinand Schmidt-Kaler, and Rainer Blatt. "Laser cooling of trapped ions." In: *J. Opt. Soc. Am. B* 20.5 (May 2003), pp. 1003–1015. DOI: 10.1364/JOSAB.20.001003 (cit. on p. 60).

[118] Vladan Vuleti ć, Cheng Chin, Andrew J. Kerman, and Steven Chu. "Degenerate Raman Sideband Cooling of Trapped Cesium Atoms at Very High Atomic Densities." In: *Phys. Rev. Lett.* 81 (26 Dec. 1998), pp. 5768–5771. DOI: 10.1103/PhysRevLett.81.5768 (cit. on p. 60).

[119] D. J. Wineland et al. "Experimental Issues in Coherent Quantum-State Manipulation of Trapped Atomic Ions." In: *J. of Research of NIST* 103.3 (1998), p. 259. DOI: 10.6028/jres.103.019 (cit. on p. 61).

[120] Simon Baur, Daniel Tiarks, Gerhard Rempe, and Stephan Dürr. "Single-Photon Switch Based on Rydberg Blockade." In: *Phys. Rev. Lett.* 112 (7 Feb. 2014), p. 073901. DOI: 10.1103/PhysRevLett.112.073901 (cit. on pp. 63, 65, 71, 83, 95, 102).

[121] C. Liu, Z. Dutton, C. H. Behroozi, and L. V. Hau. "Observation of coherent optical information storage in an atomic medium using halted light pulses." In: *Nature* 409 (6819 2001), pp. 490–493. DOI: 10.1038/35054017 (cit. on p. 64).

[122] Bo Zhao et al. "A millisecond quantum memory for scalable quantum networks." In: *Nature Physics* 5 (2009), pp. 95–99. DOI: doi:10.1038/nphys1153 (cit. on pp. 66, 94).

[123] Weibin Li and Igor Lesanovsky. "Coherence in a cold-atom photon switch." In: *Phys. Rev. A* 92 (4 Oct. 2015), p. 043828. DOI: 10.1103/PhysRevA.92.043828 (cit. on p. 66).

[124] C R Murray, A V Gorshkov, and T Pohl. "Many-body decoherence dynamics and optimized operation of a single-photon switch." In: *New Journal of Physics* 18.9 (2016), p. 092001 (cit. on p. 66).

[125] J. Nipper et al. "Atomic Pair-State Interferometer: Controlling and Measuring an Interaction-Induced Phase Shift in Rydberg-Atom Pairs." In: *Phys. Rev. X* 2 (3 Aug. 2012), p. 031011. DOI: 10.1103/PhysRevX.2.031011 (cit. on p. 67).

[126] T Lahaye, C Menotti, L Santos, M Lewenstein, and T Pfau. "The physics of dipolar bosonic quantum gases." In: *Reports on Progress in Physics* 72.12 (2009), p. 126401 (cit. on p. 67).

[127] M. V. Gurudev Dutt et al. "Quantum Register Based on Individual Electronic and Nuclear Spin Qubits in Diamond." In: *Science* 316 (2007), p. 1312. DOI: 10.1126/science.1139831 (cit. on p. 67).

[128] P. Neumann et al. "Multipartite Entanglement Among Single Spins in Diamond." In: *Science* 320 (2008), pp. 1326–1329. DOI: 10.1126/science.1157233 (cit. on p. 67).

[129] Thierry Lahaye et al. "Strong dipolar effects in a quantum ferrofluid." In: *Nature* 448 (2007), pp. 672–675. DOI: doi:10.1038/nature06036 (cit. on p. 67).

[130] K. Aikawa et al. "Observation of Fermi surface deformation in a dipolar quantum gas." In: *Science* 345 (2014), pp. 1484–1487. DOI: 10.1126/science.1255259 (cit. on p. 67).

[131] Holger Kadau et al. "Observing the Rosensweig instability of a quantum ferrofluid." In: *Nature* 530 (2016), p. 194. DOI: 10.1038/nature16485 (cit. on p. 67).

[132] Matthias Schmitt, Matthias Wenzel, Fabian Böttcher, Igor Ferrier-Barbut, and Tilman Pfau. "Self-bound droplets of a dilute magnetic quantum liquid." In: *Nature* 539 (2016), p. 259. DOI: 10.1038/nature20126 (cit. on p. 67).

[133] Bo Yan et al. "Observation of dipolar spin-exchange interactions with lattice-confined polar molecules." In: *Nature* 501 (2013), pp. 521–525. DOI: doi:10.1038/nature12483 (cit. on p. 67).

[134] D. Comparat and P. Pillet. "Dipole blockade in a cold Rydberg atomic sample." In: *J. Opt. Soc. Am. B* 27 (2010), A208–A232. DOI: 10.1364/JOSAB.27.00A208 (cit. on p. 67).

[135] M. Saffman, T. G. Walker, and K. Mølmer. "Quantum information with Rydberg atoms." In: *Rev. Mod. Phys.* 82 (2010), p. 2313. DOI: 10.1103/RevModPhys.82.2313 (cit. on p. 67).

[136] Alexey V. Gorshkov et al. "Tunable Superfluidity and Quantum Magnetism with Ultracold Polar Molecules." In: *Phys. Rev. Lett.* 107 (11 Sept. 2011), p. 115301. DOI: 10.1103/PhysRevLett.107.115301 (cit. on p. 67).

[137] Alexander W. Glaetzle et al. "Designing Frustrated Quantum Magnets with Laser-Dressed Rydberg Atoms." In: *Phys. Rev. Lett.* 114 (17 Apr. 2015), p. 173002. DOI: 10.1103/PhysRevLett.114.173002 (cit. on p. 67).

[138] N. Y. Yao et al. "Topological Flat Bands from Dipolar Spin Systems." In: *Phys. Rev. Lett.* 109 (26 Dec. 2012), p. 266804. DOI: 10.1103/PhysRevLett.109.266804 (cit. on p. 67).

[139] Andrei Derevianko, Péter Kómár, Turker Topcu, Ronen M. Kroeze, and Mikhail D. Lukin. "Effects of molecular resonances on Rydberg blockade." In: *Phys. Rev. A* 92 (6 Dec. 2015), p. 063419. DOI: 10.1103/PhysRevA.92.063419 (cit. on p. 75).

[140] Weibin Li, Daniel Viscor, Sebastian Hofferberth, and Igor Lesanovsky. "Electromagnetically Induced Transparency in an Entangled Medium." In: *Phys. Rev. Lett.* 112 (24 June 2014), p. 243601. DOI: 10.1103/PhysRevLett.112.243601 (cit. on p. 79).

[141] Przemyslaw Bienias. "Few-body quantum physics with strongly interacting Rydberg polaritons." Ph.D. Thesis. Universität Stuttgart, 2016 (cit. on p. 81).

[142] Valentina Parigi, Alessandro Zavatta, Myungshik Kim, and Marco Bellini. "Probing Quantum Commutation Rules by Addition and Subtraction of Single Photons to/from a Light Field." In: *Science* 317.5846 (2007), pp. 1890–1893. ISSN: 0036-8075. DOI: 10.1126/science.1146204 (cit. on pp. 83, 103).

[143] R. Kumar, E. Barrios, C. Kupchak, and A. I. Lvovsky. "Experimental Characterization of Bosonic Creation and Annihilation Operators." In: *Phys. Rev. Lett.* 110 (13 Mar. 2013), p. 130403. DOI: 10.1103/PhysRevLett.110.130403 (cit. on pp. 83, 103).

[144] G. J. Milburn. "Quantum optical Fredkin gate." In: *Phys. Rev. Lett.* 62 (18 May 1989), pp. 2124–2127. DOI: 10.1103/PhysRevLett.62.2124 (cit. on p. 83).

[145] Jaromír Fiurásek, Raúl Garía-Patión, and Nicolas J. Cerf. "Conditional generation of arbitrary single-mode quantum states of light by repeated photon subtractions." In: *Phys. Rev. A* 72 (3 Sept. 2005), p. 033822. DOI: 10.1103/PhysRevA.72.033822 (cit. on p. 83).

[146] J. S. Neergaard-Nielsen, B. Melholt Nielsen, C. Hettich, K. Mølmer, and E. S. Polzik. "Generation of a Superposition of Odd Photon Number States for Quantum Information Networks." In: *Phys. Rev. Lett.* 97 (8 Aug. 2006), p. 083604. DOI: 10.1103/PhysRevLett.97.083604 (cit. on pp. 83, 98, 103).

[147] Hiroki Takahashi et al. "Entanglement distillation from Gaussian input states." In: *Nature Photonics* 4 (2010), pp. 178–181. DOI: doi:10.1038/nphoton.2010.1 (cit. on pp. 83, 103).

[148] D.E. Chang et al. "Crystallization of strongly interacting photons in a nonlinear optical fiber." In: *Nature Physics* 4 (2008), pp. 884–889. DOI: doi:10.1038/nphys1074 (cit. on p. 83).

[149] Iacopo Carusotto and Cristiano Ciuti. "Quantum fluids of light." In: *Rev. Mod. Phys.* 85 (1 Feb. 2013), pp. 299–366. DOI: 10.1103/RevModPhys.85.299 (cit. on p. 83).

[150] Darrick E. Chang, Vladan Vuleti ć, and Mikhail D. Lukin. "Quantum nonlinear optics: photon by photon." In: *Nature Photonics* 8 (2014), pp. 685–694. DOI: doi:10.1038/nphoton.2014.192 (cit. on p. 83).

[151] Daniel Braun, Pu Jian, Olivier Pinel, and Nicolas Treps. "Precision measurements with photon-subtracted or photon-added Gaussian states." In: *Phys. Rev. A* 90 (1 July 2014), p. 013821. DOI: 10.1103/PhysRevA.90.013821 (cit. on pp. 83, 103).

[152] Alexei Ourjoumtsev, Rosa Tualle-Brouri, Julien Laurat, and Philippe Grangier. "Generating Optical Schrödinger Kittens for Quantum Information Processing." In: *Science* 312 (2006), pp. 83–86 (cit. on pp. 83, 98, 103).

[153] D. Pinotsi and A. Imamoglu. "Single Photon Absorption by a Single Quantum Emitter." In: *Phys. Rev. Lett.* 100 (9 Mar. 2008), p. 093603. DOI: 10.1103/PhysRevLett.100.093603 (cit. on p. 83).

[154] Io-Chun Hoi et al. "Giant Cross-Kerr Effect for Propagating Microwaves Induced by an Artificial Atom." In: *Phys. Rev. Lett.* 111 (5 Aug. 2013), p. 053601. DOI: 10.1103/PhysRevLett.111.053601 (cit. on p. 83).

[155] Serge Rosenblum et al. "Extraction of a single photon from an optical pulse." In: *Nature Photonics* 10 (Jan. 2016), pp. 19–22. DOI: 10.1038/nphoton.2015.227 (cit. on p. 83).

[156] A Zavatta, V Parigi, M S Kim, and M Bellini. "Subtracting photons from arbitrary light fields: experimental test of coherent state invariance by single-photon annihilation." In: *New Journal of Physics* 10.12 (2008), p. 123006. DOI: http://dx.doi.org/10.1088/1367-2630/10/12/123006 (cit. on pp. 83, 98, 103).

[157] G. Günter et al. "Interaction Enhanced Imaging of Individual Rydberg Atoms in Dense Gases." In: *Phys. Rev. Lett.* 108 (1 Jan. 2012), p. 013002. DOI: 10.1103/PhysRevLett.108.013002 (cit. on p. 83).

[158] B. Olmos, W. Li, S. Hofferberth, and I. Lesanovsky. "Amplifying single impurities immersed in a gas of ultracold atoms." In: *Phys. Rev. A* 84 (4 Oct. 2011), p. 041607. DOI: 10.1103/PhysRevA.84.041607 (cit. on p. 83).

[159] S Quabis, R Dorn, M Eberler, O Glöckl, and G Leuchs. "Focusing light to a tighter spot1." In: *Optics Communications* 179.1–6 (2000), pp. 1–7. ISSN: 0030-4018. DOI: http://dx.doi.org/10.1016/S0030-4018(99)00729-4 (cit. on p. 84).

[160] Y. O. Dudin, L. Li, F. Bariani, and A. Kuzmich. "Observation of coherent many-body Rabi oscillations." In: *Nature Phys.* 8 (2012), p. 790. DOI: doi:10.1038/nphys2413 (cit. on pp. 86, 102).

[161] R. Heidemann et al. "Rydberg Excitation of Bose-Einstein Condensates." In: *Phys. Rev. Lett.* 100 (2008), p. 033601. DOI: 10.1103/PhysRevLett.100.033601 (cit. on p. 86).

[162] Jens Honer. "Strongly Interacting Many-Body Systems in Cold Atomic Gases." Ph.D. Thesis. Universität Stuttgart, 2013 (cit. on p. 87).

[163] Leonard Mandel and Emil Wolf. *Optical Coherence and Quantum Optics:* Cambridge: Cambridge University Press, Sept. 1995. ISBN: 9781139644105. DOI: 10.1017/CBO9781139644105 (cit. on p. 89).

[164] Y. O. Dudin, L. Li, and A. Kuzmich. "Light storage on the time scale of a minute." In: *Phys. Rev. A* 87 (3 Mar. 2013), p. 031801. DOI: 10.1103/PhysRevA.87.031801 (cit. on p. 94).

[165] V. Bendkowsky et al. "Observation of ultralong-range Rydberg molecules." In: *Nature* 458 (2009), pp. 1005–1008. DOI: 10.1038/nature07945 (cit. on p. 95).

[166] A. Gaj et al. "From molecular spectra to a density shift in dense Rydberg gases." In: *Nature Comm.* 5 (2014), p. 4546. DOI: doi:10.1038/ncomms5546 (cit. on p. 95).

[167] Thomas Niederprüm, Oliver Thomas, Torsten Manthey, Tobias M. Weber, and Herwig Ott. "Giant Cross Section for Molecular Ion Formation in Ultracold Rydberg Gases." In: *Phys. Rev. Lett.* 115 (1 July 2015), p. 013003. DOI: 10.1103/PhysRevLett.115.013003 (cit. on p. 95).

[168] Michael Schlagmüller et al. "Probing an Electron Scattering Resonance using Rydberg Molecules within a Dense and Ultracold Gas." In: *Phys. Rev. Lett.* 116 (5 Feb. 2016), p. 053001. DOI: 10.1103/PhysRevLett.116.053001 (cit. on p. 95).

[169] C. Ates, T. Pohl, T. Pattard, and J. M. Rost. "Antiblockade in Rydberg Excitation of an Ultracold Lattice Gas." In: *Phys. Rev. Lett.* 98 (2 Jan. 2007), p. 023002. DOI: 10.1103/PhysRevLett.98.023002 (cit. on p. 97).

[170] Thomas Amthor, Christian Giese, Christoph S. Hofmann, and Matthias Weidemüller. "Evidence of Antiblockade in an Ultracold Rydberg Gas." In: *Phys. Rev. Lett.* 104 (1 Jan. 2010), p. 013001. DOI: 10.1103/PhysRevLett.104.013001 (cit. on p. 97).

[171] Alexey V. Gorshkov, Rejish Nath, and Thomas Pohl. "Dissipative Many-Body Quantum Optics in Rydberg Media." In: *Phys. Rev. Lett.* 110 (15 Apr. 2013), p. 153601. DOI: 10.1103/PhysRevLett.110.153601 (cit. on p. 97).

[172] Rainer Kimmich. *NMR Tomography, Diffusometry, Relaxometry.* Springer, 2001 (cit. on p. 102).

[173] S. Sevin çli, N. Henkel, C. Ates, and T. Pohl. "Nonlocal Nonlinear Optics in Cold Rydberg Gases." In: *Phys. Rev. Lett.* 107 (15 Oct. 2011), p. 153001. DOI: 10.1103/PhysRevLett.107.153001 (cit. on p. 104).

[174] G. W. F. Drake and R. A. Swainson. "Quantum defects and the $1/n$ dependence of Rydberg energies: Second-order polarization effects." In: *Phys. Rev. A* 44 (9 Nov. 1991), pp. 5448–5459. DOI: 10.1103/PhysRevA.44.5448 (cit. on p. 109).

[175] C L Vaillant, M P A Jones, and R M Potvliege. "Long-range Rydberg-Rydberg interactions in calcium, strontium and ytterbium." In: *Journal of Physics B: Atomic, Molecular and Optical Physics* 45.13 (2012), p. 135004 (cit. on p. 109).

[176] J. Hostetter, J. D. Pritchard, J. E. Lawler, and M. Saffman. "Measurement of holmium Rydberg series through magneto-optical trap depletion spectroscopy." In: *Phys. Rev. A* 91 (1 Jan. 2015), p. 012507. DOI: 10.1103/PhysRevA.91.012507 (cit. on p. 109).

[177] D. R. Bates and Agnete Damgaard. "The Calculation of the Absolute Strengths of Spectral Lines." In: *Philosophical Transactions of the Royal Society of London A: Mathematical, Physical and Engineering Sciences* 242.842 (1949), pp. 101–122. ISSN: 0080-4614. DOI: 10.1098/rsta.1949.0006. eprint: http://rsta.royalsocietypublishing.org/content/242/842/101.full.pdf (cit. on pp. 110, 113).

[178] W R Johnson and K T Cheng. "Quantum defects for highly stripped ions." In: *Journal of Physics B: Atomic and Molecular Physics* 12.6 (1979), p. 863. DOI: http://dx.doi.org/10.1088/0022-3700/12/6/006 (cit. on p. 111).

[179] Constantine E. Theodosiou. "Lifetimes of alkali-metal—atom Rydberg states." In: *Phys. Rev. A* 30 (6 Dec. 1984), pp. 2881–2909. DOI: 10.1103/PhysRevA.30.2881 (cit. on p. 111).

[180] M. Marinescu, H. R. Sadeghpour, and A. Dalgarno. "Dispersion coefficients for alkali-metal dimers." In: *Phys. Rev. A* 49 (2 Feb. 1994), pp. 982–988. DOI: 10.1103/PhysRevA.49.982 (cit. on pp. 111, 112).

[181] Chris H. Greene and Mireille Aymar. "Spin-orbit effects in the heavy alkaline-earth atoms." In: *Phys. Rev. A* 44 (3 Aug. 1991), pp. 1773–1790. DOI: 10.1103/PhysRevA.44.1773 (cit. on p. 111).

[182] Ali Sanayei et al. "Quasiclassical quantum defect theory and the spectrum of highly excited rubidium atoms." In: *Phys. Rev. A* 91 (3 Mar. 2015), p. 032509. DOI: 10.1103/PhysRevA.91.032509 (cit. on p. 112).

[183] Myron L. Zimmerman, Michael G. Littman, Michael M. Kash, and Daniel Kleppner. "Stark structure of the Rydberg states of alkali-metal atoms." In: *Phys. Rev. A* 20 (6 Dec. 1979), pp. 2251–2275. DOI: 10.1103/PhysRevA.20.2251 (cit. on p. 113).

[184] S. A. Bhatti, C. L. Cromer, and W. E. Cooke. "Analysis of the Rydberg character of the $5d7d\,^1D_2$ state of barium." In: *Phys. Rev. A* 24 (1 July 1981), pp. 161–165. DOI: 10.1103/PhysRevA.24.161 (cit. on p. 113).

[185] B Kaulakys. "Consistent analytical approach for the quasi-classical radial dipole matrix elements." In: *J. Phys. B: At. Mol. Opt. Phys.* 28 (1995), p. 4963. DOI: doi:10.1088/0953-4075/28/23/008 (cit. on p. 113).

[186] G Lagmago Kamta, S G Nana Engo, M G Kwato Njock, and B Oumarou. "Consistent description of Klein-Gordon dipole matrix elements." In: *Journal of Physics B: Atomic, Molecular and Optical Physics* 31.5 (1998), p. 963 (cit. on pp. 113, 114).

[187] M. S. Safronova and U. I. Safronova. "Critically evaluated theoretical energies, lifetimes, hyperfine constants, and multipole polarizabilities in ^{87}Rb." In: *Phys. Rev. A* 83 (5 May 2011), p. 052508. DOI: 10.1103/PhysRevA.83.052508 (cit. on p. 113).

[188] M. S. Safronova, U. I. Safronova, and Charles W. Clark. "Magic wavelengths, matrix elements, polarizabilities, and lifetimes of Cs." In: *Phys. Rev. A* 94 (1 July 2016), p. 012505. DOI: 10.1103/PhysRevA.94.012505 (cit. on p. 113).

[189] Igor I. Sobelman. *Atomic Spectra and Radiative Transitions*. Springer, 1992 (cit. on p. 113).

Danksagung

Nach insgesamt fast sieben Jahren am PI5, die mit einem Hiwi-Job während meines Studiums begonnen haben, möchte ich mich schließlich bei denjenigen bedanken die zum Gelingen dieser Arbeit beigetragen haben.

Besonders hervorheben möchte ich dabei meinen Betreuer Sebastian Hofferberth. Seit sich unsere Wege vor über fünf Jahren zum ersten Mal gekreuzt haben, konnte ich in einer Vielzahl von Diskussionen eine Menge von Dir lernen und meine Fähigkeiten in verschiedensten Bereichen verbessern. Ich wünsche Dir viel Erfolg beim Neuanfang als Professor in Dänemark und ein paar erfolgreiche Anträge um Deine Gruppe zu erweitern!

Die meiste Zeit am Experiment habe ich mit Hannes Gorniaczyk verbracht. Zusammen ist es uns gelungen auf den ehemals leeren Labortischen ein tolles Experiment aufzubauen, welches einige hervorragende Ergebnisse abgeliefert hat. Vielen Dank für deinen unermüdlichen Arbeitseinsatz und die fantastische Software zum Aufzeichnen und Speichern der Daten.

Später hinzugestoßen sind Ivan Mirgorodskiy und Asaf Paris-Mandoki. Euer internationaler Einfluss hat geholfen dieses "schwäbisch-norddeutsche" Experiment nochmals auf eine neue Stufe zu heben und auch nach der Zeit von Hannes und mir ein paar schöne Ergebnisse mit der Apparatur zu erzielen.

Für die Unterstützung in einer Vielzahl von kleineren und größeren Projekten gebührt mein Dank den zahlreichen Hiwis, Bachelor- und Masterstudenten die zeitweise am Experiment beteiligt waren. Explizit genannt seien hier Fabian Böttcher, Johannes Schmidt, Thomas Dieterle, Christoph Braun, Christian Zimmer und Florian Christaller.

Vielen Dank auch an die Kollegen des "Superatoms"-Experiments, mit denen wir nicht nur das Labor sondern auch einige technische Entwicklungen geteilt haben. Besonders die von Michael Schlagmüller entwickelte Elektronik und Computersteuerung waren eine extreme Hilfe.

Die unmittelbare räumliche und thematische Nähe zur Gruppe von Prof. Hans Peter Büchler am ITP3 ermöglichte einige fruchtbare Kollaborationen. Hierbei möchte ich mich besonders bei Przemyslaw Bienias und Sebastian Weber für eine Vielzahl von hilfreichen Diskussionen im Rahmen unserer gemeinsamen Projekte bedanken.

Tilman Pfau und Robert Löw haben mich während meines Bachelorstudiums in ihren Vorlesungen für die Forschung am PI5 begeistert und mir dadurch ermöglicht den Fuß in die Tür dieses faszinierenden Teilgebiets der Physik zu setzen. Dafür möchte ich mich bei Euch beiden bedanken. Außerdem seid Ihr die Hauptverantwortlichen für den guten Austausch zwischen den einzelnen Experimenten und die tolle Atmosphäre am Institut.

Dafür verantwortlich sind natürlich auch alle anderen Mitglieder des Instituts die ihre Zeit mir geteilt haben. Es war mir immer eine Freude Kaffeepausen oder Aktivitäten außerhalb der Universität wie Wanderungen, Kanufahrten oder Volleyballturniere mit euch zu verbringen.

Vielen Dank an die Mitarbeiter in der Administration des Instituts, Astrid Buck, Anne-Katrin Kriesch, Britta Lenz und Karin Otter, für die Unterstützung beim Schreiben von Begründungen zu Vertragsverlängerungen, Bezahlen von Rechnungen und Hilfe bei der Kommunikation mit der Hochschulverwaltung. Nicht zu vernachlässigen ist der unermüdliche Einsatz von Harald Kübler was die Computerinfrastruktur des Instituts betrifft.

Für die schnelle und unkomplizierte Übernahme des Mitberichts dieser Arbeit in einem eng gestrickten zeitlichen Rahmen möchte ich mich bei Prof. Martin Dressel und Dr. Thomas Pohl bedanken, sowie bei Prof. Hans Peter Büchler für den Vorsitz und die freundliche Atmosphäre in meiner mündlichen Prüfung.

Nicht vergessen möchte ich meine Freunde innerhalb und außerhalb der Universität. Gemeinsame Unternehmungen haben stets geholfen den hin und wieder rauchenden Kopf frei zu bekommen um wieder neue Motivation schöpfen zu können.

Nicht zuletzt geht ein großes Dankeschön an meine Familie. Ohne ihre Unterstützung über all die Jahre wäre es mir niemals möglich gewesen diese Arbeit anzufertigen.

Danke!